Temperature Field Measurements with High Spatial and Temporal Resolution Using Liquid Crystal Thermography and Laser Induced Fluorescence

Vom Fachbereich Maschinenbau
an der Technischen Universität Darmstadt
zur
Erlangung des Grades eines Doktor-Ingenieurs (Dr.-Ing.)
genehmigte

Dissertation

vorgelegt von

Dipl.-Ing. Ralph Nasarek

aus Laudenbach

Berichterstatter:	Prof. Dr.-Ing. P. Stephan
Mitberichterstatter:	Prof. Steve Wereley
Tag der Einreichung:	04.05.2009
Tag der mündlichen Prüfung:	06.07.2009

Darmstadt 2010

D17

Acknowledgments

The present work was created during my stay at the Fachgebiet Technische Thermodynamik (TTD) at Technische Universität Darmstadt. Foremost, I would like to thank the leader of the TTD group and my advisor, Prof. Dr.-Ing. P. Stephan, who gave me the opportunity, support and freedom I needed for the realization of this work. I would also like to thank Prof. Dr. Dr. habil. C. Tropea, the leader of the Graduiertenkolleg 1114 (Optische Messtechniken für die Charakterisierung von Transportprozessen an Grenzflächen), of which I was member, and the Deutsche Forschungsgemeinschaft, who financed my work. Further, I would like to thank Prof. S. Wereley for accepting the task of co-examiner, for facilitating my stay in the U.S. and for fruitful discussions concerning flow dynamics, high resolution measurement techniques and other important things in life.

I want to express my thanks to all my former colleagues of TTD. With discussions, support and meetings in the seminar room after work you made the daily work at TTD very pleasant. In particular, I would like to thank Jan Vogt as my diploma student, co-worker and now follower of my project. He took part in designing and conducting experiments, providing fresh ideas and in inciting important discussions. I thank Dr.-Ing. Frank Dammel for performing the numerical calculations of the thermal induced free convection in the cubic facility and for many helpful discussions; Prof. Dr. rer. nat. habil. Andreas Dreizler and Dr.-Ing. Jan Brübach for their support and knowledge transfer regarding spectroscopic measurements; Boris Schilder and Dr.-Ing. Enno Wagner with whom I had the pleasure to work in several side projects; Benjamin Fröhlich from the institute of Produktionstechnik with whom I had exciting discussions not only during lunch time; my colleagues and their advisors in the Graduierten Kolleg 1114 for seminar days, summer schools, and Alpentouren; Jan Vogt, Christian Kunkelmann and Elyssa Tardif for proofreading the thesis and Felix Brinckmann for general sup-

port even on weekends. Additionally, I would like to thank all the students who helped me in the form of student projects or student jobs. In particular, Thomas Schaaf, Philipp Trunk, Benjamin Meyer, and Harald Glawe demonstrated excellent motivation in fulfilling their studies and jobs.

Sincere thanks are dedicated to the staff of TTD without whom the realization of the work would not have been possible. In particular, I thank Gabi Gunkel and Ingrid Benz for support in every situation, Roland Berntheisel and the whole workshop crew who did a very good job fabricating experimental setups and helping to design the experiments, Robert Schrod (Thanks again for changing so many transistors) and Moritz Mattern for all the computer and network stuff.

Last but not least, I want to thank those who supported me in many difficult situations, in particular my girlfriend Moa-Li Gourmelon for all the support (especially in the final days), and my parents.

Hiermit versichere ich, die vorliegende Doktorarbeit unter der Betreuung von Prof. Dr.-Ing. Peter Stephan nur mit den angegebenen Hilfsmitteln selbständig angefertigt zu haben.

Ralph Nasarek

Darmstadt, den 02.05.2009

Zusammenfassung

Räumlich hochauflösende Temperaturfeldmessungen sind wichtig, um mikroskopische Wärmetransportvorgänge zu bestimmen, welche beispielsweise beim Blasensieden, bei verdampfenden Menisken oder beim Wärmeaustausch an mikrostrukturierten Oberflächen zu finden sind. Diese Vorgänge können aufgrund ihrer Komplexität oftmals nicht durch numerische oder theoretische Modelle beschrieben und müssen demnach experimentell ermittelt werden. Die zwei gebräuchlichen Messmethoden zur Bestimmung von Temperaturfeldern in Flüssigkeiten sind die Flüssigkristall Thermographie (LCT) und die Laserinduzierte Fluoreszenz (LIF). Eine Besonderheit der LCT-Methode ist die mögliche gleichzeitige Erfassung von Geschwindigkeits- und Temperaturfeldern, was deren Einsatz besonders attraktiv erscheinen lässt. Ob die Messmethode jedoch für Messungen mit hoher räumlicher und zeitlicher Auflösung anwendbar ist, war zu diesem Zeitpunkt nicht bekannt. Die Messmethode LIF verspricht aufgrund ihres physikalischen Prinzips eine sehr hohe Auflösung. Aus diesem Grund wurden beide Messmethoden hinsichtlich ihrer räumlichen und zeitlichen Auflösung sowie ihrer Anwendbarkeit charakterisiert. Darüber hinaus wurden Parameter identifiziert, welche die Messgenauigkeit beeinflussen und darauf basierend Verfahren entwickelt, um die Einflüsse zu minimieren.

Um die Messgenauigkeit der LCT-Methode zu bestimmen, wurden Temperaturfelder mit homogener Temperaturverteilung und thermisch induzierter Konvektion gemessen und mit numerischen Ergebnissen verglichen. Der Einfluss des Beleuchtungswinkels wurde für den besonderen Fall der Volumenbeleuchtung ermittelt und mit Ergebnissen aus der Literatur verglichen. Da es viele widersprüchliche Aussagen bezüglich des Verhaltens von Flüssigkristallen (TLCs) bei überhitzung gibt, wurde dies experimentell untersucht. Es wurde herausgefunden, dass Hystereseerscheinungen in dem Temperatur-Farbwertverlauf auftreten,

diese jedoch unabhängig von dem Grad der überhitzung sind und bei ausreichender Unterkühlung wieder verschwinden. Die zeitliche Auflösung der Messmethode LCT ist letztendlich durch das thermische Antwortverhalten der TLCs beschränkt. Da auch hier unterschiedliche Aussagen in der Literatur zu finden sind, wurden diesbezüglich Experimente durchgeführt, welche eine thermische Antwortzeit von 10 ms bei höheren Temperaturgradienten hervorbrachten. Im Hinblick auf die Verbesserung der Messgenauigkeit wurden verschiedene Bildverarbeitungsalgorithmen entwickelt und angewandt. Weiterhin wurde gezeigt, dass Volumenbeleuchtung in Kombination mit entsprechender Bildverarbeitung eine Möglichkeit darstellt, Temperaturfelder in Mini-Strömungen zu messen. Eine Erweiterung des optischen Aufbaus erlaubte darüber hinaus die Messung von 3D-Temperaturverteilungen durch Scannen der Strömung.

Analog zu der LCT-Methode wurde die LIF-Methode hinsichtlich ihrer Anwendbarkeit und Messgenauigkeit untersucht und Potential zur hohen räumlichen Auflösung festgestellt. Um die Abhängigkeit von Beleuchtung und Konzentration zu minimieren, wurde die Zwei-Farb-LIF Methode angewandt. Da ein Nd:YAG Laser aufgrund seiner hohen Pulsenergie und schnellen Pulswiederholrate eingesetzt werden soll, musste eine geeignete Farbstoffpaarung gefunden werden. Aus diesem Grund wurden verschiedene Farbstoffe spektral untersucht und Pyridine 1 und Rhodamine 6G als adäquate Farbstoffe identifiziert. Diese wurden in Zwei-Farb-LIF Messungen eingesetzt und ein gutes Signal-Rausch-Verhältnis wurde erzielt. Ferner konnte gezeigt werden, dass der Einfluss von Beleuchtung und Konzentration erheblich gesenkt wird.

Die Größe der TLC Kapsel, die thermische Antwortzeit und die hohe Messungenauigkeit sind Faktoren, welche die Auflösung der Messmethode LCT einschränken. Eine gleichzeitig räumlich und zeitlich hochauflösende Messung ist daher nicht möglich. Dahingegen hat die Methode LCT entscheidende Vorteile. Es ist möglich mit entsprechenden TLCs Temperaturen im Bereich von hundertstel Kelvin aufzulösen. Ferner können TLCs in Kombination mit Volumenbeleuchtung eingesetzt werden, was von großem Vorteil für Strömungsvisualisierung im Mikrobereich ist. Mit der Messmethode LIF können sehr große räumliche und zeitliche Auflösungen erzielt werden. Die im Rahmen dieser Arbeit gefundene Farbstoffkombination und entwickelte Messaufbau ermöglichen den Einsatz eines leistungsstarken Nd:YAG Lasers und somit zeitlich hochauflösende Messungen bis hin zu 500 Hz mit der verwendeten Messtechnik.

Contents

List of Figures

List of Tables

Nomenclature

Symbol	Meaning	Unit
Roman Letters		
A	amplitude of temperature	K
B	blue	-
b	separation of point images	pixel
C	constant	-
C	volumetric concentration	-
C_{mv}	mass-volume-concentration	kg/m^3
c	specific heat capacity	J/(kg K)
d	diameter	m
d	distance of pinhole centers/ diameter of circumcicle through pinholes	m
d_H	diameter of pinholes	m
d	particle displacement	pixel
f	frequency	1/s
f	focal length	m
g	gravity acceleration ($g = 9.81$ m/s^2)	m/s^2
G	green	-
G	quality grade of signal	-
H	hue	-
h	height	m
h	Planck constant ($h = 6.63 \cdot 10^{-34}$) Js	Js
I	intensity	-

Symbol	Meaning	Unit
J	logarithmic intensity	-
K	constant	-
k	correction factor	-
L	length, focal length	m
L_0	pitch length	m
M	magnification factor	-
M	optical magnification	pixel/m
N	number of images	-
n	refractive index	-
$\dot{q}$	volumetric heat source	W/m^3
r	radius of circumcicle through image points	pixel
R	red	-
R	intensity Ratio	-
R	radius of capillary tube	m
s	color Signal	-
s_{pix}	pixel size	m/pixel
S	saturation	-
t	time	s
t	transmission coefficient	-
T	temperature	K
$\dot{T}$	temperature gradient	K/s
u	velocity	m/s
$\bar{u}$	mean velocity, integrated over flow section	m/s
$\overrightarrow{u}$	velocity in vector form	m/s
w	weighting factor	-
x	Cartesian coordinate	m
X	distance in x-direction parallel to object plane	m
y	Cartesian coordinate	m
y'	optical path length	m
Y	distance in y-direction parallel to object plane	m
z	Cartesian coordinate	m
Z	distance from object plane	m

Symbol	Meaning	Unit

Greek Symbols

α	heat transfer coefficient	$W/(m^2\,K)$
β	opening angle	rad
δ	thickness	m
ϵ	absorption coefficient	-
ζ	temperature sensitivity	1/K
η	dynamic viscosity	Nm·s
Θ	contact angle	rad
ϑ	dimensionless Temperature	-
λ	wavelength	m
ν	kinematic viscosity	m^2/s
ξ	intensity attenuation	-
Π	dimensionless, normalized hue value	-
ρ	density	kg/m^3
σ	surface tension	N/m
σ_H	standard deviation of hue values	rad
σ_T	standard deviation of temperature values	K
σ'	dimensionless, normalized standard deviation	-
φ	angle of inclined light	rad
φ	phase shift	rad
ϕ	quantum efficiency	-
ω	angular frequency	rad/s

Subscript and Superscript

abs	absorption
C	camera axis
cal	calibration
E	entrance
em	emission
ex	excitation
fl	fluorescence
I	image
ill	illumination
L	liquid
LP	longpass
M	mirror
norm	normalized value
opt	optical
P	particle
phos	phosphorescence
pix	pixel
PIT	particle image thermometry
PIV	particle image velocimetry
Pyr	pyridine 1
r	reflection
ref	reference
Rh6G	Rhodamine 6G
s	sink
sens	sensible
set	setpoint value
SP	shortpass

t	transmission
TC	thermo couple
THF	temperature of heating foil
TGl	temperature of glycerin
$\dot{q}$	volumetric heat source

Dimensionless Numbers

$\mathrm{Re} = u \cdot d/\nu$	Reynolds number
$\mathrm{Ca} = \eta/\sigma \cdot \mathrm{d}z/\mathrm{d}t$	Capillary number

Abbreviations and Acronyms

1C-LIF	one-color LIF
2C-LIF	two-color LIF
2C1D-LIF	two-color one-dye LIF
2C2D-LIF	two-color two-dye LIF
3DPIV	three dimensional particle image velocimetry
3D-µDPTV	three dimensional micro defocussing particle tracking velocimetry
AOI	area of interest
CCD	charged coupled device
CIE	International Commission on Illumination
CMOS	complementary metal oxidesemiconductor
FOV	field of view
fps	frames per second

HSI	Hue, Saturation, Intensity
IA	interrogation area
IR	infra red (laser)
LCT	liquid crystal thermography
LED	light emitting diode
LIF	laser induced fluorescence
μPIV	micro particle image velocimetry
μPTV	micro particle tracking velocimetry
NA	numerical aperture
Nd:YAG	neodymium-doped yttrium aluminum garnet
PDE	partial differential equation
PIT	particle image thermometry
PIV	particle image velocimetry
PMMA	poly(methyl methacrylate)
PTV	particle tracking velocimetry
Rh110	Rhodamine 110
Rh6G	Rhodamine 6G
RhB	Rhodamine B
RS	red start
SEE	standard estimate of error
TTL	transistor-transistor logic
UV	ultra violet

Chapter 1

Introduction

Heat transfer mechanisms in micro scales are an important issue for various applications. On the one hand, miniaturized technologies including heat transfer are becoming more and more important and can be found in micro processing, computer chip cooling or lab-on-a-chip applications. Microfluidic systems in particular provide new challenges in micro scales like liquid mixing, pumping, evaporation, combustion or heat exchange. Furthermore, the generally well-known macroscopic transport processes can not be directly transferred to the microscopic processes. This is due to effects like capillary forces which dominate inertial and gravitational forces in micro regions. It is obvious that new research areas arise which address these mostly unexplored phenomena. On the other hand, microscopic heat transfer phenomena do not solely play a role in micro applications. For example, structured surfaces in some cases show enhanced heat transfer compared to smooth surfaces. The higher heat transfer coefficient leads to higher heat flux densities or to lower wall temperatures. This again is very important for many industrial applications in chemical, biological or process engineering. Nevertheless, the exact thermodynamic processes are often not fully understood. However, this is essential for specific improvement of the heat transfer.

For that reason, it is very important to know the heat transfer mechanisms in the liquid, which can be constructed from the temperature and velocity distributions. These can be achieved by theoretical considerations, numerical calculations or experimental measurements. Even if in the future most flow phenomena can be simulated with numerical methods, the numerical models still need to be compared with experiments to prove their validity.

Since most flow phenomena are of a three-dimensional nature, a whole field measurement of the liquid is demanded which is in turn hard to realize. On that account, the transport phenomena have to be transfered into two dimensions for experimental investigations, which can be done using the symmetry of rotation (nucleate boiling, heat transfer in tubes, capillary flows in tubes) or expanding one dimension (heat transfer in gaps, capillary flows in gaps). In doing so, two-dimensional measurement methods can be applied.

Microscopic transport phenomena are often highly dynamic like nucleate boiling or invasive capillary flows. This again requires a measurement technique which is not only able to resolve micro scales but also captures data with high temporal resolution. Methods for measuring temperature or velocity fields are nowadays commonly of optical nature.

Velocity fields in micro flows are obtained by means of the measurement method micro particle image velocimetry (µPIV), achieving high resolution combined with high accuracy. This method was introduced by Santiago et al. [125] and further developed for high temporal resolution and even whole field measurements. Contrary to high resolution measurements of velocity fields, high resolution measurements of temperature fields are not established so far.

The aim of the present work is to obtain a measuring method, which is suitable for two dimensional temperature measurements in liquids with high spatial and temporal resolution. On this account, the measurement methods liquid crystal thermography (LCT) and laser induced fluorescence (LIF) are investigated and applied. Both measurement methods are already established for temperature measurements with relatively low resolution. The possibilities and constraints of the measurement methods are investigated, presented and discussed.

The LCT method offers the possibility to measure velocity fields simultaneously, and beyond that its implementation is rather simple. The question of whether the technique is applicable for high resolution measurements is traced by figuring out the highest temporal and spatial resolution. The measurement accuracy is elaborated and methods are presented to either minimize the error source or enhance the measurement accuracy. Among other things, this is done by comparing measured temperature fields with numerically calculated ones. In addition, temperature and velocity fields which were measured with high temporal and spatial resolution are presented.

As an alternative to the LCT technique, the LIF technique is investigated in detail. Because a dye, dissolved in the liquid, is used as a temperature indicator, simultaneous velocity field measurements are not possible without adding additional tracer particles. Nevertheless, the method promises very high temporal and spatial resolutions because the fluorescence decay time is in the order of magnitude of 100 ns and the size of a dye molecule is in the order of magnitude of 10 nm. Analogous to the LCT method, the possibilities and constraints of the LIF method are pointed out and measured temperature fields are compared with numerical results. Admittedly unsurprising, the main error sources are irregularities in illumination and local dye concentration. On this account, the so-called two-color LIF method is applied, which strongly reduces these effects. The challenge here is to apply the two-color LIF method for high-resolution measurements, which demands a different illumination system than it is typically employed and therefore another dye constellation. Hence, spectral investigations on several fluorescence dyes are conducted. Based on these results, an optical setup, fitting the spectral characteristics of the particular dyes, is realized. The two-color LIF method is further investigated regarding its accuracy and applicability.

In conclusion, both measurement methods are directly compared and the characteristics of the measurement methods are pointed out. The result can be used by the researcher in order to find the most suitable method for his particular application.

Chapter 2

State of the Art

This chapter starts with a brief description of measurement methods beside LCT and LIF (2.1). Section 2.2 deals with the measurement method LCT in which the basics of the method are explained, followed by the presentation of the existing works. Here it is divided into works which are focused on the investigation of the measurement technique and works in which the measurement technique is applied. Similarly, section 2.3 first describes the principle of the measurement method LIF and after that the works in which the method is applied. Additionally, many of the published works are listed in corresponding tables. It should be noted that due to the extensive amount of publications, the tables are not completed but contain a broad spectrum of the published works.

2.1 Temperature Measurements in Liquids beside LCT and LIF

The first attempts to obtain information about temperature distributions in liquids were qualitative measurements such as Schlieren-methods, shadowgraphy or adding dyes. A possibility for obtaining quantitative temperature distributions is the laser phase shift interferometry [133]. Nevertheless, with this technique only temperature fields can be measured, which are integrated in one dimension and therefore are not two-dimensional.

Another rather new technique is the molecular tagging thermometry, which determines the temperature fields from the temperature-dependent phosphorescence lifetime of phosphor molecules in the particular liquid [55].

Temperature fields can also be measured by observing the strongly temperature dependent Brownian motion in liquids [54, 102]. Hohreiter et al. [54] attained a temperature measurement accuracy of approx. ±3 K. Constraints are the measurement accuracy, the demand for small particles (0.7 μm) and the demand for static flows [54].

The dependency of the fluorescence and phosphorescence decay time on the temperature and the development of ultra high-speed cameras lead to new temperature measurement methods [15, 16]. Until now, these methods were only applied for temperature measurements on surfaces and in sprays, although they might be applicable in liquids as well.

2.2 Liquid Crystal Thermography

This section highlights the LCT measurement technique and is divided into a demonstration of how to measure temperature fields in liquids with thermochromic liquid crystals (TLCs) and a review of research activities applying and investigating the measurement technique (table 2.1 - 2.4).

2.2.1 Basics

In this section, the function of LCT is explained, which is divided into the color perception and the physical principle of TLCs. Furthermore, it is explained how TLCs are applied for temperature field measurements in liquids.

Color Perception

Modern color capturing systems (e.g. digital color cameras) use sensor chips and color filters to measure three different wavelength bands, which are located in the red, green and blue color range. That means that for every sensor element, a value for red, green and blue is obtained[1], thereby, a three-dimensional color

---

[1] Exceptions are the so called Bayer matrices. Here every sensor element only has one value, r, g or b. Three dimensional matrices are reconstructed afterwards

space is generated. Every point within this 3D space represents a color, and the color signal s can be described as a linear combination of the basic vectors p_j:

$$s = R \cdot p_1 + G \cdot p_2 + B \cdot p_3 \tag{2.1}$$

The primary color system, established by the CIE (*International Commission on Illumination*), uses the monochrome colors R, G and B with 700 nm, 546.1 nm and 435.8 nm. In the practical sense, the captured image consists of three matrices, namely red, green and blue. Nevertheless, the three-dimensional data is not easy to use as a measurand. On this account, the HSI[2] (hue, saturation and intensity) color space is employed (figure 2.1) where the color is represented as the scalar hue.

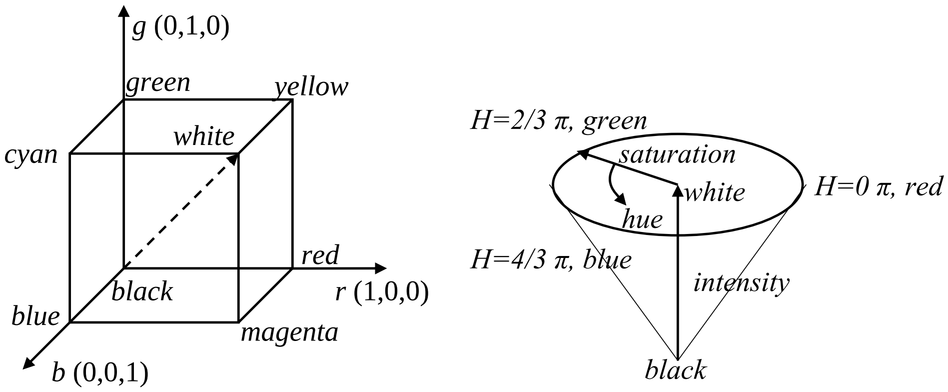

Figure 2.1: RGB and HSI color space

The hue value H actually describes the angle on the HSI cone and is calculated from:

$$\begin{aligned} \text{if } R > B \text{ and } R > G \quad H &= \frac{G - B}{6(R - min(R,G,B))} \\ \text{else if } G > B \quad H &= \frac{2 + B - R}{6(G - min(R,G,B))} \\ \text{else} \quad H &= \frac{4 + R - G}{6(B - min(R,G,B))} \end{aligned} \tag{2.2}$$

From this formula, the hue value H reaches from 0 to 1 which corresponds to $0 - 360°$ in degree or $0 - 2\pi$ in radian. In the present work, the hue values'

---

[2] HSI is also known as HIS, HSV (V means value), HLS (L means luminance)

angular dimension is used in radian. With increasing angle, the hue value passes through red, yellow, green, cyan, blue, magenta and back to red. Therefore, the hue values of red are both 0 and 2π. In praxis, this can cause serious problems in the measurement data analysis. If two pixels next to each other show slightly different colors of red, they can have strongly different hue values. Averaging out of these two pixels would then lead to a mean hue value of π which originally represents the color cyan. A possibility to minimize this error is to employ spatial filters on the RGB images first and then calculate the mean hue values from the RGB values. The purity or intensity of the color is described by the saturation value. In the HSI color space, it is equivalent to the distance from the intensity axis, where no color can be found. The saturation is calculated from

$$S = \frac{1 - \min(R, G, B)}{I} \tag{2.3}$$

with I as intensity calculated from:

$$I = \frac{R + G + B}{3} \tag{2.4}$$

That means, when no saturation 'exists' ($S = 0$), black occurs for $I = 0$ and accordingly white for $I = 1$.

Liquid Crystal Thermography

Liquid crystals show mechanical properties of liquids and optical properties of solid bodies. They are intermediate between amorphic isotropic liquid and crystalline solid, whereas the alignment of their crystalline structure is dependent on pressure, electromagnetic fields, shear stress and temperature. Liquid crystals are categorized into lyotropes, barotropes and thermotropes. Lyotropes change their molecule structure in dependence on the concentration of a specific solvent. As for barotropes, the pressure is the controlling factor for the change of molecule structure. For the temperature measurement, thermotropic or thermochromic liquid crystals are applied, which show a distinctive dependency of their molecule structure on temperature. In the following, only thermochromic liquid crystals are considered whereas it is distinguished between smectic and chiral-nematic liquid crystals. The molecules of smectic liquid crystals are located in one direction in the main but have randomly distributed centers, whereas chiral-nematic liquid crystals show molecules which are twisted perpendicular to a specific orientation axis. In the solid-, respectively crystalline-phase, the molecules, which have a kind of cigar appearance, are allocated parallel to each other (figure 2.2 a)). With increasing thermal energy the liquid crystals reach a point, where they free from their neighbors. They are still fairly aligned in one direction, but not parallel to each other anymore (figure 2.2 b)). The distance of their centers is statistically distributed.

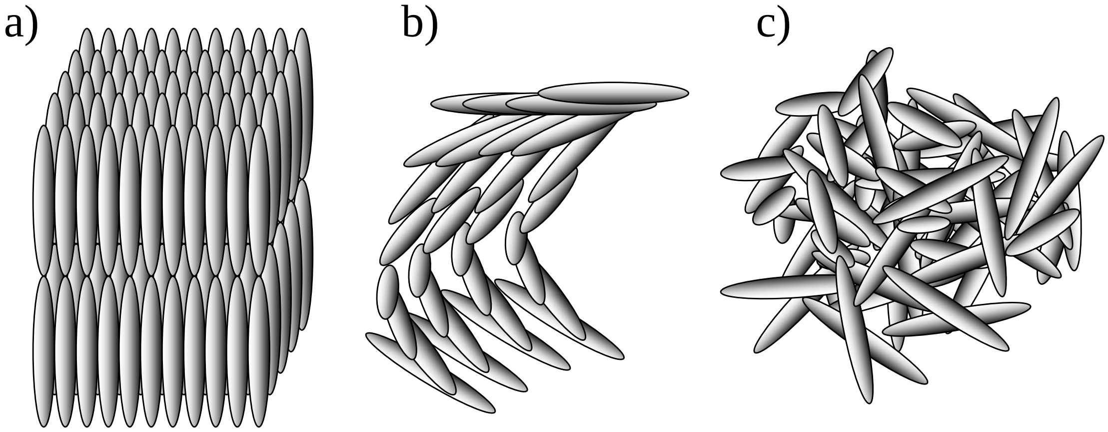

Figure 2.2: Schematic illustration of liquid crystals in different phases: a) crystalline, b) nematic, c) isotropic liquid

A special group of liquid crystals are chiral-nematic, or cholesteric, liquid crystals. In the chiral-nematic phase, the molecules are aligned parallel to each other in molecule layers which have a thickness of approximately 0.3 nm [72]. An additional important property is that the molecule layers are twisted against each other with a defined angle. This twist is temperature dependent and increases with increasing temperature. As a result, a helical structure can be found as shown in figure 2.3.

Chiral-nematic liquid crystals offer a particular optical property: depending on the angle of twist, a certain dominant wavelength of light is reflected, while the other spectral part is transmitted. This is originally caused by interference as shown in figure 2.4. The pitch length describes the distance in direction of the

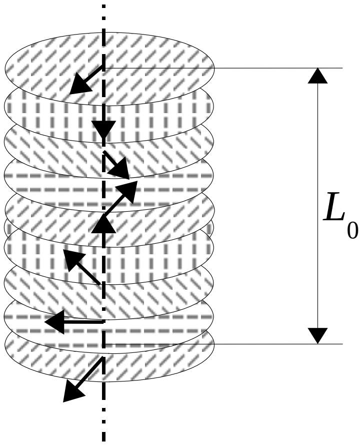

Figure 2.3: Helical structure of chiral-nematic liquid crystals

rotation axis, which is needed for a whole rotation of the molecules' alignment. Using Bragg's law, the reflected wavelength can be calculated from:

$$\lambda_0 = L_0 \cdot n \cdot \sin\varphi \tag{2.5}$$

The reflected wavelength, λ_0, is dependent on the natural number n of pitches, their lengths, L_0, and the angle of inclined light φ. This geometric relation is illustrated in figure 2.4.

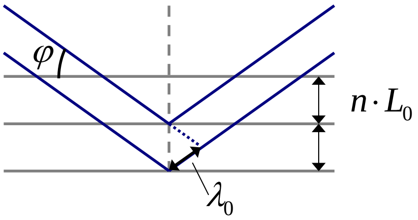

Figure 2.4: Wavelength of reflected light as a function of angle of inclined light and pitch length

In summary, it can be said that with increasing temperature, the angle of twist between the molecule layers expands, which leads to a decreasing pitch length. For this reason, the dominant wavelength of the reflected light decreases with increasing temperature (see figure 2.6). The maximum angle of twist is approximately 40° [72]. With further increasing temperature, the TLCs turn into pure liquid (figure 2.2 c)). The temperature region where TLCs reflect light is called

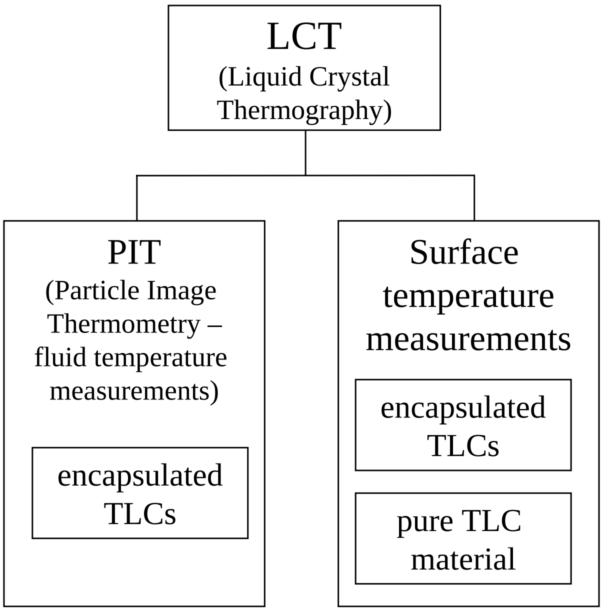

Figure 2.5: Conception of temperature measurements with thermochromic liquid crystals

color play or activity range. At the beginning of the activity range, TLCs reflect red light and with increasing temperature, they pass through yellow, green, cyan, blue and magenta. Outside the activity range, TLCs appear optically transparent because they are either solid (lower temperatures) or liquid (higher temperatures).

TLCs are available for activity ranges with different bandwidths of 0.5 K to 40 K [45]. The start of the activity range is characterized by the red start temperature, the temperature where the color play begins. TLCs with start temperatures ranging from -30 °C to 120 °C are available from [45]. In the experiments, TLCs with the labeling BM/R40C8W/S-40 are employed among others. The labeling is described as follows: BM stands for 'encapsulated', R40 describes the start temperature of the activity range (red start), C8 is the width of the activity range in Celsius and S-40 the concentration of the slurry. According to this, the encapsulated TLCs have an activity range from 40 - 48 °C and are suspended in aqueous slurry with 40 % (Vol).

The conception of temperature measurements employing TLCs is clarified by figure 2.5. LCT is the name of the temperature measurement technique which can be divided into temperature measurements on surfaces or in liquids. For surface temperature measurements, the surface is either coated with pure TLC substance

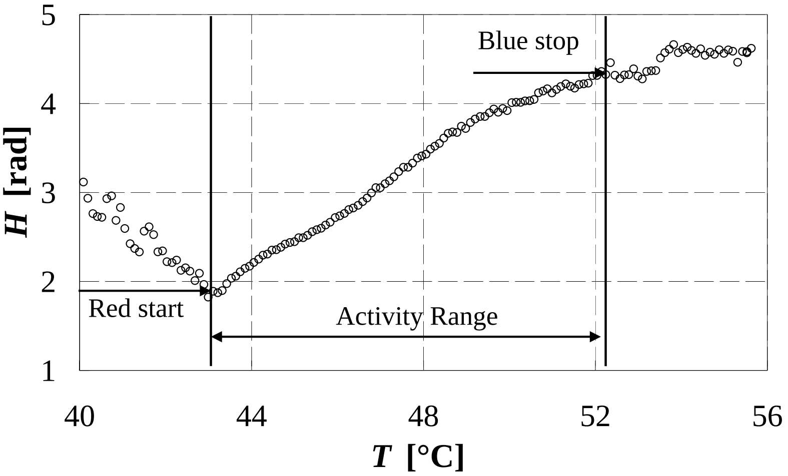

Figure 2.6: Hue values over temperature. With increasing temperature, the hue value is increased. Outside the activity range, the TLCs appear milky

or with encapsulated TLCs. The consistency of pure TLCs is, depending on their temperature, oily or paste-like. They are very affective to environment influences like chemical contamination, oxygen and ultra violet (UV) light. But, in comparison to encapsulated TLCs, they show better reflective properties concerning the intensity and uniformity of the reflected light. This becomes important when measurements with high temporal and spatial resolution are performed [139, 51].

For easier handling, TLCs are microencapsulated with a thin layer of gelatin and gum arabic to protect them from influences mentioned above. Therefore, TLC droplets are suspended in an aqueous solution containing gelatin and gum arabic. The suspension is kept in motion to avoid agglomeration of the TLC droplets. A reduction of the temperature and change of pH of the suspension leads to a reduction of the gum arabic and gelatine solubility with the result that viscose micro droplets of the reactants emerge. These small droplets tend to agglomerate with each other, which ideally leads to a closed shell around the TLC droplets. When the liquid is rapidly cooled, the walls are hardened. An undesired aftermath of the encapsulation process is the loss of signal quality, which becomes noticeable in a lower saturation of the reflected light and a broader spectrum of the reflected wavelengths. It is assumed that the different reflected wavelengths of the TLC capsules are among others induced by the shear stresses emerged during the encapsulation process. The rapid cooling of the TLC capsules leads to a strain in the capsule wall. This results in an enhanced pressure in the TLC core, which again leads to different molecule alignment in the nematic phase. Nevertheless, encapsulated TLCs are easier to handle and offer a higher durability. For surface measurements, they are sprayed on the surface with an airbrush technique or fabricated foils are applied [45].

When suspended particles indicate temperatures and thus temperature fields can be reconstructed, the method is called particle image thermometry (PIT). It should be mentioned that PIT is not exclusively bound to LCT but can also be based on other physical principles. Further, it is possible, that encapsulated TLCs could be used for temperature field measurements in gases, which has not been done yet to the author's knowledge. When encapsulated TLCs are applied for temperature measurements in liquids, a few things need to be considered. The density of the encapsulated TLCs should be similar to the density of the liquid, and the liquid has to be chemically compatible with the encapsulated TLCs. The adequate size of the encapsulated TLCs depends on the application: when velocity field measurements are conducted simultaneously, a minimum size of the capsules is required to achieve proper measurement results. Further, it should be taken into account that small particles follow the flow better and show better thermal response characteristics. On the other hand, larger TLC particles reflect more light.

2.2.2 Review of Research Employing LCT

The first temperature measurements where TLCs were employed were surface temperature measurements. Some of the first, who applied encapsulated TLCs for temperature measurement in liquids were Rhee et al. [115]. In 1984, they investigated a lid-driven flow with a combination of forced and free thermally induced convection. By means of a light sheet, the TLCs are illuminated and photographed with a film camera. Although the photos were studied by human eye, qualitative temperature distributions could be predicted. The first quantitative temperature field measurements were performed by Dabiri and Gharib 1991 [26] who observed a free, heated jet. The images were captured by a video camera and digitalized afterwards, which enabled the quantitative temperature determination. By means of a calibration curve, the temperature could be assigned to the hue values. Based on these key findings, particle image thermometry using encapsulated TLCs was employed for many different kinds of flow phenomena.

Most commonly, free convection within a cuboidal facility was investigated. This includes normal thermal convection induced by two tempered opposed side walls [52, 34], with ice formation [96, 67, 144], in Hele-Shaw-cells [99], Rayleigh-Bénard convection [40, 145, 23], lid driven flows [115, 111], magnetic fluids in magnetic fields [32, 9, 10] or other special applications. The free convection in a narrow gap ($1.1\,x\,10\,x\,10\,\mathrm{mm}^3$) was observed by Heiland et al. [49].

While most of the researchers apply TLCs in encapsulated form, a few authors [52, 67, 23] suspended droplets of pure TLC material directly in the liquid and reported a higher accuracy than authors who used encapsulated TLCs.

Pressure driven flows over wavy surfaces [43, 69] or behind cylinders were observed by [101, 87, 109]. Park et al. [101] were the first to use a relatively high acquisition rate of 30 Hz to investigate the oscillating wake behind a heated cylinder. For the illumination, they used two flash lamps, which fired 15 Hz each, and a CCD (charged coupled device) camera with an imaging acquisition rate of 30 Hz.

Another type of flow, investigated amongst others by [26, 6, 110], is the free jet or plume which has a different temperature than the bulk. The pinch off process of a plume, for example, was visualized in the form of temperature and velocity fields by Pottebaum and Gharib [110].

A rather interesting phenomenon which attracts a certain number of researchers is the heat transfer in a droplet. Observations were performed on droplets in air [135, 116] or droplets in two immiscible liquids [97, 92]. Particularly droplets surrounded by gas led to problems in terms of the curved surface and the changing refraction indexes. Treuner et al. [135] and Richards and Richards [116] presented algorithms to correct these spatial errors. A further challenge is the measurement depth. Especially when the droplet is rather small ([116] observed droplets with $d < 1\,\mathrm{mm}$), the measurement depth should not be bigger than approx. 10 % of the droplet diameter. The problem was solved by [116] using an objective[3] with a high numerical aperture and therefore a small depth of field. With their optical setup, they achieved a spatial resolution of 100 μm.

Pehl [104] used TLCs for temperature measurements under high pressure up to 7000 bar. Prior to the essential investigation, Pehl et al. [105] observed the influence of high pressure on the temperature measurement properties and figured

---

[3] Infinity K2 long-distance microscope

out that the isochromes are linear between the temperature and the pressure. With increasing pressure, the red start temperature of the TLCs is shifted to higher temperatures with approx. 0.015 °C/bar.

A simple method to achieve 3D temperature fields is to scan the measurement volume by moving the light sheet or the camera in the direction of the third dimension. It is obvious that the flow needs to be stationary in this case. This was first reported by Kowalewski et al. [67] and further developed by [34, 86, 23]. The disadvantage is that 3D velocity fields only can be determined when the flow is stationary and no velocity components exist perpendicular to the object plane. On this account, Funantani and Fujisawa [38] used two cameras for stereoscopic PIV. Thus, they achieved real 3D velocity information but only 2D temperature information. Further developing of this technique resulted in scanning the measurement volume and additionally employing stereoscopic PIV. Fujisawa et al. [35] received real 3D temperature and velocity information of a heated plume.

Even though the measurement method is rather simple and therefore applied quite often, many parameters exist which influence the measurement result. On this account, numerous studies were carried out which address the measurement error sources. In the following, some important works in this area are presented which also include the temperature measurement on surfaces because these works are in a sort transferable to the temperature field measurement in liquids. It should be noted that a detailed discussion about the work's results is presented in the particular sections treating the measurement accuracy in chapter 4. At this point, only a short overview is given about the available works.

In 1987, Ireland and Jones [57] investigated the thermal response characteristics of TLCs. With a rather simple setup, they were able to determine the thermal response time of encapsulated TLCs to be approximately 5 ms. Kobayashi et al. [64] did analytic investigations on the thermal response characteristic of encapsulated TLCs. Comparable to Ireland and Jones, Wagner and Stephan [139] investigated the thermal response characteristics of TLC films on surfaces but, unlike Ireland and Jones, Wagner and Stephan used pure TLC material.

Another significant influencing factor on the temperature measurement accuracy is the illumination. The degree of damaging the TLCs caused by ultra violet radiation was investigated by [3, 21, 142]. Anderson and Baughn [3, 4] examined

Author and year	Application T : temperature v : velocity	TLCs, activity range and diameter	Liquid	Illumination and capturing	Field of view
Rhee 84 [115]	Lid driven flow, forced and free convection, T, v (qual.)	N.a., $2 - 50$ µm	Water	Light sheet from projector lamp, film camera	$150x150\,\mathrm{mm}^2$ $450x150\,\mathrm{mm}^2$
Dabiri 91 [26]	Free heated jet, T	$23 - 26\,°C$, 150 µm	Water	Light sheet from xenon lamp, 3CCD camera	$112x163\,\mathrm{mm}^2$
Nishimura 92 [96]	Free convection in cube with solidification, T	$2.5 - 5\,°C$, $6.5 - 9\,°C$ $10 - 15$ µm	Water+Na_2O_3	Light sheet from projector lamp, film camera	$30x50\,\mathrm{mm}^2$
Ozawa 92 [99]	Free convection in Hele-Shaw cell, T, v	$28 - 30\,°C$, $10 - 20$ µm	Various silicon oils	2 halogen lamps from each side, film camera and video camera	Resolution: $2.64x2.58$ mm
Gluckman 93 [40]	Rayleigh-Bénard convection, T, v	$25.5 - 26.5\,°C$, 15 µm	Water	Light sheet from xenon lamp, 3CCD camera	$63x50\,\mathrm{mm}^2$ $63x90\,\mathrm{mm}^2$
Hiller 93 [52]	Free convection in cube, T, v	$20 - 24\,°C$, $2 - 50$ µm	Water/glycerin	Light sheet from xenon flash tube, 3CCD camera	$50x50\,\mathrm{mm}^2$
Kowalewski 93 [67]	Free convection in cube with solidification, 3D T, v	$27 - 32\,°C$, $20 - 23\,°C$ pure, ≈ 50 µm	Water, glycerin water/glycerin	Light sheet from xenon flash tube, 3CCD camera	$38x38\,\mathrm{mm}^2$
Treuner 95 [135]	Temperature distribution in large droplets, T, v	$25 - 32\,°C$, N.a.	Water/glycerin	Light sheet from xenon lamp, two film cameras, background illum. and 3CCD camera	$\approx 15x15$ mm
Nozaki 95 [97]	Heat transfer in droplet in immiscible liquid, T	$37 - 45.6\,°C$, $42 - 43.7\,°C$, 15 µm	Water with TLCs in methylphenyl silicone oil	Light sheet and volume illum. from halogen lamp, 3CCD camera	$\approx 8x8$ mm
Prasad 96 [111]	Lid driven flow, forced and free convection, T, v (qual.)	$23 - 25\,°C$, $50 - 100$ µm	Water	Light sheet from xenon lamp, film camera	$150x150\,\mathrm{mm}^2$ $450x150\,\mathrm{mm}^2$
Richards 98 [116]	Temperature distribution in evaporating droplets, T	$30 - 35\,°C$, $5 - 15$ µm	Water	One axis illumination from ring light, 3CCD camera	$\approx 1x1\,\mathrm{mm}^2$
Mochizuki 99 [92]	Heat transfer in droplet in immiscible liquids, T integrated	N.a., 15 µm	Water droplets in silicone oil	Volume illumination from 2 halogen lamps, 3CCD camera	
Pehl 00 [105]	Temperature measurements under high pressure, T	Depends on pressure, $10 - 20$ µm	Water	Light sheet from xenon lamp, 3CCD camera	$6x8\,\mathrm{mm}^2$
Fujisawa 00 [34]	Free convection in cube 3D T, v	$27.7 - 30\,°C$, 10 µm	Water	2 light sheets from 2 stroboscopes, 3CCD camera	$60x56\,\mathrm{mm}^2$
Kowalewski 00 [68]	Temperature field around bubble in low pressure, T, v	$36 - 39\,°C$, 25 µm	Water	Shadowgraphy, light sheet from halogen lamp, 3CCD camera	$\approx 10x15\,\mathrm{mm}^2$

Table 2.1: Overview of works where LCT measurement technique was applied to fluid flow configurations, 1984-2000

Author and year	**Application** T **: temperature** v **: velocity**	[TLCs, activity range **and diameter**	Liquid	Illumination and capturing	Field of view
Park 01 [101]	Wake behind heated cylinder, T, v	$26 - 29\,^{\circ}C$, 40 µm	Water	Light sheet from 2 xenon flash tubes, 3CCD camera	$50x40\,\mathrm{mm}^2$
Lutjen 01 [86]	Free convection in cube, 3D T, v	$24 - 29\,^{\circ}C$, 40 µm	Glycerin	Light sheet from xenon arc lamp, 3CCD camera	$76.2x76.2\,\mathrm{mm}^2$
Kowalewski 01 [66]	Filling of cavity, T, v	N.a., 50 µm	Glycerin	Light sheet from halogen tube lamp, 3CCD camera	$38x113\,\mathrm{mm}^2$
Funatani 02 [38]	Rayleigh-Bénard convection, T, 3D v	$29.6 - 32\,^{\circ}C$, PIV: 50 µm, PIT: 10 µm	Water	Light sheet from stroboscope, 2x3CCD cameras	$60x60\,\mathrm{mm}^2$
Günther 01 [41]	Flow over wavy walls, T, v	$33.8 - 35.1\,^{\circ}C$, 19.75 µm	Water	Light sheet from metal halide lamp, 3CCD camera	$33x25\,\mathrm{mm}^2$
Ciofalo 03 [23]	Rayleigh-Bénard convection, 3D T, v	$19.2 - 21\,^{\circ}C$, pure ≈ 100 µm	Glycerin	Light sheet from flash lamp, film camera	$120x60\,\mathrm{mm}^2$
Pottebaum 04 [110]	Pinch-off process of buoyant plume	$25.8 - 28.0\,^{\circ}C$, 100 µm	Water/glycerin	Light sheet from 2 xenon flash lamps, 3CCD camera	$97.6x73\,\mathrm{mm}^2$
Kruse 05 [69]	Flow over wavy surfaces, T, v	$29 - 30\,^{\circ}C$, 20 µm	Water	Light sheet from stroboscope, laser light sheet for PIV, 3CCD camera	$36x45\,\mathrm{mm}^2$
Fujisawa 05 [35]	Turbulent Rayleigh-Bénard convection, 3D T, v	$28 - 30\,^{\circ}C$, 10 µm	Water	Light sheet from 2 metal halide lamps, stereo PIV with 2x3CCD cameras	$22x22\,\mathrm{mm}^2$
Filar 06 [32]	Thermal and magnetic induced convection in cylinder, T	$18 - 21.7\,^{\circ}C$	Glycerin	Light sheet from LEDs, 3CCD camera	
Bednarz 06 [9]	Thermal and magnetic induced convection in cube, T	$19.2 - 20.7\,^{\circ}C$, N.a.	Water/glycerin	Light sheet from projector lamp, 3CCD camera	$35x32\,\mathrm{mm}^2$
Li 06 [81]	Thermal induced convection, 4 heated walls, qual. T, v	$28.5 - 32.5\,^{\circ}C$, N.a.	Water	Light sheet from white light source or laser (PIV), 3CCD camera	$368x98\,\mathrm{mm}^2$
Li 07 [82]	Thermal induced convection, facility divided by plate with hole , qual. T, v	$29 - 39\,^{\circ}C$, $20 - 40$ µm	Water/glycerin	Light sheet from high power white light source, 3CCD camera	$38x38\,\mathrm{mm}^2$
Heiland 06 [49]	Thermal convection in gap, T, v	$28 - 34\,^{\circ}C$, 40 µm	Water	Light sheet from 2 xenon flash lamps, 3CCD camera	$67x51\,\mathrm{mm}^2$
Bednarz 08 [11]	Thermal induced free convection in gap, T	$19.7 - 23.7\,^{\circ}C$, N.a.	Water	Light sheet from projector lamp, 2x3CCD cameras	$300x15\,\mathrm{mm}^2$

Table 2.2: Overview of works where LCT measurement technique was applied to fluid flow configurations, 2001-2008

the influence of several illumination sources on the temperature measurement accuracy and figured out that an illumination source with a broad spectrum leads to the best results.

It is already known that the illumination angle (meaning the angle between the illumination and camera axis) has direct influence on the indicated color and therefore on the temperature. This was observed in liquids by [97, 42, 37] and on surfaces by [30, 12, 21]. A dependency of the activity range on the illumination angle has been observed by [97, 42, 37]. Further, it was found that the measurement accuracy is higher at smaller angles. A more detailed discussion of these works can be found in section 4.3.1.

When TLCs are heated above their activity range, hysteresis in the temperature-hue-relation occurs which leads to an additional measurement error. The effect of hysteresis was examined and documented by [142, 8, 120, 2, 130, 51, 6, 7]. The results of these works are discussed in detail in 4.2. Aging effects occur when TLCs are kept for a longer time period at a certain temperature. These effects lead to irreversibilities in the temperature hue curve during heating and cooling and were among others observed by [51, 142].

Different kinds of color space transformation to obtain temperatures from the color images were applied by Hay and Hollingsworth [47]. Fujisawa [36] suggested using the saturation and intensity values in addition to the hue values to enhance the measurement accuracy. Using a neural network instead of the hue value is suggested by [76, 101, 44]. Roesgen and Totaro [117] use a linear transformation to determine the temperature from the RGB values.

To overcome the relatively high measurement uncertainty of encapsulated TLCs, elaborate data analysis is required. Behle et al. [12] and Farina et al. [30] analyzed the influence of different averaging techniques on the measurement accuracy.

2.3 Laser Induced Fluorescence

Similar to the previous chapter about LCT, an explanation of the basics of the measurement technique is first given, followed by a review of works dealing with LIF (tables 2.6 and 2.7).

Author and year	Investigation	Employment of TLCs	Illumination and capturing	Accuracy/results
Ireland 87 [57]	Thermal response characteristics of encapsulated TLCs	Encaps. (10 µm) TLCs coated on surface	White light source, photo diode for high temporal resolution	Thermal response time: few ms
Camci 92 [18]	Influence of illumination intensity, illumination angle	Encaps. TLCs coated on surface	Incandescent light source, 3CCD camera	Larger illumination angles result in higher uncertainty
Farina 94 [30]	Influence of camera configuration, background light, illumination angle	Encaps. $(10 - 15\,\mu\text{m})$ TLCs coated on surface	Ring light, 3CCD camera	Calibrated system shows less dependency on illumination
Nozaki 95 [97]	Influence of illumination angle, comparison between light sheet and volume illumination	Encaps. (15 µm) TLCs suspended in silicone oil	Halogen lamp, light sheet and volume illumination, 3CCD camera	Activity range decreases for increasing illumination angle
Behle 96 [12]	Influence of illumination angle and camera configuration	Encaps. and pure TLCs coated on surface	Halogen lamp, ring light, 3CCD camera	Hue value increases with increasing illumination angle, ±5.3% accuracy at $5\,x\,5$ pixels averaging
Hay 96 [47]	Influence of RGB to HSI transformation	Pure TLCs coated on surface	Fluorescent light bulbs, 3CCD camera	Higher uncertainty at higher temperature ranges
Hay 98 [48]	Influence of illumination angle	Encaps. (20 µm) TLCs coated on surface	Fluorescent light bulbs, 3CCD camera	Less influence of illumination angle for dimensionless temperatures
Sabatino 00 [120]	Local calibration, hysteresis effects	Encaps. $(10 - 15\,\mu\text{m})$ TLCs coated on surface	Halogen light bulb, film camera	Decrease of bias error due to local calibration
Chan 01 [21]	Influence of illumination angle	Encaps. $(10 - 15\,\mu\text{m})$ TLCs coated on surface	Halogen lamp, ring light, 3CCD camera	Viewing angle calibration technique minimizes effect of illumination angle
Fujisawa 01 [36]	Different methods for temperature determination	Artificial color images	-	Using H, S and I for temperature determination leads to better results

Table 2.3: Overview of works which address to measurement technique LCT, 1987-2001

Günther 02 [42]	Influence of illumination angle	Encaps. (20 µm) TLCs in water/glycerin	Light sheet from metal halide lamp, 3CCD camera	Activity range depends on test liquid and illumination angle
Bakrania 02 [7]	Hysteresis effects	Pure TLCs coated on surface	Halogen light bulb, 3CCD camera	Hysteresis disappears when cooled below start temperature
Fujisawa 04 [37]	Influence of illumination angle, additional PIV particles	Encaps. (10 µm) TLCs in water	Light sheet from xenon flash lamp, 3CCD camera	Lowest uncertainty at angle of 20°, ideal mixture of TLC/PIV particles
Wiberg 04 [142]	Influence of illumination intensity, film thickness, TLC aging, digital resolution	Encaps. TLCs coated on surface	Halogen lamp, 3CCD camera	Illumination intensity and aging lead to change of hue response, thicker films show higher accuracy
Anderson 04 [2]	Hysteresis effects	4 different kinds of encaps. TLCs coated on surface	Fluorescent light source, 3CCD camera	Super-heating leads to reduction in intensity, hysteresis value depends on super-heating temperature
Anderson 05 [3, 4]	Influence of illumination source	Encaps. TLCs coated on surface	Tungsten filament lamp, tungsten/halogen lamp, fluorescent lamp with and w.o. UV filter, full spectrum fluorescent lamp, 3CCD camera	Light sources with broad spectrum lead to best accuracy (white balance of camera was not changed), UV damages TLCs
Wagner 06 [139]	Thermal response characteristics of pure TLC substance	Pure TLCs coated on surface	White light source, high speed camera for high resolution	Thermal response time: $< 10\,\mathrm{ms}$

Table 2.4: Overview of works which address to measurement technique LCT, 2002-2006

2.3.1 Basics

The physical phenomenon fluorescence is influenced by a certain number of parameters. In the following, at first the physical principle of fluorescence is explained, followed by a description of the factors, which take influence on the fluorescence.

Fluorescence

Fluorescence is the spontaneous emission of light by excited molecules. When applying laser induced fluorescence, the molecules are excited by electro magnetic radiation (laser light) and turn into a state of higher energy. Thereby the kinetic energy of the electrons is enhanced when moving to higher, but unstable electrical states (see figure 2.7). Within the electrical states (singlet and triplet states) they dissipate energy in the form of vibrational relaxation until they reach the lowest energy level of the particular singlet and triplet state. The emission of radiation occurs when the electrons move from the singlet or triplet to the ground state. In principal, there are three possibilities for the energy reduction of the molecule. In most cases, the molecule emits light, which is called fluorescence and happens within a few nanoseconds. However, when molecules interchange with neighboring molecules, the energy is released without emitting photons, which is called quenching. The third and also the most unlikely case is the intersystem crossing, where the electron moves to the triplet state with an according energy level. The electron then loses further energy through vibrational relaxation and finally emits light when moving back to the ground state. This process is called phosphorescence.

From the energetic point of view, the emitted photon can only have the same or a smaller amount of energy than the absorbed photon - the residual energy is dissipated by the vibrational relaxation. This results in a redshift of the emitted light which is also called Stokes shift.

The fluorescence intensity I_{fl} can be described by

$$I_{fl} = I_0 \cdot C \cdot \phi \cdot \epsilon \tag{2.6}$$

and is linearly dependent on the illumination intensity I_0, the dye concentration C, the quantum efficiency ϕ and the absorption coefficient ϵ. The quantum

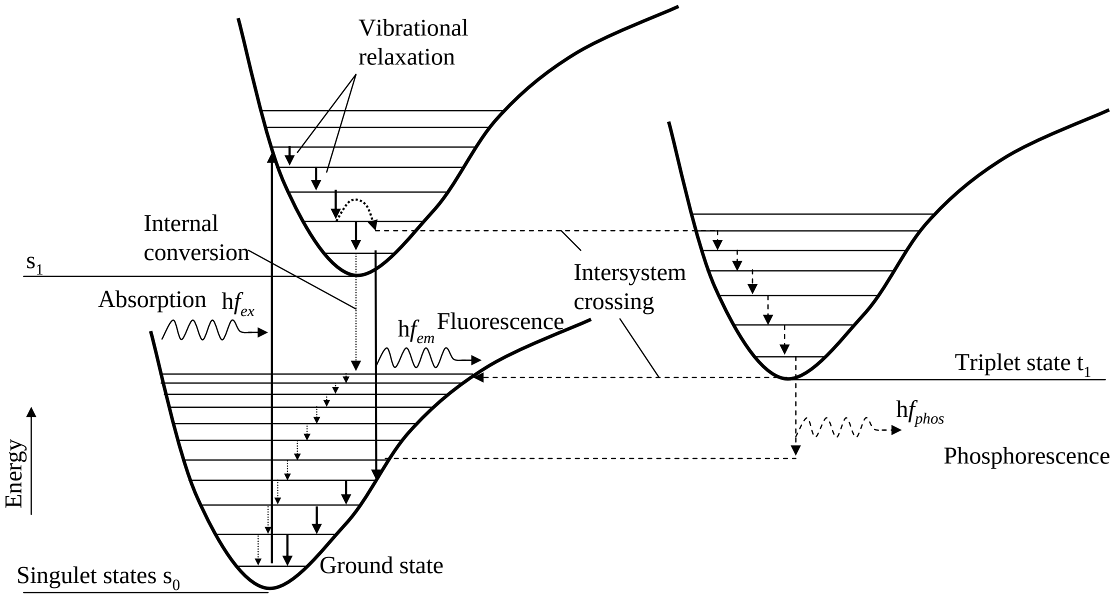

Figure 2.7: Energy state diagram of a fluorescence dye. Three possible energy transfers are shown: fluorescence - solid line, internal conversion - dotted line, intersystem crossing and phosphorescence - dashed line. For simplification, further possible energy states and singlet and triplet states are left.

efficiency stands for the number of emitted photons divided by the number of absorbed photons. The absorption coefficient describes the ability of the dye to absorb photons and is mainly dependent on the wavelength of the exciting light.

Fluorescence Dyes

Fluorescence dyes are organic molecules with aromatic ring structures, which possess delocalized electrons that can be easily excited by photons. Fluorescence dyes exhibit characteristic absorption and emission spectra. To design the optical setup, it is important to know these spectra. A group of dyes, which are often used for LIF, are rhodamines. They are commonly soluble in ethanol and water and show quantum efficiencies close to 100 %. The size of the fluorescenct molecules is approximately 10 nm [5].

Quenching and Photobleaching

As already mentioned, quenching occurs when excited molecules interchange with neighboring molecules and their energy emission is non-radiant. The interchange with the neighboring molecules can be of a different kind:

- **Collisional interaction** brings collisional partners into electric ground state
- **Energy transfer** without physical contact of the molecules
- **Oxygen** works as a catalyst and electrons move to triple state
- **Energy conversion** within the fluorescence molecule, also called internal conversion

Quenching is a reversible process. After the non-radiative energy dissipation, the fluorescence molecule can be excited again. In equation 2.6 the effect of quenching can be found in the quantum efficiency Φ.

Photobleaching is caused by intense illumination and happens to molecules which are located in the triple state. The molecules are then converted into colorless leuco combounds, which are no longer able to fluoresce [73]. Thus, photobleaching is - compared to quenching - irreversible. The occurrence of photobleaching also depends on the dye, which means that some dyes show higher susceptibility for

	Quenching	**Photobleaching**
Influencing factors	Dye molecule Polarity of solvent pH-value of solvent Temperature	Dye molecule Illumination intensity Exposure time
Consequences	Reversible reduction of fluorescence intensity	Irreversible reduction of fluorescence intensity
$\Rightarrow$	Principle of temperature and pH measurement	Error source for temperature and pH measurements

Table 2.5: Comparison of phenomena quenching and photobleaching

photobleaching than others. At low excitation light intensity, low dye concentration and short duration of illumination, the photobleaching effects are negligible [140]. However, at high illumination intensity and/or illumination duration, photobleaching occurs and leads to significant measurement errors. According to this, photobleaching should be avoided by carefully configuring the illumination setup. To clarify the difference between quenching and photobleaching, which is frequently mixed up, the main differences are shown in table 2.5.

Another kind of bleaching is the chemical bleaching, where the dye molecule reacts with another molecule. This effect is irreversible as well.

Solvent

The solvent influences the absorption and emission spectra and the quantum efficiency. A solvent with a high polarity leads to a stabilization of the excited molecule which has a dipole character. The result is a longer dwelling time of the molecule in the excited state. This again enhances the probability of non-radiative quenching due to collision with neighboring molecules and reorientation of neighboring molecules (solvent relaxation). The solvent relaxation leads to an electron transfer from a lower energy level of the excited state, so that the energy of the emitted photon is also lower (red-shift of the emission spectrum). Again, the collisional quenching leads to a decrease of the emitted light. In praxis, a dye dissolved in water shows a red-shifted spectrum and a lower fluorescence intensity but also a higher temperature sensitivity compared to the same dye in ethanol.

pH-Value

Another factor which influences fluorescence is the pH-value of the solvent. Acidic liquids have more H^+ free radicals which change the fluid properties. Accordingly, basic liquids provide more OH^- oxidants. Both kinds of liquids lead to quenching effects. A red-shift and a peak increase of the emission spectrum of rhodamine B in N-octanol at decreasing pH-value was observed by [132].

Concentration

According to 2.6, the concentration shows linear influence on the fluorescence intensity. When the optical way of the exciting light is considered, the fluorescence intensity decreases exponentially with increasing optical path length, y'. This is described by the Beer-Lambert-law

$$\frac{I_{fl}(y)}{I_{ill}} = exp\left[-\int_0^y \epsilon \cdot C(y')dy'\right]. \tag{2.7}$$

When the absorption and emission spectra overlap, a part of the spectrum of the emitted light is re-absorbed. When applying planar LIF measurement method, the fluorescence dilution is normally partially illuminated (e.g. with a light sheet). The fluorescence light then has to cover a certain distance through the dilution until it finally reaches the sensor. This distance is called absorption path. The fluorescence intensity, captured from the sensor, also depends on the absorption path length. Even when the spectra do not overlap, a certain part of the emitted light is absorbed by the liquid. This absorption is of course smaller than self absorption due to overlapping spectra. If the length and dye concentration of the absorption path remain more or less constant, the self-absorption also remains constant and does not affect the measurement.

When the dye concentration is increased beyond a certain point, saturation occurs; not all dye molecules can absorb light anymore. With a further increase of the dye concentration, the fluorescence intensity is decreased and red-shifted, which is mainly caused by the self-absorption. The self-absorbed fluorescent light has a lower photon energy (higher wavelength) than the regular exciting light. The emerging emitted light from the self-absorption then has a higher wavelength. Further, the intensity of the fluorescent light is decreased due to additional quenching effects. On this account, the dye concentration should be kept as small as possible, which is also advantageous with respect to the homogeneous dye distribution within the liquid.

Temperature Measurement using the Fluorescence Principle

Some fluorescence dyes (e.g. rhodamine B) show distinctive temperature dependent fluorescence intensities. The reason for this effect is mainly the temperature dependency of the quantum efficiency. With increasing temperature, the quantum efficiency is decreased which is due to increasing quenching effects. This effect is caused by higher kinetic energy of the molecules. Temperature changes can also lead to a shift of the absorption spectrum, which possibly results in a shift of the fluorescence intensity. Depending on the wavelength of the exciting light, the fluorescence intensity can increase or decrease with increasing temperature. A dye, which shows positive fluorescence intensity increase over temperature, probably undergoes this effect. At moderate temperatures ($0 - 100\,^{\circ}\mathrm{C}$), the temperature sensitivity of the absorption coefficient is negligible [79].

To measure the temperature of a liquid, the fluorescence dye is dissolved in the liquid, the measurement volume is excited with light and the fluorescent light is captured with an according sensor. Furthermore, the excited light needs to be separated from the fluorescence light so that the fluorescence intensity is captured exclusively. This can be easily realized with optical long-pass filters. To measure planar temperature fields, a spatial resolving sensor is needed like a commercial camera. Using a pulsed laser for exciting the dye has the advantage, that the photobleaching effects are minimized, and high temporal resolution measurements become possible. This method is called one-color LIF and is abbreviated as 1C-LIF in the following. 1C-LIF can be expanded to the two-color (2C) LIF method. Here it is distinguished between the two-color LIF method using two dyes (2C2D-LIF) and using one dye (2C1D-LIF). The reason for the more extensive 2C-LIF method is the enhancement of the measurement accuracy, which is explained as follows.

One-Color LIF

The measured signal S can be described as a product from the fluorescence intensity, I_{fl}, and an optical constant K_{opt}, which mainly represents the sensitivity of the camera and is calculated from

$$S = K_{opt} \cdot I_{fl} = K_{opt} \cdot I_{il} \cdot C \cdot \phi \cdot \epsilon. \tag{2.8}$$

Ideally, K_{opt} is independent from the captured illumination intensity I_{il}. The 1C-LIF method can be employed for temperature measurements subjected to some conditions: Only the quantum efficiency and the absorption coefficient are temperature dependent, the dye concentration is homogeneous and the illumination is temporally constant. If these factors are fulfilled, 2D temperature measurements can be conducted when applying a spatial resolvable optical setup.

Two-Color LIF

Because the fluorescence signal shows a strong dependency on the concentration and the illumination intensity, the 1C-LIF method does not work for applications, where the concentration and the illumination are not constant. Therefore, a reference image is used, which provides the information of the illumination intensity and the concentration exclusively and shows no temperature information. The temperature field is then obtained from the ratio of the temperature sensitive and the reference image. This can be realized as follows.

Two-Color Two-Dyes LIF (2C2D-LIF) The reference signal is achieved by using an additional dye, which shows an insignificant temperature sensitivity. The absorption spectra must overlap, so that both dyes can be excited by a monochrome laser (see figure 2.8). The separation of the two spectral bands is carried out with optical filters and mirrors, and two cameras can be applied to capture the bands. The ratio is calculated from

$$R = \frac{S_{sens}}{S_{ref}} = \frac{K_{opt,sens} \cdot C_{sens} \cdot \phi_{sens} \cdot \epsilon_{sens}}{K_{opt,ref} \cdot C_{ref} \cdot \phi_{ref} \cdot \epsilon_{ref}}. \tag{2.9}$$

This method is independent from the illumination intensity. The dependency on the dye concentration remains because two different dyes are used. If the dye concentration is not homogeneous within the measurement volume, the

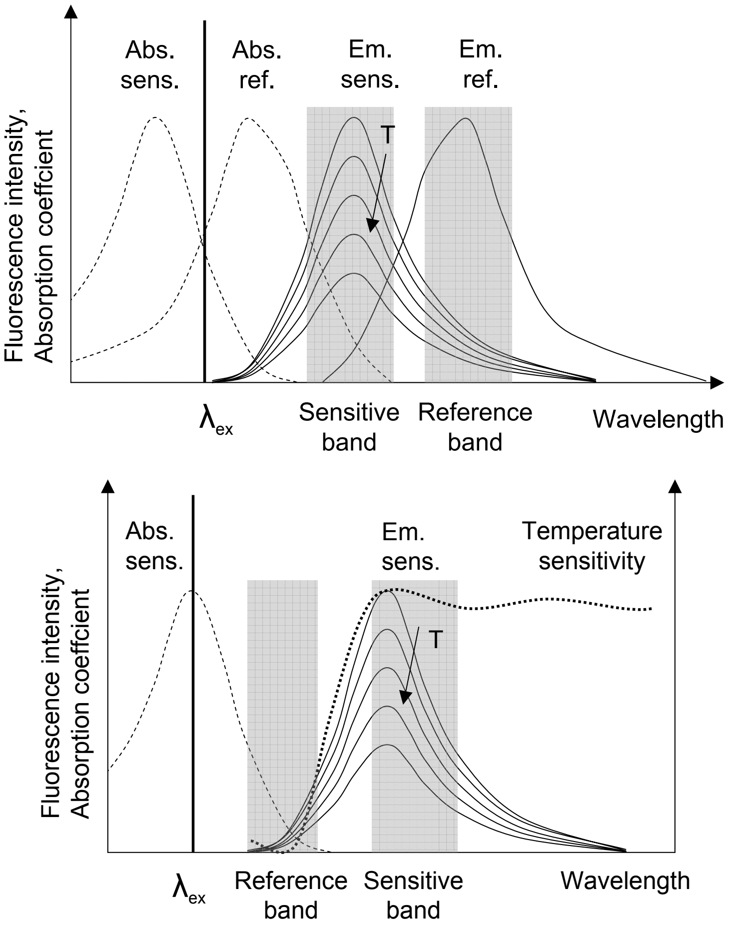

Figure 2.8: Top: principle of 2C2D-LIF. Sensitive and reference emission spectra are captured selectively. Bottom: principle 2C1D-LIF: Only one dye with wavelength dependent temperature sensitivity is used. Reference band shows lower temperature sensitivity than sensitive band

temperature signals are strongly defective. A possibility to minimize this error is the use of only one dye.

Two-Color One-Dye LIF (2C1D-LIF) The principle of the 2C1D-LIF method is to obtain the sensitive as well as the reference image from one dye. Therefore, the dye must show a wavelength dependent temperature sensitivity in the emission spectrum (see figure 2.8). The ratio is then calculated from

$$R = \frac{S_{sens}}{S_{ref}} = \frac{K_{opt,sens} \cdot \phi(\lambda_1) \cdot \epsilon(\lambda_1)}{K_{opt,ref} \cdot \phi_(\lambda_2) \cdot \epsilon(\lambda_2)} \tag{2.10}$$

where the concentration and illumination factors are crossed out.

2.3.2 Current Research Activities

LIF can be employed in different ways for temperature measurements in liquids. It should be noted that beside the studies dealing with temperature field measurements in liquids, also studies on pH or concentration field measurements are presented. These measurement methods show a high similarity and therefore can be transferred easily to another specific application.

Two-dimensional temperature measurements using LIF were already performed by Romano et al. in 1989 [118]. They measured the surface temperature of a metal plate heated from the other side by a laser beam. The surface was coated by a polymer containing rhodamine B, which enabled temperature measurements with a accuracy of 1 K. By using a microscope, a high spatial resolution of 1 µm could be achieved.

The first two-dimensional temperature measurements in liquids were performed by Sakakiabara et al. in 1993 [123]. 1C-LIF was applied to investigate a flow through a cylindrical tube, whereas Rhodamine B was dissolved in water and illuminated with an Argon-Ion laser. A temperature sensitivity of 2.3 %/K was found. In addition to the temperature fields, velocity fields were measured with the PIV method, applying a second camera. A jet impinging on a horizontal plate was observed by [124] where two cameras were used to measure the velocity fields additionally.

Coolen et al. [24] investigated the accuracy of temperature measurements using the 1C LIF principle. The measured temperature fields were compared with numerically calculated temperature fields. A cuboidal facility was used and rhodamine B, dissolved in water, was illuminated by a Nd:YAG laser. The laser power was measured by means of a power meter. The authors observed a fluctuation of the laser pulse intensity of 3%, which neccessitates temporal averaging over 30 images. Additionally, diverse error sources of the LIF method were documented. These are photobleaching, which has a major influence on the accuracy, pH change of water and self-absorption, which have both a minimal influence. The greatest part of the uncertainty of 1.7 K was credited to the variation of the dye concentration in water and the image capturing namely random noise of the CCD camera and the frame grabber. A further, non marginal effect was found in shadography due to the temperature dependent change of the refractive index of water.

Two dimensional temperature measurements of a wake behind a heated cylinder were conducted by Seutiens et al. 2001 [128], who also used Rhodamin B as temperature sensitive dye and a Nd:YAG laser for illumination.

Ross et al. [119] applied LIF for temperature measurements in a t-shaped micro mixer. Because they used volume illumination, only the bulk temperatures could be measured. This problem was solved by Yoon and K. C. Kim 2005 [150] who realized a micro light sheet with a thickness of approximately 5 μm. Thus, they were able to measure true two-dimensional concentration fields of ethanol respectively methanol with a high accuracy. Another possibility for measuring two-dimensional fluorescence fields in spite of using volume illumination is the use of a confocal microscope. This has been carried out by Ichiyanagi et al. in 2007 [56], who measured pH and velocity fields in a t-shaped micro mixer. Using a three-chip color camera enabled the simultaneous employment of PIV. Hoffmann et al. [53] used a confocal microscope in combination with a scanning device. On this account, they were able to measure three-dimensional concentration and velocity fields in a t-shaped micro mixer. It should be noted that the flow needs to be stationary for such measurements.

Because of the high error-proneness of the 1C-LIF method for illumination and concentration inhomogeneities, effort has been put into the development of LIF methods using two or even more spectral bands to minimize the above mentioned error sources. Sakakiabara and Adrian [121] used rhodamine B and rhodamine 110 in combination with an argon-ion laser to measure three dimensional temperature distributions of a Rayleigh-Bénard convection. The third dimension was achieved by scanning the liquid volume with a laser light sheet. Two CCD cameras were used to capture the temperature sensitive and non-sensitive spectral bands. Copetta and Rogers [25] did intense investigations on nine different fluorescence dyes with the background to find suitable dyes for temperature and pH measurements in water. While they used two cameras for the pH measurement, only one camera was applied for the temperature measurement. The capturing of the different wavelength bands was realized with sliding color filters in front of the camera. The same principle, namely the sliding filters, was used by Kim and Kihm in 2001 [61], who measured the temperature distribution in a channel with a width of 1 mm. Funantani et al. [39] applied a three-chip CCD camera to measure the velocity and temperature field of a heated plume simultaneously. The scattered light of the particles was captured by the blue chip, while the green and red chip captured the non-sensitive, respectively the temperature sensitive, spectral bands. A further improvement of the measurement accuracy was achieved by Sakakiabara [122], who used two digital cameras with a high gray scale resolution (14 bit) and developed a deconvolution algorithm to enhance the congruence of the two images. Simultaneous measurements of temperature and velocity fields were done by Kuhn [70], who used three cameras. Two cameras were employed for 2C-LIF and one camera for PIV measurement.

While the two-color measurements described so far used one sensitive and one non-sensitive dye, a dye can be applied instead which exhibits a wavelength-dependent sensitivity. This was first conducted by Lavieille et al. [75], who used rhodamine B, the 488 nm band of an argon-ion laser and two photomultiplier tubes. This technique was expanded in using three photomultiplier tubes, which further reduces the effect of re-absorption. Nevertheless, when using photomultiplier tubes, only zero-dimensional measurements are possible. Bruchhausen et al. [17] used rhodamine B, a Nd:YAG laser and two CCD cameras for two color LIF with one dye. Thereby, they were able to measure the temperature distribution of a heated free jet.

In table 2.6, a general overview of works including LIF measurement technique is given. It is divided into 1C-LIF, 2C2D-LIF and 2C1D-LIF and special applications. The particular sections are sorted chronologically. Further the achieved measurement accuracy is not named because it is less meaningful. There is no unique method which represents the measurement accuracy, and it would be to extensive to describe each author's modality of the measurement accuracy.

2.4 Aim and Motivation

Most flow phenomena, which were investigated by employing LCT, do not put large demands on the measurement technique because both the temporal and spatial resolution are relatively low. When LCT is applied for measurements with high spatial and temporal resolution, some procedures and technologies are quite different to low resolution measurements and thus open questions remain. Most LCT applications in macro scales use light sheets for illumination which is often not possible for micro/mini applications. On the one hand, the energy density of white light is not high enough to create a micro light sheet, which provides enough light for illumination. On the other hand, many micro/mini flow applications do not offer the possibility for illuminating from the side. Furthermore, the information density of LCT is significantly lower for high resolution applications. This again leads to a reduction of the measurement accuracy and requires special data analysis. Another ambiguous point is the thermal response characteristic of the encapsulated TLCs. While the pure TLC substance has been investigated by Wagner and Stephan [139], the thermal response time for encapsulated TLCs is not fully clarified yet. Although Ireland and Jones [57] provided valuable results for encapsulated TLCs coated on a surface, a lot of questionable data exists in the literature. Further, the thermal response characteristic observed by [57] was done with encapsulated TLCs in an acrylic binder and the transferability to suspensions is not clear.

Concerning the LIF technique, to the author's knowledge, only CCD cameras have been applied. These cameras offer a better sensibility than CMOS (Complementary metal oxidesemiconductor) cameras, but can be used only for measurements with lower temporal resolution. For this reason, the effect of the lower camera sensitivity on the measurement accuracy needs to be examined.

The LIF measurement technique can be improved when two spectral bands are applied. In the majority of the applications found in the literature, a continuous laser (argon-ion laser) is used for illumination. However, a continuous illumination

Author and year	Application	T : **temperature** v : **velocity** pH: **pH value** C: **concentration**	Dye and liquid	Laser	Field of view
1C LIF					
Sakakiabara 93 [123]	Flow in cylindrical tube	2D, T and v	Water, Rh B	Ar-ion (cw, 488 nm)	40x30 mm^2
Lemoine 96 [80]	Turbulent free jet	0D, C	Water, Rh B	Ar-ion (cw, 514.5 nm)	-
Sakakiabara 97 [124]	Jet impinging on horizontal plate	2D, T and v	Water, Rh B	Ar-ion (cw, 488 nm)	20x20 mm^2
Karasso 97 [59]	General investigation	2D, pH	5(6)carboxydichloro-fluorescein	Nd:Yag (pulsed, 532 nm)	N.a.
Coolen 99 [24]	Free convection in cuboidal facility, measurement accuracy	2D, T	Water, Rh B	Nd:Yag (pulsed, 532 nm)	20x25 mm^2
Seuntienes 01 [128]	Wake behind heated cylinder	2D, T	Water, Rh B	Nd:Yag (pulsed, 532 nm)	55x55 mm^2
Ross 01 [119]	Temperature distribution in micro mixer	2D, T	Water, Rh B	Mercury arc lamp (cont., 500 - 550 nm)	ca. 200 x 400 µm^2
Meyer 02 [91]	Natural convection over heated plate	2D, T and v	Water, Rh B	Nd:Yag (pulsed, 532 nm)	200x160 mm^2
Yoon 05 [150]	Micro mixing, investigations of different dyes	2D, C	Water, ethanol, methanol, Nile Blue A	Diode (cw, 638 nm)	350x320 µm^2
Ichiyanagi 07 [56]	Micro mixing, confocal microscopy	2D, pH and v	Fluorescein sodium salt, water	Ar-ion (cw, 514.5 nm)	55x55 mm^2
Hoffmann 07 [53]	Micro mixing, confocal microscopy	3D, C and v	Water, Rh B	HeNe (cw, 543 nm)	400x550 mm^2

Table 2.6: Overview of works where one color LIF measurement technique is applied

Author and year	Application	T : temperature v : velocity pH: pH value C: concentration	Dye and liquid	Laser	Field of view
2C2D LIF					
Copetta 98 [25]	T: free convection, pH: turbulent jet, overview of dyes	2D, T and pH	Water, Rh B, fluorescine	Ar-ion (cw, 514.5 nm)	N.a.
Sakakiabara 99 [121]	Rayleigh-Bénard convection	3D, T	Water, Rh B, Rh 110	Ar-ion (cw, 488 nm)	$30x30x40$ mm^3
Kim 01, 03 [61, 62]	Free convection in mini channel	2D, T	Water, Rh B, Rh 110	Ar-ion (cw, 488 nm)	$1x1$ mm^2
Funantani 04 [39]	Free jet	2D, T and v	Water, Rh B, Rh 110	Ar-ion (cw, 488 nm)	$85x64$ mm^2
Sakakiabara 04 [122]	Rayleigh-Bénard convection, accuracy enhancement	3D, T	Water, Rh B, Rh 110	Ar-ion (cw, 488 nm)	$160x120x40$ mm^3
Kuhn 08 [70]	Flow over wavy walls	2D, T	Water, Rh B, Rh 110	Nd:Yag (pulsed, 532 nm)	$75x90$ mm^2
Natrajan 08 [94]	Mini channel, overview of dyes	2D, T and pH	Ethanol, Rh B, SulfoRh 101	Nd:Yag (pulsed, 532 nm)	$2.2x2.2$ mm^2
2C1D LIF					
Lavieille 01 [75]	Evaporating and combusting droplets	0D, T	Ethanol, Rh B	Ar-ion (cw, 514.5 nm)	-
Castanet 03 [19]	Evaporating and combusting droplets	0D, T	Ethanol, Rh B	Ar-ion (cw, 514.5 nm)	-
Bruchhausen 05 [17]	Heated turbulent free jet	2D, T	Water, Rh B	Nd:Yag (pulsed, 532 nm)	$25x50$ mm^2
3C1D LIF					
Lavieille 04 [74]	Heated free jet	0D, T	Ethanol, Rh B	Ar-ion (cw, 514.5 nm)	-
Maqua 06 [88]	Evaporating and combusting binary droplets	0D, T	Ethanol, acetone, Rh B	Ar-ion (cw, 514.5 nm)	-

Table 2.7: Overview of works where multi color LIF measurement technique is applied

is not useful for measurements with high temporal resolution and can lead to unwanted effects like photobleaching.

On this account, the measurement technique LCT is investigated in detail. The main error sources are highlighted and discussed and possibilities to minimize these effects are presented. Different kinds of data processing are investigated with regard to increase the measurement signal quality. To verify the applicability for measurements with high temporal resolution, the thermal response characteristic of encapsulated TLCs is examined. Further, volume instead of light sheet illumination is applied which necessitates real particle image thermometry analysis. It is ascertained that volume illumination is applicable for real 2D temperature measurements, and example measurements of a flow in a mini channel are presented.

The LIF measurement technique is applied as a promising alternative to LCT concerning its applicability for measurements with high resolution. Therefore a pulsed Nd:YAG instead of a continuous argon-ion laser and CMOS cameras are applied. This again demands other dye constellations because of the different exciting wavelength. Therefore, comprehensive spectroscopic investigations on different dyes are conducted in several liquids to find the most suitable dyes. Based on the results of the spectral investigations, 2C2D and 2C1D-LIF methods are tested and verified.

As a final result, a comparison between the LCT and LIF measurement techniques is done to help the user finding the proper measurement technique for the particular application.

Part I

Liquid Crystal Thermography

Chapter 3

Experimental Method

In this chapter, the technical aspect of 2D temperature measurements in liquids using LCT is described. The experimental method consists of the optical setup (3.1), the calibration procedure (3.2) and the image analysis (3.3). Because the possibility of measuring velocity fields with PIV simultaneously is an important feature, the chapter is extended with a brief explanation of PIV (3.4).

3.1 Optical Setup

The required optical equipment consists of a white light source to illuminate the TLCs and a camera to collect their reflected light. When high spatial resolution is demanded, optics with high magnification are required. Nevertheless, the optical equipment has to be set up carefully because it has a significant influence on the measurement signal quality.

3.1.1 Illumination

Light is generated when excited electrons of an atom move back to their ground state. Some electrons then emit photons which have a frequency in the visible range. Generally it can be divided between thermal and luminescence light sources. As for thermal light sources, the electrons are excited by thermal energy. Every body emits electro-magnetic radiation, the wavelength of which depends on the body's temperature. Wien's displacement law says that with increasing temperature, the radiation gains energy which means that the frequency increases and thus the wavelength decreases. Therefore, at a certain body temperature, the radiation becomes visible. Thermal light sources suit for LCT because of their continuous spectrum and their small part of UV radiation. The disadvantage of thermal light source is the low efficiency: only 10 % of the energy is converted into visible light, while the rest is infrared radiation. Typical substitutes are incandescent bulbs like tungsten bulbs, which spiral wound element is made of tungsten and has a high melting point above 3000 °C. When the electrons are not excited by thermal energy but by other processes, the light sources are called luminescence light sources. The possibilities of excitation are far reaching; electrical energy, UV-radiation, electron bombardment are some examples. Some luminescence light sources, for example gas discharge light sources, have higher efficiencies than thermal light sources. Disadvantageous for LCT measurements is the discontinuous spectrum of these light sources, which consists of peaks and bands depending on the used gas and metal coatings. Recently white LEDs (light emitting diodes) were applied by [32]. LEDs show a big potential, because they have a very high efficiency, high durability and are easy to control, so that pulsed illumination becomes easily possible. The constraint is, that LEDs nowadays provide relatively low light density and the spectrum of the white light LEDs is not continuous. Nevertheless, due to the effort put in the research for the development of LEDs, these constraints might be overcome soon.

When applying a light source for LCT, some facts have to be considered. TLCs get harmed by UV-light while IR-light leads to unwanted heat input. This becomes very important when using gas discharge lamps because they have an intensive spectral part in the UV region. Another unwanted effect is the heat input due to photon absorption when using continuous light sources. This becomes significant when intense light sources are necessary for high resolution measurements. The liquid and the walls absorb photons and the energy is dissipated and transformed into heat. To reduce scattering from the background, the facility walls should be either transparent or black, which again implicates good absorption properties. A possibility for reducing the unwanted heat input is to keep the duration of illumination as short as possible. This can be realized by light flashes or pulsed illumination. Light flashes have the disadvantage of being limited in their repetition rate ($\approx 50 - 60\,\mathrm{Hz}$). Pulsed illumination can be created by LEDs or by chopping a continuous light source with a polarizer or a chopper wheel, for example.

In the present work, tungsten halogen lamps were employed. When measurements with high spatial and temporal resolution were conducted, two tungsten halogen lamps were used with 250 W each. The light is transported to the measurement section by means of fiber optics. Because the used fiber optics are not transparent for IR radiation, an additional IR filter is not necessary.

Heat Input

The extensive effort of chopping the light was not expended because for most applications the heat input was not relevant. Further, the experimental setup for investigating hysteresis effects and the influence of aging and angle between illumination and camera axes did not necessitate a high measurement frequency. The illumination was not chosen too intense and thus, the occurring heat input leads to an insignificant increase of the absolute temperature of the liquid. For the observations, only the absolute liquid temperature was important, which was quantitatively measured by thermocouples. The two necessary light sources for the high speed visualization of the thermal response time caused significant heat input. With a simple modification, the heat input caused by illumination was measured and considered in the analytical calculation. For the convection cube setup, the heat input was negligible because a light sheet was created, which had a comparatively low light density.

3.1.2 Image Capturing

Compared to monochrome cameras, color cameras record the three basic colors red, green and blue separately. In most cases, this is realized by three sensor chips - one for each color - or one sensor chip and color filters in front of each pixel, called Bayer-matrix. For more informations see [58]. It is obvious that cameras with three chips show higher sensitivity than cameras with only one chip. In digital cameras, normally two kinds of image sensors can be found: CCD and CMOS. When photons hit the image sensor, electrons are released from the silicon atoms of its silicon layer. These electrons are either captured continuously (CMOS principle) or gathered for a certain time interval (CCD principle). As a result, the mini voltage of each sensor is captured and transformed into intensity values by digitalization.

With a sensor array of many sensors, 2D intensity fields can be measured. Nowadays, cameras have chips with $8 \cdot 10^6$ sensors. CCD cameras have better image capturing qualities, while CMOS cameras allow faster data transfer. The poorer image quality of the CMOS chips is caused by the inhomogeneous sensitivity of the particular sensors [58]. Nevertheless, the trend is going to an enhancement of the CMOS chip sensitivity, so that CMOS chips are nowadays available with a quantum efficiency of 40 %. This development makes CMOS cameras more and more attractive for high speed visualization.

In the present work, a CMOS high speed RGB camera[1] was used for measurements with high frequencies. When high measurement frequencies are not required, a CCD RGB camera[2] is preferred because of its better image capturing quality and higher quantum efficiency. High spatial resolution requires optical magnification. Therefore a long distance objective[3] was employed. Depending on the object lens, the working distance is 90 mm, respectively 45 mm. The numerical aperture is according to the manufacturer between 0.017 and 0.224 depending on the magnification and the objective which was used.

3.2 Calibration procedure

Generally, the connection between hue value and temperature is established with the calibration procedure. Therefore, the colors of the TLCs, respectively the hue values at a certain temperature are measured with a RGB camera, and the result is a calibration curve as shown in figure 3.1. After approximating a polynomial, the temperature can be calculated from the measured hue value.

This quite simple principle is rather complex in reality and several things have to be considered. In this section, the most important factors are described. The calibration has to be conducted in-situ, which means under measurement conditions. It has to be taken into account that reflections of the background interfere with the reflected light of the TLCs. Ideally, the background should not have any reflective surfaces, which can be realized with transparent or blackened non-transparent walls. Nevertheless, few reflections remain which influence the

---

[1] IDT X-Stream XS-3, 614 fps at full resolution (1280 x 1024 pixels)

[2] Hitachi HV-C20 M, Resolution: 752 x 596 pixels

[3] Leica Z16, objective: 1.0x or 2.0x, camera tube: 1.0x

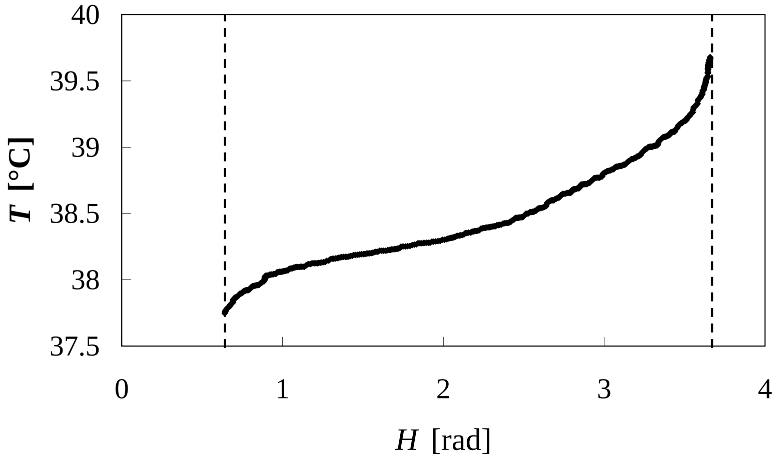

Figure 3.1: Calibration curve. From the measured hue values, the temperatures can be calculated (e.g. with a fifth order polynomial)

measurement signal. The angle between the illumination and optical axis, the light intensity, the field of view and the camera configurations must not change after the calibration procedure because these factors have a significant influence on the temperature-hue-allocation. Generally, there are two different methods of calibration for TLCs in liquids.

One principle is the linear temperature distribution within the area of interest, achieved by a stratified temperature distribution of the liquid. This is achieved when the top wall has a higher temperature than the bottom wall, while the remaining walls are adiabatic. With the known wall temperatures, the temperature depending on the distance to the isothermal walls can be linearly interpolated. The advantage is that principally one image suffices for the whole calibration. The disadvantage is on the one hand that the experimental setup must offer the possibility of tempered walls at the top and bottom. Further, image processing procedures like local calibration (see chapter 4.5.1) are not possible.

The other calibration method is the sequential approach of homogeneous temperature distributions. The system is heated up and kept on the particular temperature, until a sufficiently homogeneous temperature distribution is achieved. Of course, it is not possible to reach entire isothermal conditions, since the walls are not adiabatic, and even if they were, the duration to reach homogeneous temperature distributions is infinite. Nevertheless, this possibility provides the best calibration results, but it is very time consuming. The greater the liquid volume is, the longer it takes until a homogeneous temperature distribution is achieved. This circumstance should be considered when designing the measurement facility.

For the present measurements, the calibration procedure was conducted before the measurement sessions. Therefore, the optical setup (illumination, focal plane) was adjusted and fixed. In most measurements, the calibration process was sequential calibration with a continuous increasing temperature of around 10^{-3}K/s. The start and end temperatures were chosen beneath and beyond the TLCs red start and blue stop temperatures. The reference temperature was measured with thermocouples[4]. Depending on the measurement setup, the thermocouples were either directly allocated in the liquid (section 4.3) or soldered within the facility walls (section 4.6). The measured voltages are captured[5] and digitized[6]. Temperatures are computed from the voltages and visualized on the computer screen with a data acquisition program[7]. A further feature of the equipment is the possibility to send 5 V trigger signals. With this instance the calibration procedure is automated. The liquid is heated up slowly and at a certain temperature interval, a trigger signal is sent to the RGB camera[8], which captures a certain amount of images. The signal flow is illustrated in figure 3.2.

3.3 Image Analysis

The type of image processing for PIT depends on the spatial resolution. If the spatial resolution is low and the image diameter of an encapsulated TLC is less than one pixel, the image processing simplifies. The hue information is received from each pixel. Beside the RGB to HSI transformation, only a few standard image processing algorithms need to be applied like background subtraction, high frequency noise removal with long pass filters and, if necessary, local calibration. This leads to a higher accuracy in the temperature measurement because a higher amount of encapsulated TLC particles per imaged area contribute to the temperature measurements. For the velocity measurement, this fact is disadvantageous because the signal to noise ratio suffers. In terms of a high spatial resolution and a

---

[4] Electronic Sensor, 0.5 mm thermocouple, type K

[5] National Instruments, SCXI 1102

[6] National Instruments, PCI-NI6221

[7] National Instruments, Labview 7.1

[8] IDT X-Stream XS-3

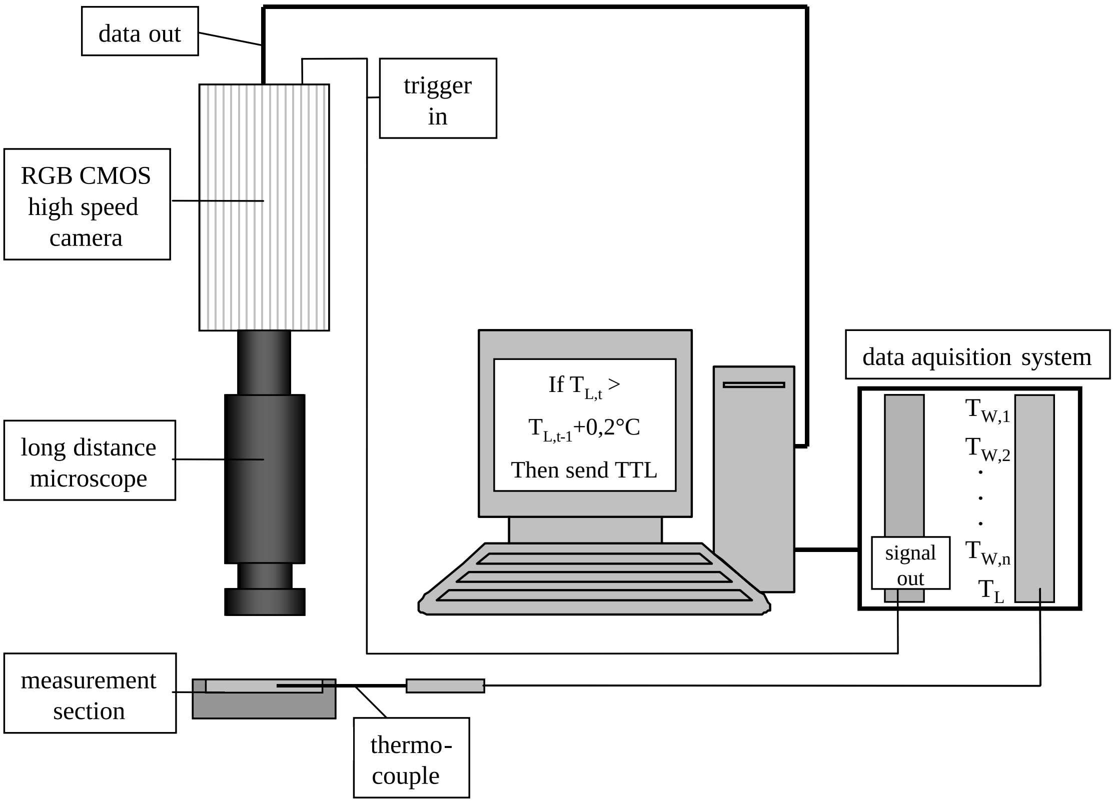

Figure 3.2: Schematic illustration of the signal flow for automated calibration procedures

high measurement accuracy, the optimum image diameter of one particle for PIV measurements is $2 - 3$ pixels [113].

If the spatial resolution is high, particle detection becomes necessary. On the one hand, the TLC capsules have an image diameter up to 10 pixels, and therefore, the temperature information is extracted from the TLC capsule itself. On the other hand, when volume illumination is applied, the whole measurement volume is illuminated, and only the encapsulated TLCs within the measurement volume shall contribute to the planar temperature measurement. It is obvious that particles before and behind the measurement volume produce wrong temperature information. Due to fewer TLC capsules per imaged area, the accuracy is lower.

In this section, some typical processing procedures are explained and their influence on the measurement accuracy is described. Image processing is divided into pre-processing, processing and post-processing. Pre-processing is used as preparation of the images. Typical pre-processing procedures are background subtraction or defining the area of interest. The actual RGB to HSI transformation or operations like particle detection are processing procedures. Post-processing algorithms are applied to sort obviously wrong values out of the temperature fields. Arithmetical averaging, mean or long pass filters are often used for post-processing.

3.3.1 Pre-processing

It has been found, that background subtraction is a very useful pre-processing algorithm which significantly enhances the quality of the results. Thus, reflections of the background, which have an erroneous contribution to the measurement accuracy, are minimized. The background image is taken at the beginning of the calibration procedure, when the TLCs are out of the activity range and appear milky. It is self evident that the optical configuration must not change when capturing the background image. To achieve a smooth hue distribution, it is recommended to capture a sequence of background images and to apply temporal and spatial averaging. The background image is then subtracted from the measurement respectively calibration image before the RGB to HSI transformation. The effect of the background subtraction and the resulting measurement signal enhancement are presented and discussed in section 4.5.2.

Further pre-processing algorithms are the removal of erroneous hue values, which might occur due to erroneous pixel sensors. This can be done by minimum and maximum thresholds or median filters. To remove high frequency noise, long pass filtering can be applied. In doing so, it is averaged over a certain pixel array.

In the present work, pre-processing has been applied in the following way. First, the background was subtracted, then the area of interest was cropped and a long-pass filter was applied.

3.3.2 Processing and Particle Detection

The actual processing is the conversion of the hue values into the temperatures. This is done by means of the calibration curve and the RGB to HSI transformations from equation 2.2. Beside the standard procedure of using one calibration curve for the whole measurement volume, spatially dependent calibration curves can also be applied. This means that the area of interest is divided into interrogation areas and every interrogation area has its own calibration function. The procedure and the effect of local calibration is described in detail in section 4.5.

When applying true particle image thermometry, the temperature information is provided by the particles exclusively and not from the background. To extract the temperature information from the particles, the particles need to be detected first. Generally there are different methods for particle detection [95, 152]. If the signal to noise ratio is in an acceptable range, the common, and simplest particle detection method namely threshold filtering can be applied.

In this section, the algorithms for particle detection are described like it was conducted for the high resolution temperature measurements in the present work. First the background is subtracted and a threshold is set, which emerges from the maximum and the mean image intensities. After the threshold filtering, areas remain, which show intensities bigger than the threshold. Within each of these areas, the coordinates of the maximum intensity are determined. As a result, the centers of the particles are obtained. Beside the particle positions, the particle diameters were determined. This has been done to figure out if there are connections between the indicated temperatures and the particle diameter. In addition to that, the particle diameter information can also be used to separate putative TLC capsules or TLC agglomerations. The particle diameter determination method, which is presented below, is quite simple but not very accurate. For particle diameter determinations with higher accuracy see [98, 1, 60]. Nevertheless, for the above mentioned purpose, the particle diameter determination method is absolutely adequate.

Before the algorithms for the particle diameter determination can be applied, the exact particle position must be known. Therefore the subpixel position of the particle is calculated which defines the particle center with a higher resolution than the pixel resolution. Because the particle intensity distribution is Gaussian-like [1], the subpixel determination of the center can be determined as explained exemplary for the x-direction. First the natural logarithm is calculated from the intensity values of the center pixel x_0 and the two adjacent pixels x_{0-1}, x_{0+1} with $J_x = \ln(I_x)$. The subpixel accuracy δx is then calculated from

$$\delta x = \frac{J_{x_{0-1}} - J_{x_{0+1}}}{2(J_{x_{0-1}} + J_{x_{0+1}} - 2J_{x0})} \tag{3.1}$$

and the exact position of the center is $x_0 + \delta x$, respectively $y_0 + \delta y$. Another method is the approximation of a quadratic polynomial through the natural logarithm values. Here the center and the two or more neighboring pixel values can be comprised.

The pixel diameter of the particles, $d_{P,pix}$, is determined by a one-dimensional Gaussian fit in x- and y-direction iteratively by

$$I(x) = (I_{max} - I_0) \cdot \exp\left(-8\left(\frac{x-(x_0+\delta x)}{d_{P,pix}}\right)^2\right), \tag{3.2}$$

whereas I_{max} and I_0 are the intensities of the particle center and the environment and x_0 the x-position of the particle center. The particle image diameter, $d_{P,I}$, is calculated from the pixel size, s_{pix}, and the particle diameter in pixel with

$$d_{P,I} = d_{P,pix} \cdot s_{pix}. \tag{3.3}$$

The actual particle diameter, d_P, is then calculated from the image diameter, $d_{P,I}$, with regards to refraction effects from

$$d_P = \frac{1}{M}\sqrt{d_{P,I}^2 - \left(2.44 \cdot (M+1)\frac{\lambda}{2NA}\right)^2}, \tag{3.4}$$

where M represents the magnification, NA the numerical aperture and λ the wavelength of the illuminating light. For white light, a mean wavelength of $\lambda = 550\,nm$ can be assumed.

As a result, particle image data exists, which contains the exact coordinates of the particle, the particle intensity, the hue value averaged over the particle image area and the particle diameter.

3.3.3 Post-Processing

As mentioned before, the hue signal of the TLCs is not very stable; the signals show a high deviation from the mean hue signal. Principally different methods exist to reduce the image noise. The non-linear median filter is very useful to remove erroneous values which show extreme divergences. Because these extreme divergences significantly affect linear low pass filters, the median filter is recommended to be applied beforehand. The low pass filters then reduce high frequency noise. Further it can be divided between temporal and spatial filtering. Several images are required when applying temporal filtering techniques. Of course the flow phenomena has to be steady within the time period for filtering. Further, it should be taken into account that filtering always leads to a reduction of the resolution. A careful choice of the spatial and temporal kind and size of filters is essential. The effect of filtering methods on the measurement accuracy is shown in chapter 4.5.3.

3.4 Simultaneous Measurement of Temperature and Velocity Fields

The most significant advantage of applying encapsulated TLCs for temperature measurements in liquids is the possibility to determine velocity fields by means of PIV simultaneously. In this section, the common PIV technique is described very briefly, since much literature exists on this topic [1, 113, 90, 125]. The principle of PIV is the measurement of the particle displacement. Therefore, the flow is seeded with particles (here encapsulated TLCs) and a pair of images is captured at specific times t_A and t_B. The images are divided into interrogation areas and the interrogation areas of image A are correlated with the corresponding interrogation areas of image B. Each correlation leads to a correlation matrix which again gives information about the pixel displacement of the particles. After applying algorithms to achieve particle displacement with sub pixel accuracy (see also equation 3.1), every interrogation area exhibits a pixel displacement in x- and y-direction, d_x and d_y. The according velocities are calculated with

$$v_i = \frac{d_i \cdot s_P}{t_B - t_A} \tag{3.5}$$

with the pixel size s_P.

To employ PIV, some requirements need to be fulfilled; as already mentioned, the particles must have a certain image diameter ($2-3$ pixels) [113], the displacement of one particle from image A to image B should not exceed half of the interrogation window size, and the particle seeding density should be that high, that $3-4$ particles can be found within an interrogation window.

Figure 3.3 illustrates the flow chart of the image processing procedure, which is required to simultaneously apply PIT and PIV. The RGB images are transformed into HSI images and the intensity images are pre-processed by employing background subtraction, long pass filtering and, if necessary, other pre-processing algorithms. Now the PIV algorithms can be applied and the obtained vector fields are post-processed to eliminate erroneous velocity vectors.

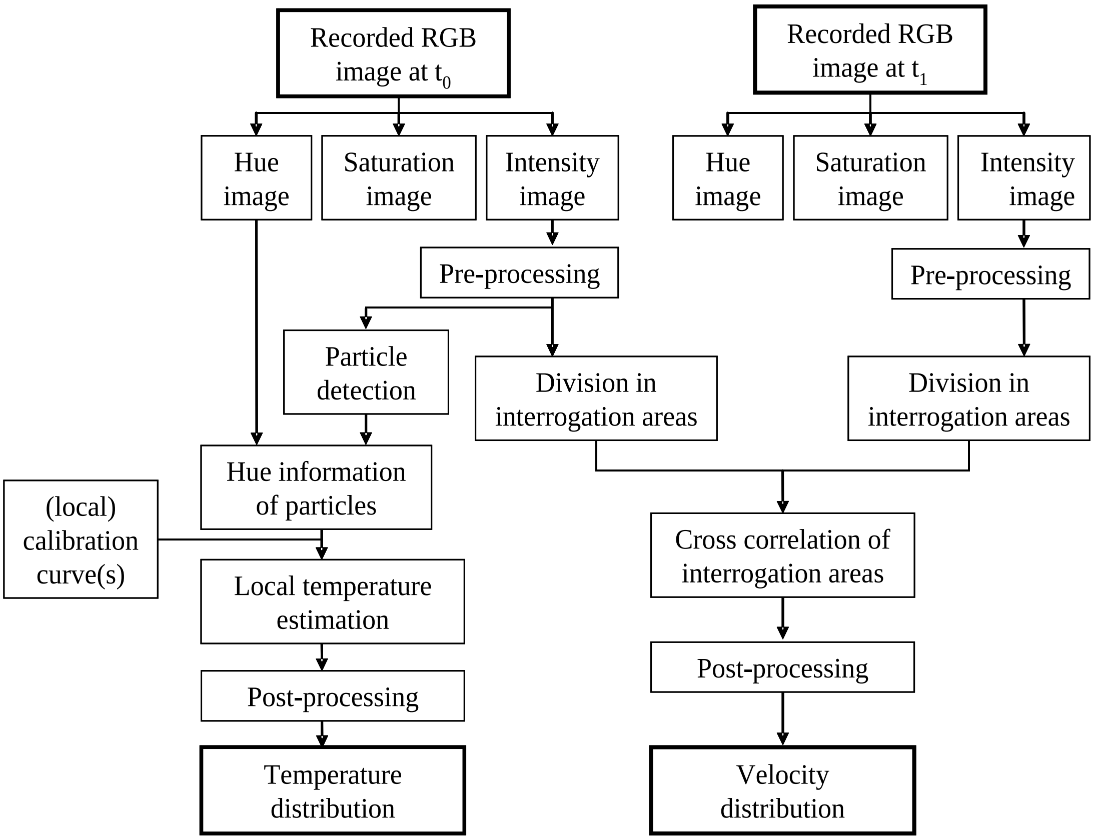

Figure 3.3: Principle of simultaneous measurement of temperature and velocity fields

Chapter 4

Experimental Characterization and Deployment

The first part of the following chapter deals with the accuracy of the measurement technique LCT. Therefore, reasons for uncertainties in the measurement technique are pointed out (4.1) and the effects of super-heating (4.2), illumination and camera configuration on the signal quality (4.3) are presented. To figure out the constraints of the measurement technique regarding its temporal resolution, investigations on the thermal response characteristic are presented in 4.4. Beside the experimental configurations, methods of signal processing exist, which can be applied to enhance the measurement accuracy and are presented in 4.5.

At the end of the chapter, the TLCs are employed in simultaneous temperature and velocity field measurements. The measured temperature fields in a thermal induced free convection (4.6) are compared with numerically calculated ones. To conclude, the measured temperature fields in a channel flow are presented (4.7). In this context, the volume illumination method was applied and further, 3D temperature fields were achieved by scanning the flow. The measurements were performed with high spatial and temporal resolution.

4.1 Measurement Accuracy and Error Sources

Generally the quality of temperature measurements with TLCs is expressed by high signal resolution dH/dT and low measurement uncertainty σ_T. In figure 4.1, a temperature hue calibration curve is shown. The temperature error bars

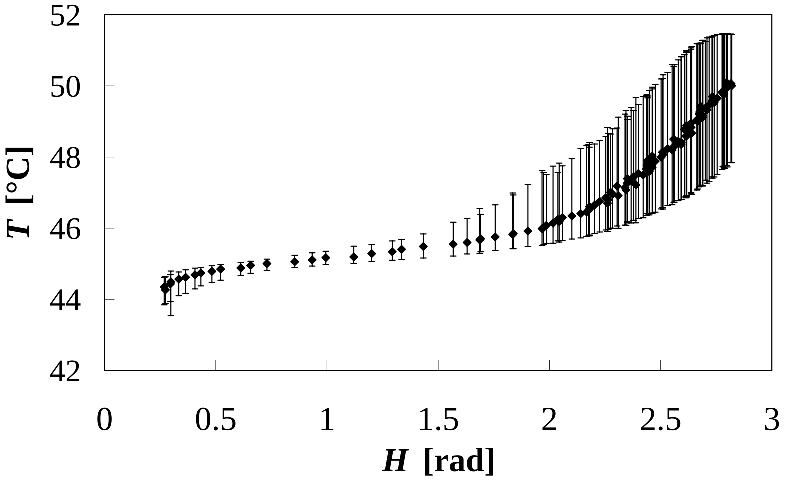

Figure 4.1: Temperature hue curve from calibration, TLCs BM/R40C10W were used

were calculated from the deviations of the hue values at almost homogeneous temperature distribution with

$$\sigma_T = \sqrt{\frac{1}{n-1}\sum_{i=1}^{n}(T_i - \bar{T})^2}. \tag{4.1}$$

In equation 4.1, T_i is the temperature indicated by the TLC capsule, $\bar{T}$ the mean temperature and n the number of measured temperature values. At a definite temperature, the encapsulated TLCs do not show a certain hue value but a spectrum of hue values. The dots in figure 4.1 represent the measured temperature by the TLCs (calculated from the average hue value) at the particular temperature. From the average hue values, the calibration polynomial is calculated with fitting a polynomial (in this case of 9th order). The error bars represent the common standard deviation of 68.3 %. It can be seen that the measurement uncertainty increases in the upper temperature region while it is quite moderate in the lower region. Because it reaches up to 25 % in the upper temperature region, the measurement accuracy is quite disaffected here.

Many parameters exist which lead to erroneous temperature measurements with TLCs (figure 4.2) which are described as follows. The temperature field measurement error finally results from erroneous hue value measurements and errors in the calibration curve. It should be noted that it is not possible to quantify the particular errors. Compared to bias errors of thermocouples for example,

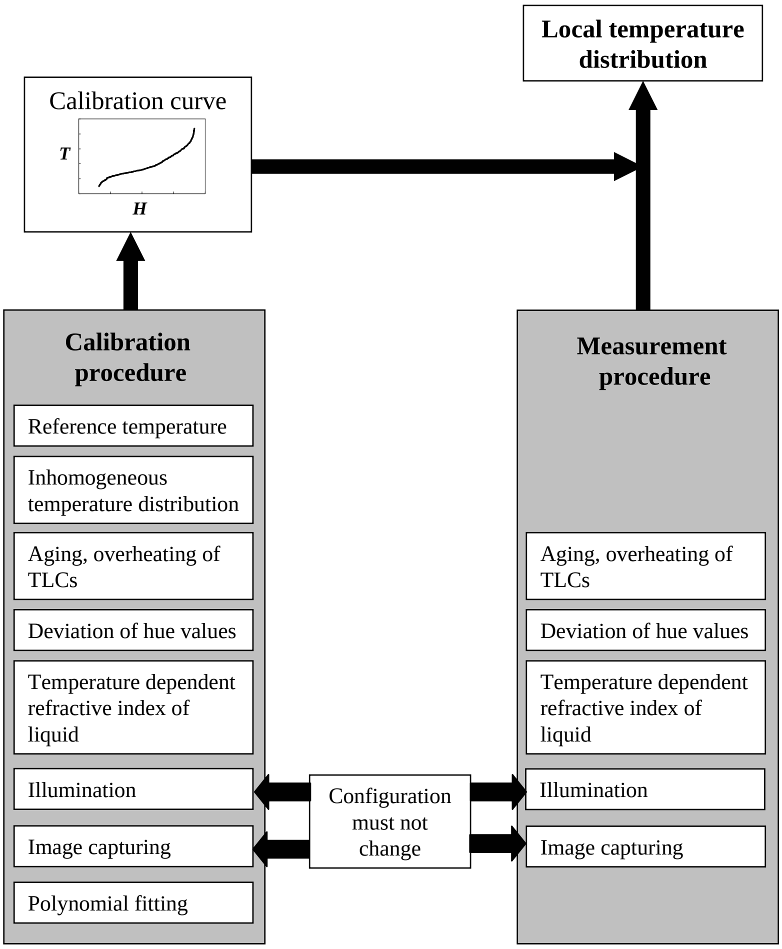

Figure 4.2: Error sources from calibration and measurement procedure affecting temperature measurement with TLCs

errors in optical measurements are, due to the huge number of error sources, nearly impossible to predict. It is up to the elaborateness of the measurement procedure to minimize these errors as much as possible. A possibility to quantify the sum of all errors is, for example, the measurement of homogeneous temperature distribution. Then the measured temperature field can be compared with the expected one. Of course, the expected temperature field also contains errors, due to reference temperature measurement with thermocouples, for example. In addition, it is not possible to reach absolutely homogeneous temperature distributions under experimental conditions.

Reference Temperature Measurement

As already mentioned, the reference temperature measurement is used in the calibration procedure. The overall error consists of the measurement error of the thermocouple, the mini voltage transmittance, its magnification and digitization. The error of the thermocouple comprises a systematic and a stochastic part. Therefore a correction polynomial, obtained from a thermocouple calibration procedure [27] can be applied to minimize the error from $\pm 1\,K$ to $\pm 0.1\,K$ absolute.

Inhomogeneous Temperature Distribution of the Liquid Volume

To determine the hue value-temperature allocation, careful calibration procedures have to be accomplished. This automatically implies a homogeneous temperature distribution which is furthermore very important for the local calibration polynomial (see 4.5.1). To achieve proper homogeneous temperature distributions in the liquid volume, tempered walls are essential. This can be realized by applying secondary tempering flows which temperatures are controlled by a thermostat. The heat is conducted through a solid block so that small temperature changes in the liquid flow are dampened by the heat capacity of the solid. Further, the remaining walls which define the liquid volume should be isolated to achieve nearly adiabatic conditions. But even then the temperature is not homogeneous. The heat transport through the walls is not zero and when the wall temperature is changed, it takes a long time until the temperature distribution is homogeneous. These effects have to be taken into account when designing the experimental procedure.

Aging/Super-heating of TLCs

It has been observed that TLCs, which are in use for several hours, change their reflective properties which leads to substantial measurement errors. Besides that, TLCs must not be heated far above their activity range, because hysteresis occurs in their temperature hue curve. In such a case, TLCs should be cooled beyond the red start temperature. Investigations on these phenomena are presented and discussed in 4.2. When the temperature is too high, TLCs can also be destroyed.

Deviation of Hue Values

The greatest error source is the deviation of the reflected colors of TLC capsules at homogeneous temperature conditions. This effect is among other things addressed to the encapsulation process [100, 69, 142] and it is assumed that shear stresses occur while the capsules are hardened.

Further, the TLCs are made of a mixture of organic compounds and a different composition from particle to particle can be expected. Another reason for the deviation of the hue values is the capsule itself. As it is spherical, it behaves like a lens with aberrations.

Compared to bias errors due to illumination or background reflection, this error is not predictable and therefore occurs in form of high frequency noise also called white noise. To demonstrate the high frequency noise, the hue values of single particles within a section of the area of interest are shown in figure 4.3. The section has a size of 420 *x* 32 pixels. Because the temperature distribution is almost homogeneous, the hue values should be in fact equal. Instead high frequency noise can be recognized but also components of noise with lower frequencies which is addressed to inhomogeneous illumination conditions. To minimize this error, local and/or temporal averaging needs to be done.

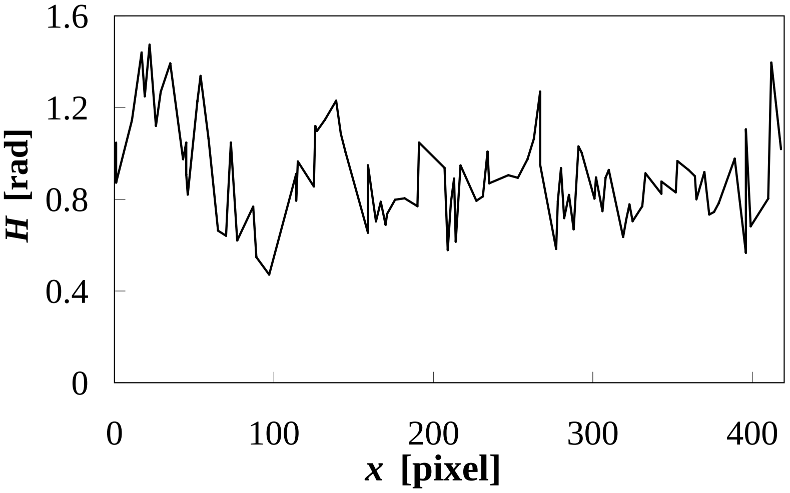

Figure 4.3: Hue values of TLC particles detected within a section of 420 *x* 32 pixels at homogeneous temperature

Due to the additional determination of the particle diameter (see section 3.3), it is possible to display the the hue values of the particles depending on their diameter (figure 4.4). It can be seen that there is no real correlation between the particle diameter and the reflected hue value. What can be seen in figure 4.4 is the increase of the deviation of hue values with increasing temperature. The reason for the temperature dependent measurement uncertainty is not known. Possible explanations are augmented misalignments in the molecule structure at higher temperatures or inhomogeneous twisting angles.

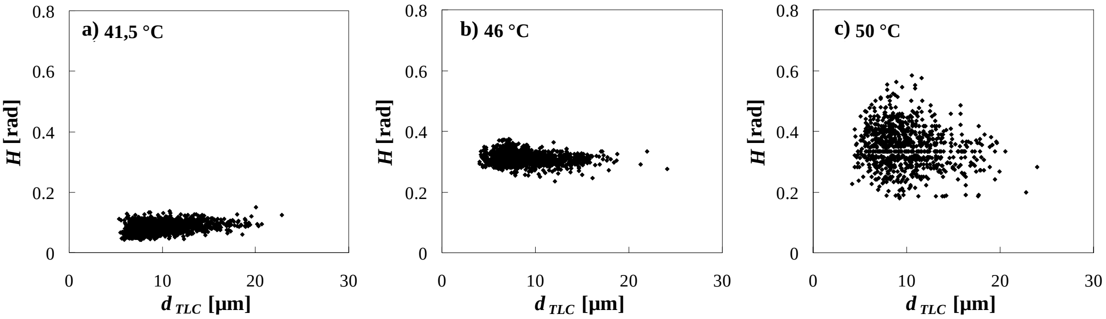

Figure 4.4: Hue value distribution over diameter of encapsulated TLCs (BM/RS40C10) at different temperatures

Refractive Index

All liquids exhibit a temperature dependent refractive index which normally increases with increasing density. Although the change of the refractive index at moderate temperature differences (20 K) is negligible, the refractive index is strongly dependent on the wavelength of the passing light. If the refractive index changes locally, the propagation of the light also changes which results in optical deformations. This effect especially leads to geometrical errors.

Illumination

When illuminating the measurement volume, unavoidable reflection and scattering effects occur. This leads to inhomogeneous illumination of the FOV (field of view) which again leads to low frequency noise of the hue values of the reflected light. This error is primarily of systematic nature, if the illumination is stable over time. Image processing procedures like local calibration or background subtraction can be applied to minimize this error. Nevertheless, one should be careful, when arranging the illumination of the test section. Another, more problematic error is the heat input caused by illumination which happens due to photon absorption of the liquid and most notably by blackened facility walls. This error becomes significant when intense illumination is applied. The additional heat input is hard to determine. While absorption coefficients can be estimated rather good, the light density is mostly not predictable. Nevertheless, the heat input into the channel walls can be determined by measuring it, which again requires intricate modifications of the setup like additional temperature measuring points. A possibility for minimizing the heat input is to keep the illumination duration as short as possible. This can be realized by a pulsed illumination like a flash lamp.

Image Capturing

The field of different measurement errors caused by image capturing is extremely far-reaching and therefore only error sources which have a significant influence are mentioned. Cameras show variance in the intensity image itself, which is caused by photon noise. Spatial inhomogeneities are caused by different dark signals and different sensitivities of the sensor elements [58]. Generally CCD cameras show less dark noise and are preferable for measurements of low light intensity. A factor which also influences the measurement accuracy is the digitization of the intensity. When using an 8 *bit* system e.g., the expression of the intensities is limited to integer values from $0 - 255$. This directly leads to a limitation of the resolution and therefore in measurement accuracy. For a list of further error sources see [58].

Polynomial Fitting

Commonly, the temperature hue curve can not be described by typical standard functions like linear, logarithmic, potential or exponential functions. Therefore, a polynomial with a high order has to be approximated. The approximation is erroneous and the uncertainty of the hue temperature calibration can be calculated from

$$\delta T = \left(\left(\frac{dT}{dH} \delta H \right)^2 + (2 \cdot SEE)^2 \right)^{\frac{1}{2}} \tag{4.2}$$

where $\frac{dT}{dH}$ is the slope of the curve fit and SEE is the standard estimate of error. This can be calculated from

$$SEE = \frac{\sum_{i=1}^{k} \left(T_i(H) - T_{fit,i}(H)\right)^2}{k - j - i} \tag{4.3}$$

with the number of data points is k and the order of the polynomial is j [47].

Test Liquid

The liquid, in which TLCs are suspended has a further influence on the calibration curve. When suspending TLCs in glycerin, the hue-temperature curve is shifted to higher activation temperatures compared to water [42]. It is supposed that the different refractive indices of the liquids are responsible for the shift. This effect should be taken into account when the measurement setup is developed.

4.2 Super-heating and Aging of TLCs

When TLCs are heated beyond their activity range, hysteresis in the temperature-hue gradient occurs. Another reason for different hue gradients in heating and cooling processes are aging effects. Aging means that a change in the TLC properties occurs when keeping them at a certain temperature for a longer time period.

4.2.1 Experimental Procedure

Within the present work, the TLC behavior at super-heating and retaining on a certain temperature was investigated experimentally. Therefore a mini channel ($2\,x\,2\,x\,40$ mm), made of copper has been set up vertically (figure 4.5). The walls of the channel were blackened. The channel has been covered with a PMMA plate and a thermocouple for reference temperature measurement was mounted within the channel near the FOV. Nearly homogeneous temperatures of the copper block were achieved by means of a water flow running through a tube beneath the channel. For temperature control, a cooling thermostat was used which allowed defined temperature gradients over time. Thus sawtooth-shaped heating curves were realized. Water, glycerin and a 50% (Vol) mixture of water and glycerin were used as test liquids. Pure glycerin works best for long term measurement because

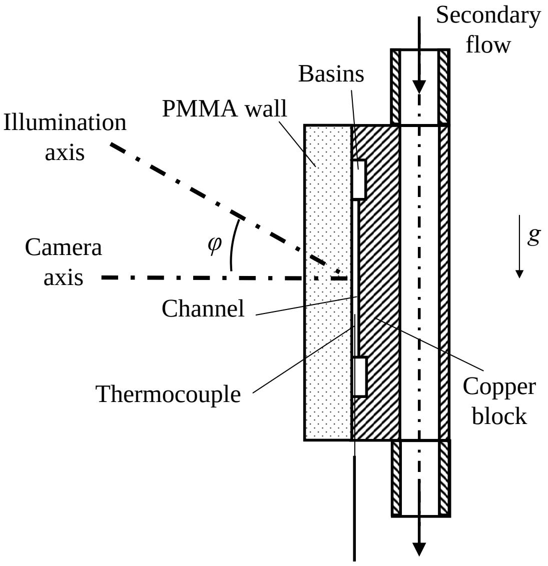

Figure 4.5: Sketch of measurement setup

the TLC capsules do not settle down. Although glycerin has a higher density than the TLC capsules, the buoyancy of the TLC capsules is marginal. The buoyancy is calculated with

$$u_s = \frac{d_P^2 \cdot g}{18\nu}\left(\frac{\rho_P}{\rho_L} - 1\right) \tag{4.4}$$

in which d_P and ρ_P are the particle diameter and density, ν and ρ_L the viscosity and the density of the liquid and g the gravitational acceleration. The particle moves in direction of gravitation when u_S is positive. For a particle diameter of $d_P = 10\,\mu\text{m}$, a mean particle density of $\rho_P = 1.1\,\text{g/ml}$ and the properties of glycerin at 45 °C of $\rho_{Gl} = 1.245\,\text{g/ml}$ and $\nu_{Gl} = 165 \cdot 10^{-6}\,\text{m}^2/\text{s}$, the velocity of buoyancy is $u_S = -3.85 \cdot 10^{-8}\,\text{m/s}$. An additional advantage of the high viscosity is the reduction of unwanted free convection.

The FOV was imaged with a long distance microscope objective[1] and captured with a high speed CMOS RGB camera[2]. The white light for illumination was generated by a halogen cold light source[3] and the light was guided to the FOV by an optical fiber[4]. In this configuration, the TLC particles have an image diameter

---

[1] Isco Optics GmbH, K2 Long Distance Microscope

[2] IDT, X-Stream XS-3

[3] KL 2500, Schott

[4] Fiber glass, $d_i = 12\,\text{mm}$

of $4-5$ pixels and the FOV contains the whole width of the channel and a part of the wall. The measurement frequency was 30 Hz which is at the same time the lowest possible measurement frequency of the highspeed CMOS RGB camera. Although the CMOS camera has a lower sensitivity than an available CCD camera, it has been chosen because it can be integrated into the system information flow as described in chapter 3.2. Hence, this allows automated calibration procedures which drastically alleviates the experimental procedure.

4.2.2 Results

Aging

To investigate the long-term behavior of TLCs, they were kept on a certain temperature for a longer period of time (approx. 1 h) and the hue values were measured. As shown in figure 4.6, an increase of the hue values over time was observed. On this account, several possible influence parameters were investigated.

The influence of the test liquid was investigated employing water, glycerin, water/glycerin (50 % vol) mixture. The volumetric seeding concentration of the TLCs[5] was for all liquids $5 \cdot 10^{-3}$. As can be recognized in figure 4.6, the hue value increases over time more or less independent on the test liquid. Further, it can be seen that TLCs in different liquids indicate different hue values at the same temperature of $43.5\,^{\circ}C$. Interesting is the similar behavior of glycerin and glycerin/water mixture. Some authors assume that the difference in the refraction index is the reason for different hue behavior in glycerin and water. Nevertheless, this appears unlikely since the glycerin water mixture behaves very similarly to pure glycerin.

As can be seen in figure 4.7, a sub-cooling of the TLCs below their start temperature does not soothe the effect. After the sub-cooling, the hue value increase over time continues as if there were no temperature change.

Another reason for the hue value increase might be found in the illumination and image capturing side. Either the color temperature of the illumination changes slightly over time or the image capturing shows a defective behavior and does not show stability in color capturing. Both of the above mentioned influences could be excluded quickly in examining the color change of the partly imaged channel wall.

---

[5] Hallcrest BM/R40C8W/S-40

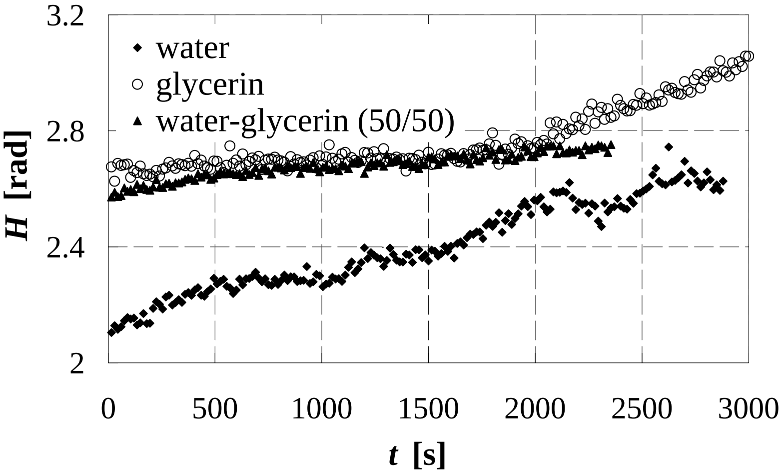

Figure 4.6: Hue gradients over time for different liquids at 43.5 °C

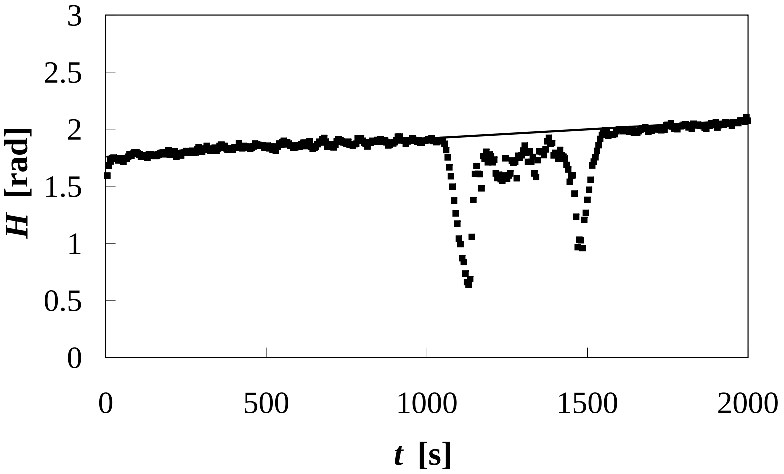

Figure 4.7: Hue gradient over time. Suspension was sub-cooled between 1000 and 1600 s to 38 °C. During sub-cooling interval, TLCs were out of activity range and no hue values were measurable

The color of the channel wall did not change in the least. Although it is rather unlikely, the bright illumination might have an influence on the hue-temperature behavior of the TLCs. This was examined in comparing long-term and short-term illumination which means that one TLC suspension was illuminated during the whole measurement duration while another TLC suspension was exclusively illuminated during the image capturing. Both hue values show a similar increase over time (figure 4.8) so that the influence of illumination can be excluded.

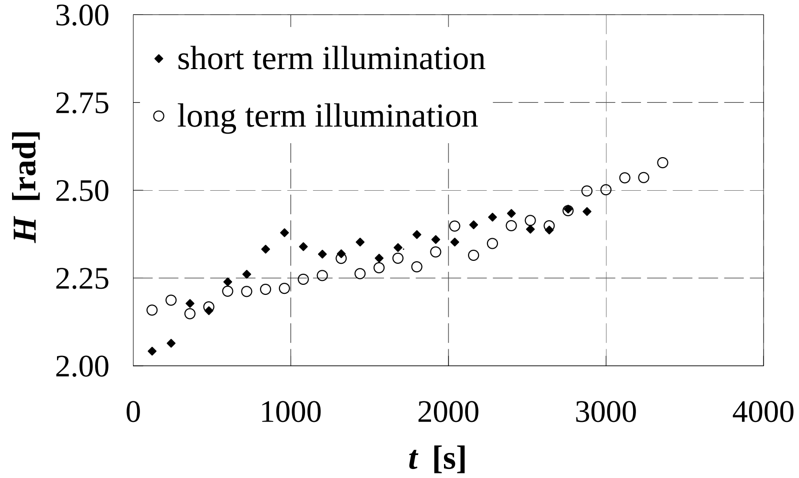

Figure 4.8: Comparison between short term illumination (illumination only lasts while capturing) and long term illumination (illumination is continuous) regarding the increase of hue values over time

This phenomenon of increasing hue values over time leads to additional errors in temperature measurement. One possibility for minimizing this error is to renew the suspension within the liquid volume of the facility. An assumption for the hue value increase over time is that glycerin affects the TLC capsules and the TLCs get damaged over time. This also appears unlikely since the water as test liquid also leads to an increase of the hue values although the test channel was cleaned carefully between the measurements. The damage of TLCs due to intense illumination can also be excluded as shown above. A more realistic assumption might be the influence of the paint which was used to blacken the channel walls. Although enough time passed for drying out, some volatile components of the paint might diffuse through the polymer shell and damage the TLCs.

Super-heating

A certain number of studies have attended to the super-heating effects of TLCs (e.g. [8, 120, 2, 51, 7]). Some authors are of the opinion that the degree of hysteresis depends on the degree of super-heating (e.g. [2]) while others see no connection (e.g. [7]). Baughn et al. [8] pointed out that hysteresis disappears when the TLCs are cooled beyond their red start temperature. Sabatino et al. [120], on the contrary, found a permanent damage of the TLCs.

Based on those discrepancies, investigations on hysteresis effects were carried out. Further volume illumination was employed to figure out if additional effects arouse. Figure 4.9 shows two hysteresis curves for different super-heating rates. For reasons of universal validity, the temperature is plotted dimensionless and is calculated from $\vartheta = \frac{T-T_{start}}{T_{stop}-T_{start}}$, where T_{start} and T_{stop} are the start and the stop temperatures of the activity range and T is the actual temperature.

While the hue curve appears normal during the heating process, unusual behavior can be found during the cooling process of the TLCs. Here they show a pendulous abdomen between $\vartheta = 1.2$ and $\vartheta = 1.4$. When being re-heated, the TLCs show the expected hue value gradient. This behavior is repeatable in the following heating and cooling processes and thus is called hysteresis. Comparing figure 4.9 top and bottom shows that the temperature-hue-gradients are fairly congruent with each other. A significant dependency of the pendulous abdomen characteristic on the degree of super-heating can not be seen. Further, it can be seen that the hue-temperature value is repeatable between $\vartheta = 0$ and $\vartheta = 0.8$, which means that the TLCs are still usable after super-heating in a restricted temperature range. Not shown in the present work is the effect of sub-cooling, which is cooling of the TLCs beyond their start temperature. It has been observed that sub-cooling leads to a reset in the hysteresis. This means that the TLCs, which are sub-cooled after super-heating, show normal temperature-hue gradients as if no super-heating took place.

An interesting issue is the behavior of the standard deviation of the hue values when the TLCs are super-heated (figure 4.10). The standard deviation,

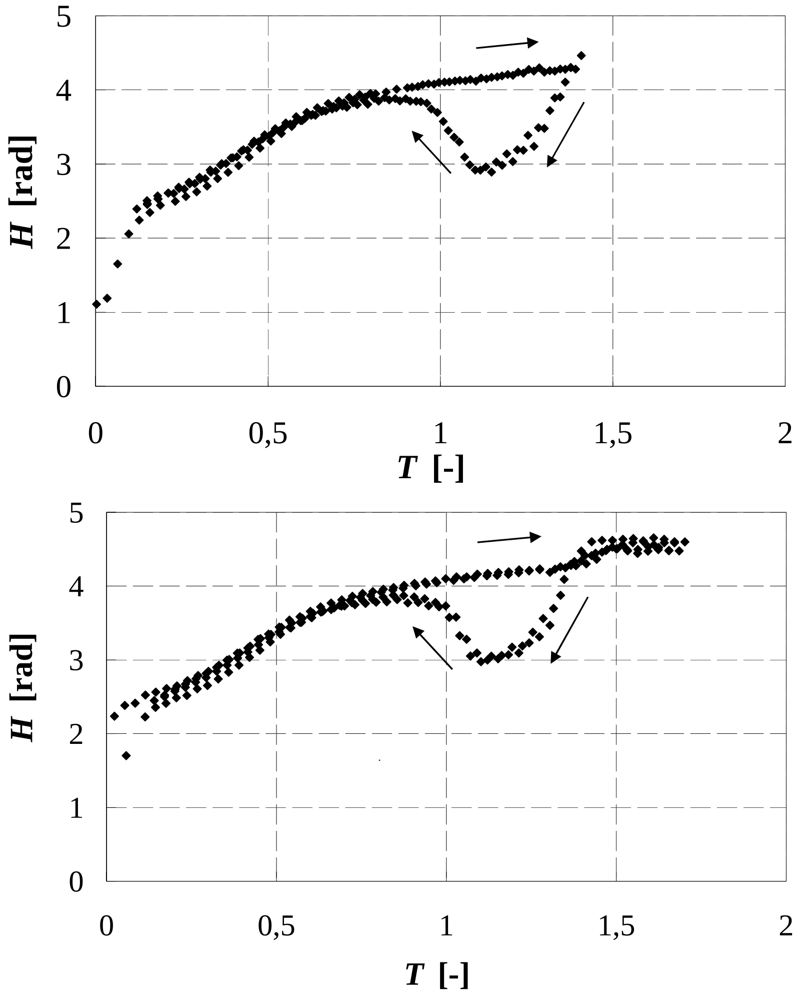

Figure 4.9: Hysteresis effects in hue-temperature gradient for BM/RS40C8W TCLs which were super-heated 40 % (top) and 70 % (bottom) of their activity range

$\sigma_H = \sqrt{\frac{1}{N-1}\sum_i^N (H_i - \bar{H})}$, was normalized with the width of the according hue spectrum $H_{max} - H_{min}$ because it is dependent on the measurement range

$$\sigma'_H = \frac{\sigma_H}{H_{min} - H_{max}} \tag{4.5}$$

During the heating progress, the standard deviation within the activity range remains below 25 %. After super-heating, the standard deviation strongly increased up to 40 % of the activity range. Similar to the hue-temperature deviation, hysteresis can be seen.

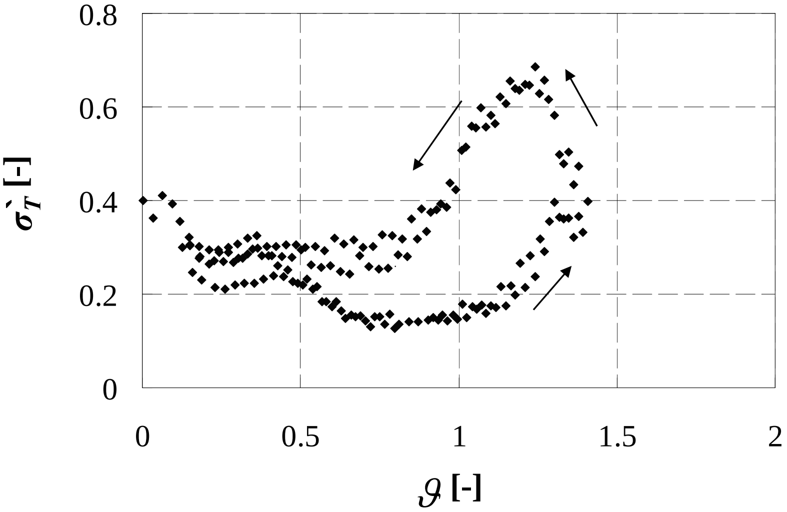

Figure 4.10: Normalized standard deviation over dimensionless temperature for an super-heating of 40% of the activity range

The above mentioned reset effect has also been observed by [2, 7]. Although the cause for the hysteresis is not fully clarified yet, an effect of molecule misalignment is most likely to be expected here. Anderson and Baughn [2] assume that hysteresis is caused by the crystalline structure which behaves differently depending on whether it is heated or cooled. The TLC molecule alignment can be divided into focal conic texture, where the axis of the helices are parallel to the surface and the planar texture where the axis of the TLC helices are perpendicular to the surface. While the planar texture shows good reflective properties, the focal conic texture does not reflect light selectively. The encapsulated TLC normally have a planar texture near the TLC-polymer shell interface. However, when the TLCs are cooled from an isotropic liquid state, the molecules form a focal conic texture, which leads to a decrease in reflectivity and a shift of the hue-values [2]. A sub-cooling of the TLCs leads to a crystalline state and the molecules have the possibility to re-organize resulting in the mentioned reset.

4.3 Influence of Optical Configuration

The optical configuration comprises the illumination and the image capturing part. The properties of illumination are mainly the kind of the light source, its intensity and its direction relative to the object plane. The configuration of the image capturing system namely the camera corresponds to the magnification of the R, G, or B signal. Some cameras exhibit this feature like the camera[6] used in the present work. As already pointed out, these properties have a distinctive influence on the measurement accuracy. In this section, the influence of the illumination direction relatively to the object plane, expressed as illumination angle, and the RGB configuration on the measurement accuracy are investigated.

4.3.1 Angle Between Camera and Illumination Axis

It is well known that the angle of illumination has influence on the hue-gradient over temperature. As a matter of fact it has been observed by several authors for pure TLC-substance (e.g. [51, 12]), encapsulated TLCs sprayed on surfaces (e.g. [12, 18, 21, 30, 48]) and suspended encapsulated TLCs illuminated with a light sheet ([42, 37, 97]). Fergason [31] describes the aberration of the reflected wavelength λ from the illuminated wavelength λ_0 at one axis illumination by means of the Bragg effect from

$$\lambda = \lambda_0 \cdot \cos\left(\frac{1}{2}\left(\sin^{-1}\left(\frac{\sin\varphi_I}{n}\right) + \sin^{-1}\left(\frac{\sin\varphi_C}{n}\right)\right)\right), \tag{4.6}$$

where φ_I and φ_C are the angles of illumination and camera axis and n is the refractive index of the TLCs[7]. Following this equation, the wavelength λ increases with increasing angle φ_I respectively φ_C. An increasing wavelength thus leads to a decreasing hue value. This has been found by [30] and [12] for TLC coated surfaces and fabricated TLC sheets. Günther and Rudolf von Rohr [42] observed the influence of different illumination angles on the activity range width. They figured

---

[6] IDT X-Stream XS-3

[7] Estimated to 1.5 TLC [12]

out that an illumination perpendicular to the camera axis results in the smallest activity range (only 7 % of the activity range, predicted by the manufacturer [45]) while an angle of 50° results in the biggest activity range. Fujisawa et al. [37] used two cameras and a light sheet with the background to measure three-dimensional velocity fields. They achieved similar results like [42] and found the biggest activity range at an angle around 40°. It is questionable if the results for the illumination technique with a light sheet are directly comparable to the volume illumination technique. Therefore the influence of the angle between the camera and the illumination axis is investigated for volume illumination of suspended encapsulated TLCs. The measurement setup is described in section 4.2 and glycerin was used as liquid. Figure 4.11 shows the hue-temperature-gradients for different camera axes. It can be seen that the illumination setup with an angle of 30° is most suitable because it has the largest $\Delta H = H_{max} - H_{min}$ compared to the other curves.

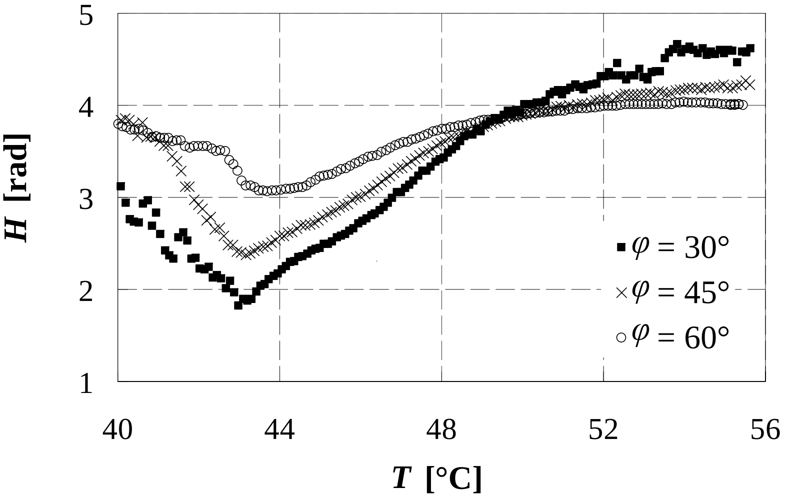

Figure 4.11: Hue-temperature gradients for different angles between illumination and camera axis for volume illumination

The dimensionless standard deviation (equation 4.5) depending on the illumination angle is presented in figure 4.12. It can be seen that the standard deviation is smallest for $\varphi = 30°$ and largest for $\varphi = 60°$. The high deviation of up to 200 % of ΔH at an illumination angle of $\varphi = 60°$ is unacceptable for temperature measurements and mainly caused by the minor ΔH.

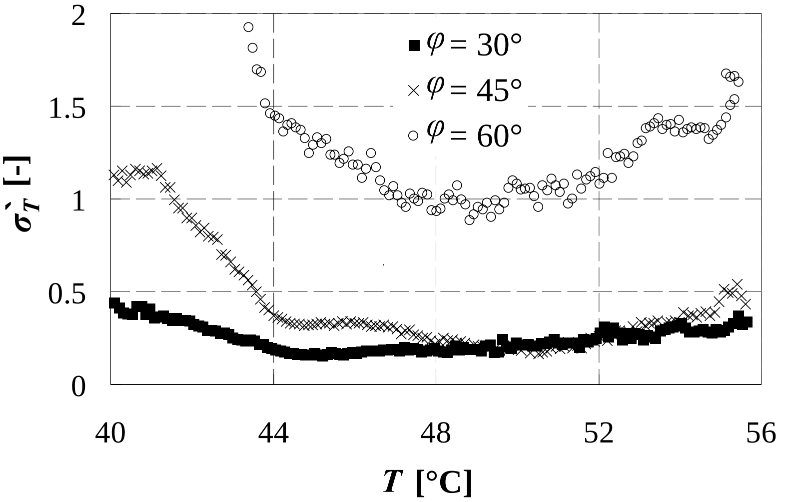

Figure 4.12: Normalized standard deviation gradients for different angles between illumination and camera axis

One supposed influence is that the TLC capsule acts like a lens with aberrations. These aberrations lead to chromatic and geometrical distortion which becomes noticeable in a hue gradient over the particle size.

The influence of different methods of illumination namely volume illumination and light sheet illumination can be seen in figure 4.13. The y-axis represents the dimensionless hue value calculated from

$$\Pi = \frac{H - H_{min}}{H_{max} - H_{min}}. \tag{4.7}$$

The reason for the dimensionless hue value is that the calibration curves have been captured with different cameras and therefore different configurations. Further, it should be noted that both the hue interval and the activity range are strongly depending on the camera configuration. Figure 4.13 should primarely represent the intense influence of the light angle on the activity range and the start temperatures. For $\varphi = 90°$, the activity range is narrowed to 18 % of the activity range at volume illumination with $\varphi = 30°$. Further the start temperature is shifted to lower temperatures for $\varphi = 90°$. Similar results were reported from Günther and Rudolf von Rohr [42]. They investigated several angles between illumination and camera axis and found that the activity range at an angle of $\varphi = 90°$ is 15 % of the activity range at an angle of $\varphi = 50°$.

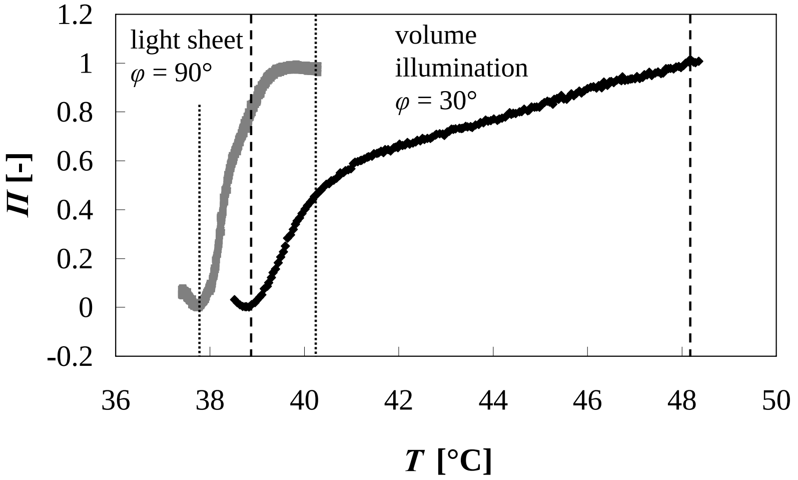

Figure 4.13: Effect of angle between camera axis and illumination on activity range and start temperature. Activity range at light sheet illumination is narrowed to 0.18 of activity range at volume illumination

4.3.2 Color Space Conversion

The transformation of the RGB values into the HSI values is performed with equation 2.2. Because equation 2.2 includes case differentiations, the hue value is dependent on the order of the RGB values. In figure 4.14, it can be recognized that the direction of the hue gradient changes when the order of the RGB values changes.

This case differentiation also effects the measurement range. For a white balance with a low magnification of the blue value, the hue value strongly decreases at higher temperatures. The influence of different camera configurations on the calibration curve is shown in figure 4.15. Here the importance of the camera configuration becomes clear.

Vice versa, it is possible to increase the activity range and the hue spectrum by weighting the RGB values. For that reason, an algorithm has been developed which iteratively determines the best RGB configuration. Here the RGB values are separately multiplied with an amplification factor, m_i until the best possible result, namely high ΔH and low σ'_H, is achieved. To accelerate the calculation, the procedure is convoluted, which means that the step size is large in the first run and then systematically reduced. As a result, a three-dimensional array is created

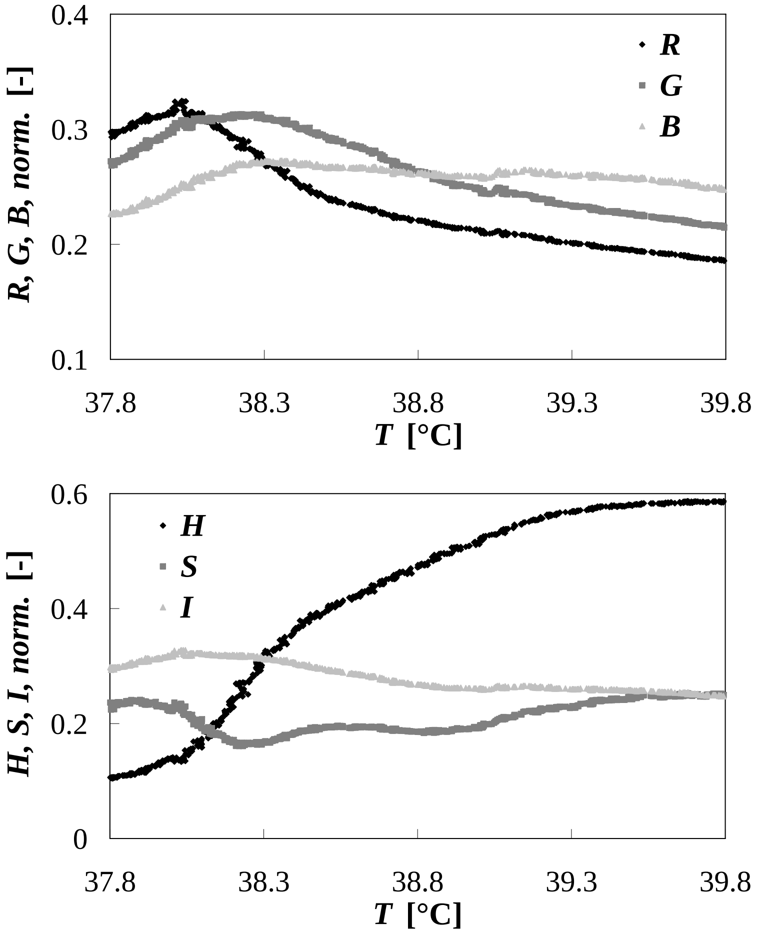

Figure 4.14: RGB and HSI values over temperature

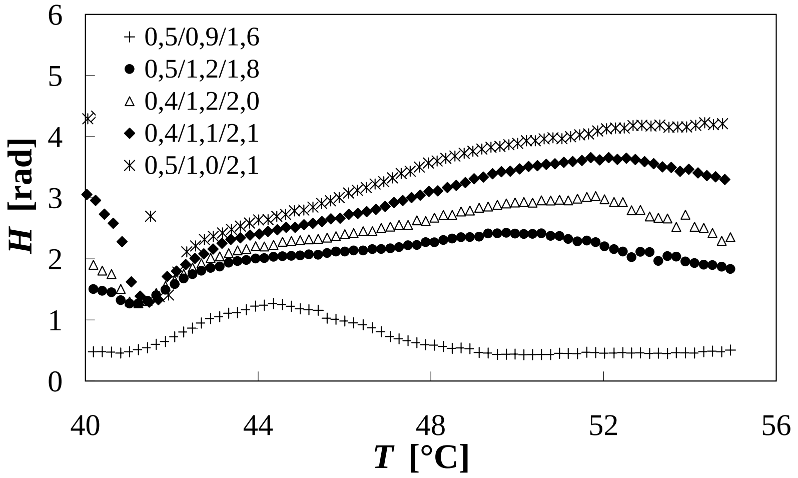

Figure 4.15: Influence of different camera configurations of R/G/B on activity range

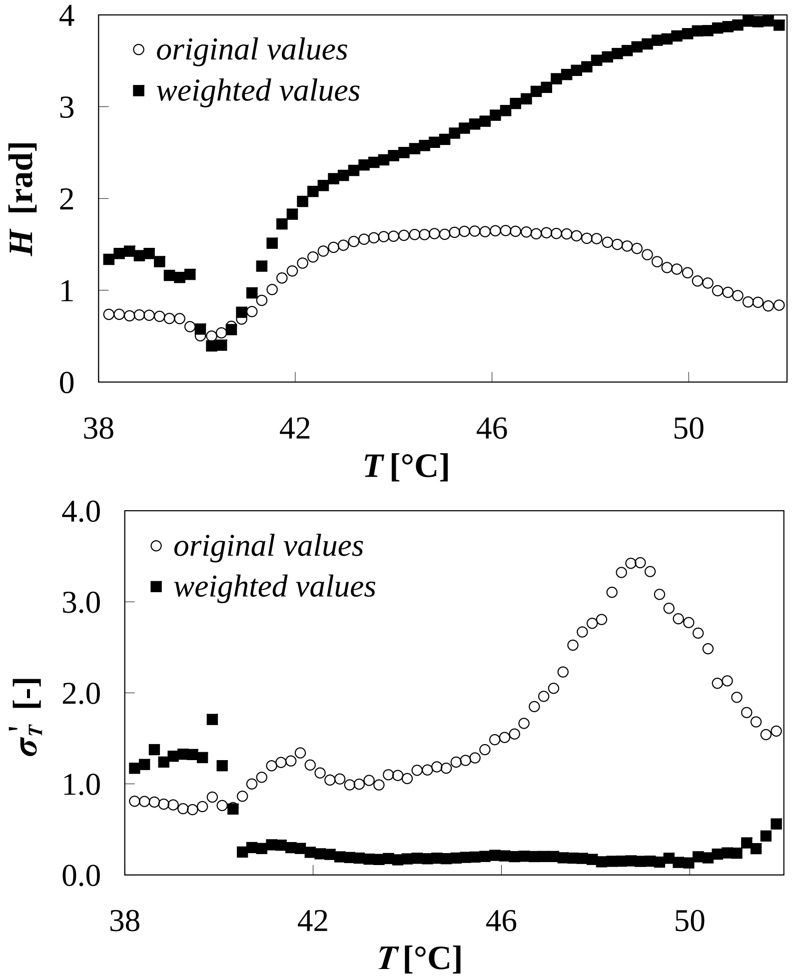

Figure 4.16: Influence of RGB weighting on activity range and normalized standard deviation

which contains the quality grade, G, in dependency of the amplification factors, w_r, w_g and w_b. The quality grade, G, is calculated from

$$G(w_r, w_g, w_b) = \frac{1 - \frac{1}{\Delta H(w_r, w_g, m_b)}}{1 - \frac{1}{20\sigma'_H(w_r, w_g, w_b)}}. \tag{4.8}$$

The factor 20 has been set to maximize the influence of the standard deviation on the quality grade. Figure 4.16 shows the influence of weighting on the hue values H and on the normalized standard deviation σ'_H. Although, for this example, a disadvantageous RGB configuration was chosen, it can be seen that a significant increase of the measurement range is possible with additional weighting of the RGB values.

4.4 Thermal Response Characteristics of Encapsulated TLCs

Many thermodynamic processes are highly dynamic (e.g. nucleate boiling, free streams, eddies behind wakes, etc.) and therefore require a measurement technique with high temporal resolution. The question of whether the TLC measurement technique is applicable for this will be clarified in the following section. Generally, there are two main temporal restrictions of the measurement technique. First, the optical setup, implying the image capturing and illumination, and second, the thermal response time of the encapsulated TLCs itself. Even when high speed cameras are used, restrictions in the maximum capturing frequency exist. This is due to a low signal to noise ratio caused by insufficient illumination and sensors with low quantum efficiency. Nevertheless, while the illumination and image capturing are paid a lot of attention in research and image sensors with higher sensitivity are developed, the thermal response time of the encapsulated TLC is fixed by its physical properties.

Ireland and Jones [57] quantified the thermal response time in 1987. The encapsulated TLCs of chiral nematic type with a narrow activity range have been applied in a layer of 10 µm on a metal foil. By means of the principle of resistance heating, the foil was heated and temperature gradients up to 2600 K/s were achieved. The color play of the TLCs was acquired with a photo-diode and plotted on an oscilloscope. Measurements were conducted at several temperature gradients and the thermal response time was determined to 5 ms.

In the present work, the thermal response time of encapsulated TLCs suspended in liquid is defined as the time which passes until the TLCs react on a temperature change. Contrary to the opinion of many authors, the system for thermal response not only consists of the encapsulated TLC capsule itself but also of the adhering liquid on its surface. Thus the following components take part in the thermal response:

- Adhering liquid - heat conduction and heat capacity
- Capsule - heat conduction and heat capacity
- TLC substance - heat conduction and heat capacity

- TLC substance - phase change and reorienting the molecule structures

This fact has been taken into account by Kobayashi and Saga [64] who did numerical investigations on encapsulated TLCs in liquid. They modeled the TLC-core, the capsule and the surrounding liquid. Different temperature functions were used as a boundary condition and the response of the system was calculated. When excited by step function of surrounding liquid temperature, the TLC core needed 150 ms until it reached 99 % of the temperature of the surrounding liquid. Kobayashi und Saga estimated the highest frequency to be 20 Hz which occurs at a vertical free stream and discovered that the TLCs could follow such a frequency. Therefore, the system is applicable for highly dynamic measurements. Following Ireland and Jones, Wagner and Stephan [139] investigated pure TLC material which was applied as a layer on a metal foil. The foil was heated harmonically and the TLC color play was measured with a RGB high speed CMOS camera[8]. Wagner and Stephan investigated different layer thicknesses (10, 20 and 40 µm) and observed that the pure TLC substance follows frequencies up to 70 Hz. The phase shift between the temperature of the heating foil and thus the thermal response was determined to 60° which corresponds to 5 ms, approximately.

4.4.1 Experimental Procedure

To investigate the thermal response characteristic of encapsulated TLCs, two different kinds of stimulation have been chosen. A harmonic temperature change of the surrounding liquid leads to a harmonic temperature response of the TLCs with the same frequency, a certain phase shift and a smaller amplitude. The phase shift and the attenuation of the amplitudes give information about the thermal response.

The other kind of stimulation is a linear temperature increase of the liquid which is caused by a step function of the heat flux. The temperature increase depends on the rate of the heat flux.

To achieve the previously described temperature stimulations, the encapsulated TLCs were suspended in a thin liquid layer which is electrically heated by a stainless steel foil. Therefore, the measurement setup of Wagner [139] was modified for

---

[8] IDT X-Stream XS-3

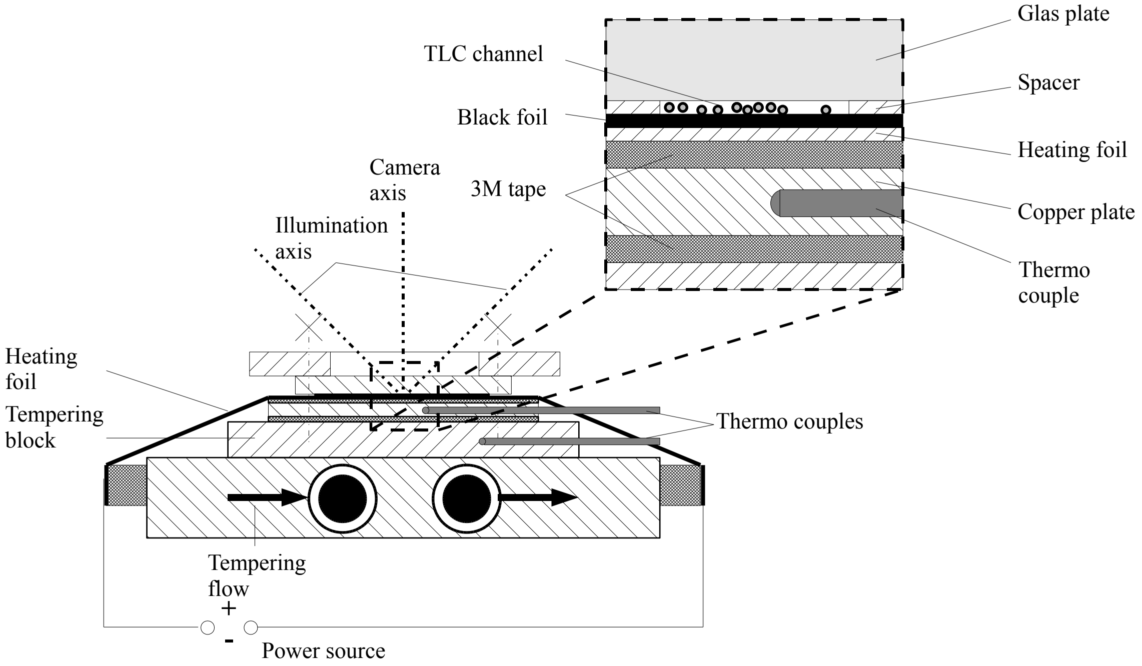

Figure 4.17: Sketch of the setup for measuring thermal response characteristic of TLCs. Camera axis is in vertical direction from the top

the use of encapsulated TLCs. The whole setup is briefly described; for detailed information, see [139]. Glycerin has been chosen as a test liquid because of its lower vapor pressure and higher viscosity which simplify the fixing of the suspension in a narrow channel (figure 4.17). The color play of the encapsulated TLCs was captured with a high speed CMOS RGB camera. Two cold light sources[9] were employed for the illumination and the light was guided with two fiber optics to the FOV.

The side walls of the channel were two metal foils with the defined thickness of 20 μm and a glass slide served as top wall. To minimize the reflections from the background, a thin black foil was coated on the stainless steel foil. The heat removal was done via a copper block which was tempered by a secondary cooling loop[10]. To measure both the temperature of the copper block and the heat flux, a small copper plate with a hole for a thermocouple was adhered with thermal conductive tape[11] between the heating foil and the copper block. As already mentioned, the heating was realized with the electrical resistance principle of the

---

[9] Schott, KL2500, 250 W, external power supply were used to provide true direct current

[10] Huber Ministat 125

[11] 3M conductive tape

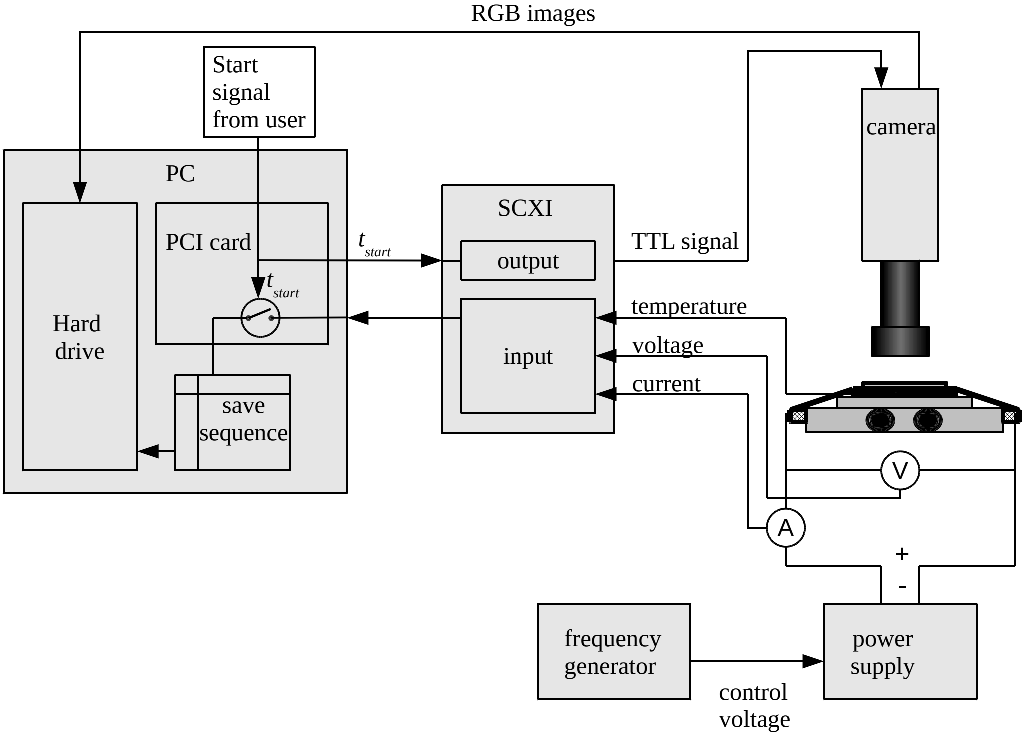

Figure 4.18: Schematic sketch of the signal flow

metallic foil. Beyond that, a power supply[12] was controlled by a frequency generator[13] which is able to generate periodic signals (step function, saw-tooth, sinus etc.). For a simultaneous acquiring of the color play and the heating power, the camera and the data acquisition system[14] are synchronized, which is schematically pictured in figure 4.18.

To measure the temperature response of the TLCs, 25 images were acquired per heating period. For heating frequencies from $2 - 28\,\text{Hz}$ this leads consequently to a measuring frequency from 50 - 700 frames per second. The voltage and current of the heating foil were captured with frequencies 250 times higher than the heating frequency. All in all, 10 heating periods were captured. Hereupon some special image processing algorithms were applied on the images as described as follows. After the single TLC particles are detected and the hue values are allocated, the results are validated and a mean hue value is calculated. With a hue-temperature-

---

[12] Delta Elektronika, SM 15-100

[13] Wavetek, Model 39

[14] National Instruments

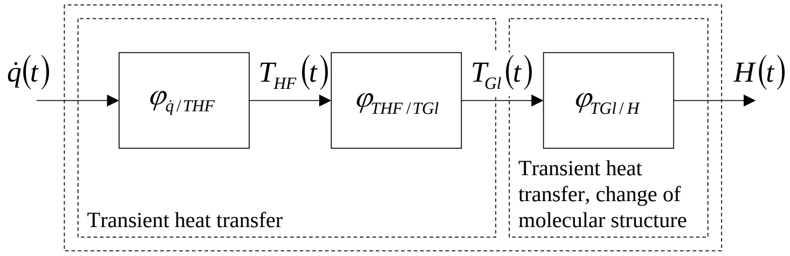

Figure 4.19: Occurring phase shifts of the system and reasons for the phase shifts

calibration curve, taken before the measurement with the same configurations, the temperatures of the particles are calculated.

The experimental procedure for the measurements of the heat flux step function is in principal similar. Because the temperature rise is quite high (up to 700 K/s), 35 images with a measurement frequency of 700 frames per seconds were recorded. After each measurement, the TLCs have been cooled to reach the crystal phase of the TLCs and thus avoid hysteresis.

In this section, the procedure for the determination of the phase shift at harmonic heating is described. The whole system can be defined with the flow chart shown in figure 4.19 where the heat flux of the foil $\dot{q}$ is the input and the color change H the output signal.

Between the harmonic heating and the resulting harmonic temperature change is a certain phase shift $\varphi_{\dot{q}/THF}$. The temperature change of the heating foil leads to a temperature change of the glycerin which again is also connected with a certain phase shift $\varphi_{THF/TGL}$. Finally the phase shift $\varphi_{TGl/H}$ between the temperature of the glycerin layer and the displayed color of the TLCs describes the thermal response of the TLCs (figure 4.20).

The investigation of the thermal response characteristic of the TLCs is based on measuring the response of the TLCs on the heating function. The other mentioned phase shifts cannot be measured directly and have to be determined numerically and analytically. Therefore the analytical approach from Wagner [139] was employed. The heat flux emerging from the heat foil is directed to the heat sink in the copper block. This assumption is justified, since heat flux through the glass plate is less than 1% of the total heat flux. Furthermore, due to the thin heating foil

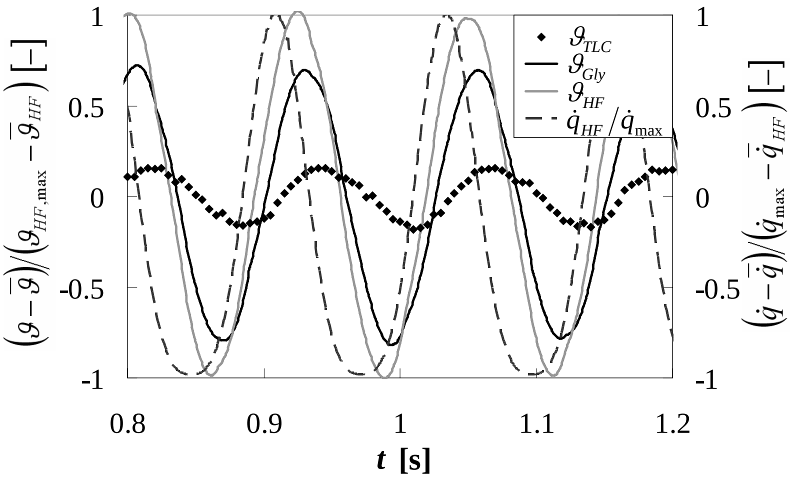

Figure 4.20: Calculated dimensionless temperature gradients of the heating foil and glycerin, measured dimensionless temperature gradients of TLCs and dimensionless heat source

(10 μm), the temperature change within the foil is neglected. The energy equation then reduces to

$$\rho \cdot c \cdot \delta \frac{\partial T_{HF}}{\partial t} = \dot{q} - \alpha(T_{HF} - T_{CU}), \tag{4.9}$$

where ρ, c and δ describe the density, specific heat capacity and thickness of the stainless steel foil and α the heat transfer coefficient near the foil. The phase shift between the heat flux gradient and the temperature gradient of the heating foil is then calculated from

$$\varphi_{q/THF} = -\arctan\left(\omega \frac{\rho \cdot c \cdot \delta}{\alpha}\right) \tag{4.10}$$

with the angular frequency $\omega = 2\pi \cdot f$ and f as the frequency of the periodic heating. The phase shift between the temperature gradient of the heating foil and glycerin, $\varphi_{THF/TGl}$ is determined numerically. Therefore a simple model has been created with PDE-toolbox[15] of Matlab[16]. Cross-correlating of the glycerin temperature gradient and the indicated temperature gradient by the TLCs leads to the phase shift and thus to the thermal response time. The resolution of the results was enhanced by sub resolution accuracy algorithms as described in section 3.3.

---

[15] Partial differential equation

[16] Mathworks Inc.

The phase shift of the stimulation by a step in the heating power was determined as described in this section. The temperature of the glycerin is calculated numerically and compared with the measured temperature of the TLCs. For small time intervals, linearly functions can be approximated to the curves. As illustrated in figure 4.21, the time difference is determined from the intersections of the straight lines with the x-axis.

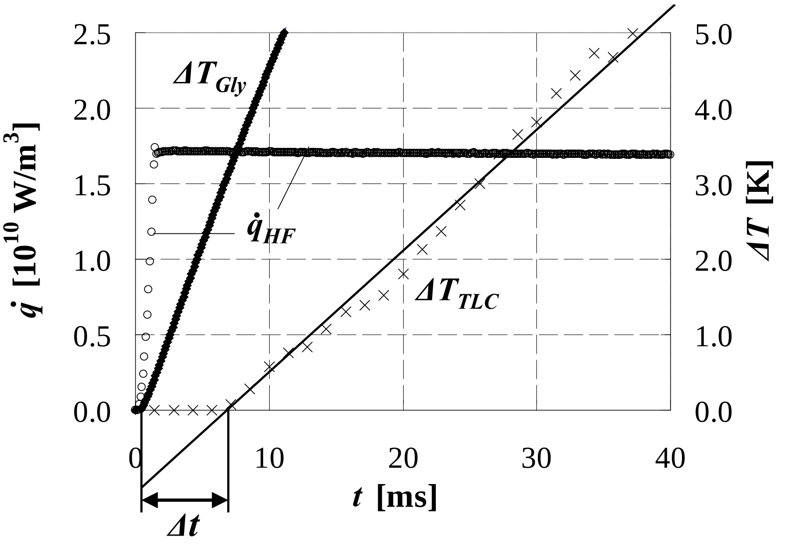

Figure 4.21: Measured temperature difference of TLCs and calculated temperature difference of glycerin over time. Stimulated by step function of heating power

4.4.2 Results

Harmonic temperature excitation

Because of high image capturing frequencies, the RGB signals needed to be intensified, which was realized with the camera. This, however, resulted in erroneous RGB measurements and therefore high uncertainty in temperature measurements. On this account, deviations of the temperature up to 100 % occured, which narrows the quantitative validity of the results. Nevertheless, when regarding the averaged amplitudes (arithmetical mean of five measurements) an asymptotic behavior of the amplitue attenuation to values of $A_{TLC}/A_{Gl} \approx 0.2$ can be seen in figure 4.22.

The thermal response time is calculated with

$$\Delta t = \frac{\varphi_{TGl/TTLC}}{360^\circ}\frac{1}{f} \tag{4.11}$$

and is shown in figure 4.23. Also shown in figure 4.23 is the thermal response time of Wagner [139] for pure TLC substance. The two curves show the same logarithmic characteristic: a high decrease of the thermal response time at lower frequencies and an asymptotic behavior at higher frequencies. Wagner investigated TLCs as surface thermometer and thus defined the thermal response time as phase shift between the temperature of the heating foil and the indicated temperature of the TLC substance.

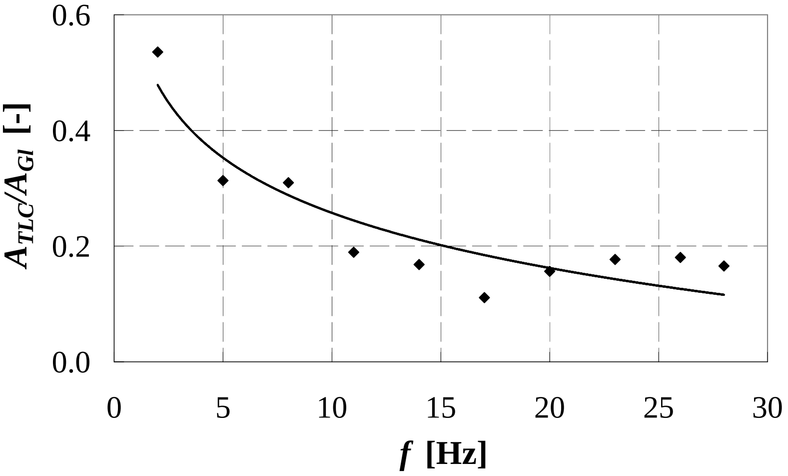

Figure 4.22: Amplitude ratios for indicated temperature of TLCs and calculated temperature of glycerin

Ramp-like temperature excitation

According to Ireland and Jones [57], the thermal response time of encapsulated TLCs was investigated and some typical temperature gradients are shown in figure 4.24. It can be seen that the temperature gradients of glycerin and TLCs are different. This is attributed to the heat storage of the TLCs, which again can be compared with the amplitude attenuation observed for the harmonic excitation.

In figure 4.25, the estimated thermal response is shown for different temperature gradients $\dot{T} = \frac{dT}{dt}$. As expected, the behavior is similar to the thermal response characteristic for harmonic excitation: the thermal response shows a

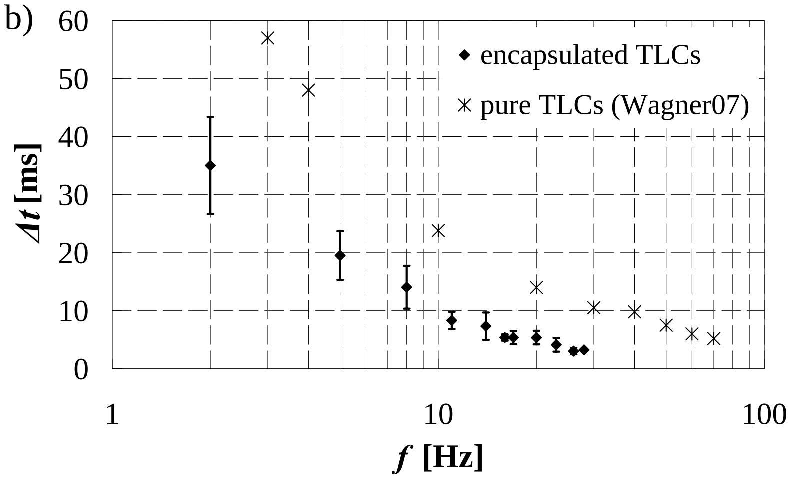

Figure 4.23: Calculated thermal response time with 4.11 for measurements of [139] and author

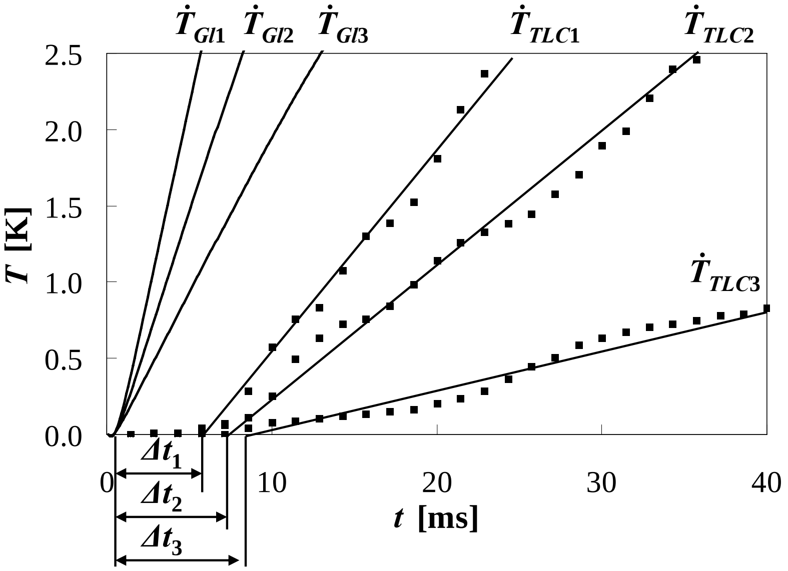

Figure 4.24: Calculated temperature of glycerin and measured temperature of TLCs for $\dot{q}_1 = 1.71 \cdot 10^{10}\,\mathrm{W/m^3}$, $\dot{q}_2 = 1.08 \cdot 10^{10}\,\mathrm{W/m^3}$, $\dot{q}_3 = 0.6 \cdot 10^{10}\,\mathrm{W/m^3}$

strong decrease at lower gradients and an asymptotic behavior at higher temperature gradients. The results presented here differ from the results of Ireland and Jones in some points. Ireland and Jones did not observe dependency of the thermal response time on the exciting temperature gradient. Furthermore, they measured a thermal response time of $\Delta t \approx 3\,\mathrm{ms}$. A reason for this might be the higher temperature gradients of $\dot{T} \approx 2700\,\mathrm{K/s}$ they achieved with their setup or a different kind of TLCs.

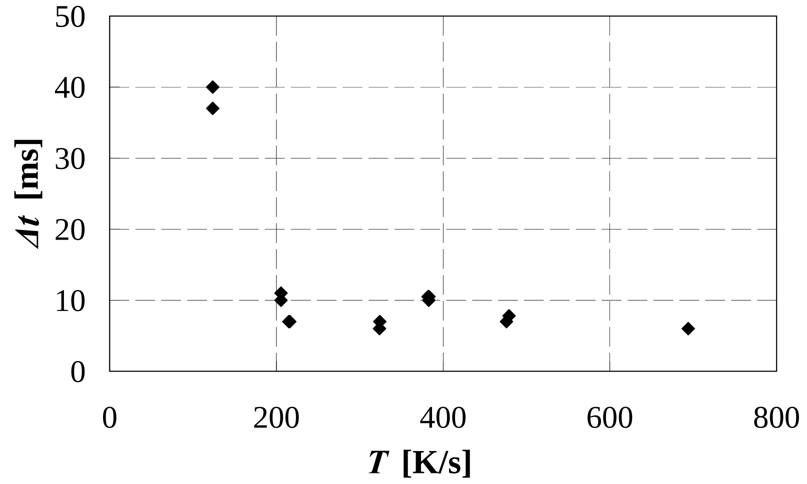

Figure 4.25: Thermal response time of TLCs for different temperature gradients of heating foil

Measurement Accuracy

As already suggested, the thermal response time measurements are quite prone to error.

For a detailed discussion of the measurement errors see [137]. A comparison of several measurements at the same parameters has shown that uncertainties up to 100 % occur. Nevertheless, it can be concluded that the thermal response time is less than 10 ms at high frequencies.

4.5 Enhancement of Measurement Accuracy

In this section, different image processing methods are presented to enhance the measurement accuracy afterwards. Although careful experimental procedure is essential, some specific errors can be minimized as shown below.

4.5.1 Local Calibration

In section 4.1, low frequency noise of the spatial distribution of the hue signal has been mentioned whose origin is addressed to inhomogeneous illumination. Since the calibration procedure is done in-situ and thus, the illumination conditions do not change, the error can be seen as a bias error. Local calibration polynomials can then be applied for a reduction of the error. Therefore, the area of interest (AOI) is divided into interrogation areas (IAs) with a proper size (e.g. $32\,x\,32$ pixel). From the series of the images taken at several homogeneous temperatures, a particular calibration curve is created for each IA. The effect of the local calibration is shown in figure 4.26. The dimensionless deviation of the temperature is calculated with

$$\sigma_T' = \frac{\sigma_T}{T_{max} - T_{min}} \tag{4.12}$$

where T_{max} and T_{min} are the start and end temperatures of the activity range and σ_T is the standard deviation of the calculated temperatures of the homogeneous temperature distribution. The effect of the local calibration is significant and the uncertainty is reduced about 5 % in the higher activity range.

4.5.2 Background Subtraction

Comparable to local calibration, background subtraction also helps to minimize systematic error caused by illumination and image capturing. In figure 4.27, the influence of the background subtraction on the hue values is shown. The measurements were conducted in the convection cube, and are described more deeply in 4.6. Nevertheless, it can be seen that the background subtraction (in the right image) leads to a higher bandwidth of hue values and to a more meaningful distribution. The top wall seems to have negative influences on the hue field because the hue values are relatively small here. This again implies lower temperatures at the top which contradicts the typical temperature distribution of free convection.

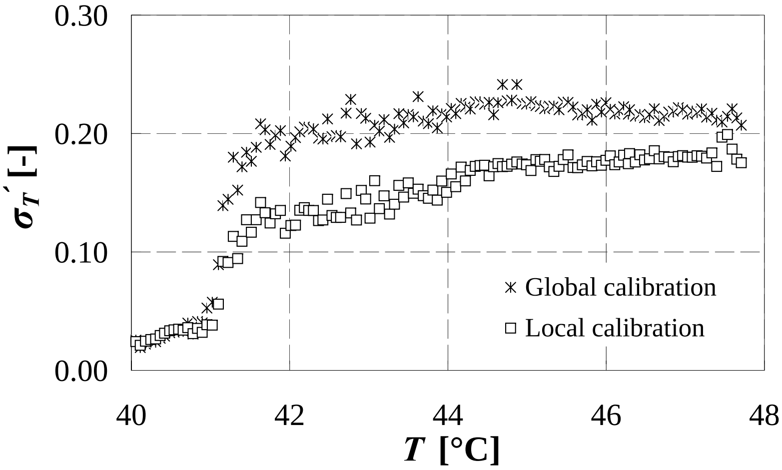

Figure 4.26: Influence of local calibration on measurement accuracy

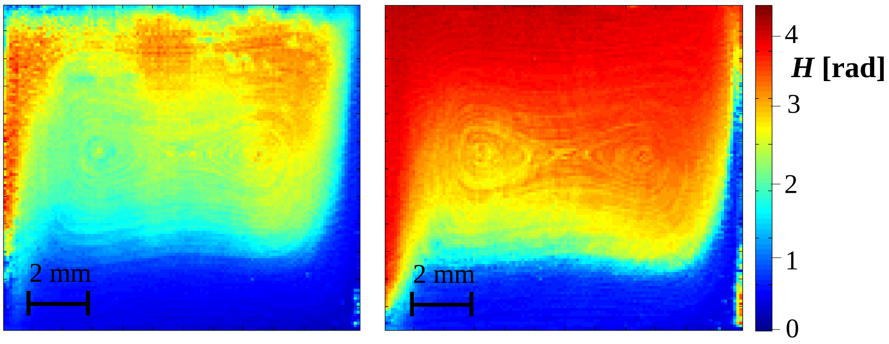

Figure 4.27: Hue distributions without (left) and with (right) RGB image background subtraction

4.5.3 Temporal and Spatial Filtering

Both the influences of spatial and temporal averaging on the measurement uncertainty are presented in figure 4.28. The temporal averaging is the number of images which are arithmetically averaged, while the spatial averaging is expressed by the size of the interrogation area. Therefore the image is divided into interrogation areas with a certain size. When doing measurements with high spatial resolution and the temperature information is achieved from single TLC capsules, the size of the interrogation areas strongly depends on the average number of particles per interrogation area. In the present case, an interrogation area size of 16 *x* 16 pixels leads to 2 particles per interrogation area in the mean, and subsequently 24 *x* 24 pixels to 4.5 particles and 32 *x* 32 pixels to 8 particles. In the present case, images at an homogeneous temperature distribution of 38 °C were recorded, which is located in the beginning of the activity range of the used TLCs BM/R40C8W/S-40 when applying a light sheet for illumination (when applying a light sheet, the activity range is narrowed and shifted towards smaller temperatures as shown in section 4.3.1). The measurement setup and procedure is explained in the following section 4.6.

Regarding spatial averaging, the uncertainty decreases with increasing size of the interrogation area (figure 4.28). This is self-evident because more particles contribute to the temperature determination per interrogation area. Also self-evident is the decrease of uncertainty with increasing number of images up to a certain amount of images. The statistical distributed temporal noise mainly arises from the unequal hue values of the TLCs. Further temporal averaging leads to an asymptotic behavior of the uncertainty. The reason therefore is located in error sources addressed to spatial nature. Most of them are caused by optical effects like in the example of inhomogeneous illumination, background reflections and image capturing.

The influence of temporal averaging is visualized in figure 4.29. For spatial averaging, low pass filtering of 4 *x* 4 pixels was applied. It becomes clear that the white temporal noise is strongly reduced by averaging over $N = 10$ images and a relatively smooth image is achieved by averaging over $N = 50$ images. The increase of the accuracy by further averaging over $N = 100$ images is minimal. Nevertheless, it is obvious that averaging over $N = 10$ images directly leads to an enormous loss of temporal resolution. On the other hand, the temperature distri-

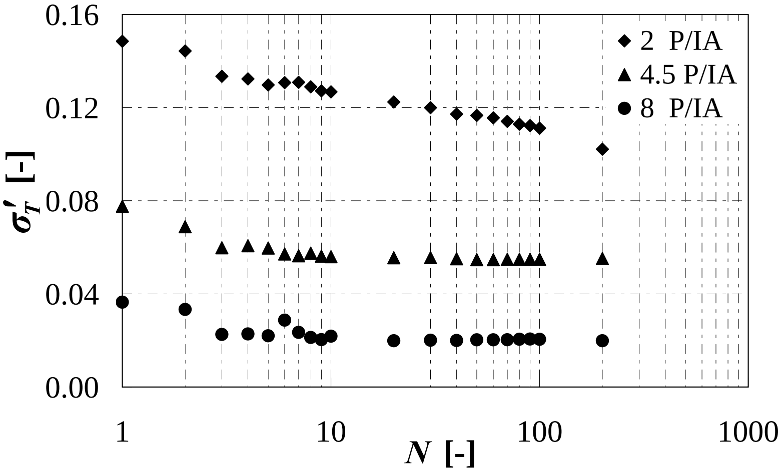

Figure 4.28: Normalized spatial standard deviation of temperature values over number of averaged images for different interrogation area sizes. Every IA contains averaged 2, 4.5 and 8 particles at a temperature of 38 °C with BM/R40C8W/S-40

bution after an averaging of only $N = 5$ images is not acceptable for temperature measurements with proper quality.

4.6 Measurement of Temperature Fields of Free Convection

The subject of this section is to characterize the LCT method regarding its temperature measurement accuracy. This can be done by measuring homogeneous temperature fields or by comparing measured with numerically calculated temperature fields. On this account, a flow of thermal induced free convection inside a cube is chosen. The convection is induced, when two opposite vertical side walls have different temperatures and the remaining walls are adiabatic.

4.6.1 Experimental Procedure

The setup, which is called in the following convection cube, is shown in figure 4.30. For establishing a homogeneous temperature distribution of the side walls, two secondary flows were employed: one is connected to a heating[17] and the

---

[17] Lauda Ecoline E100

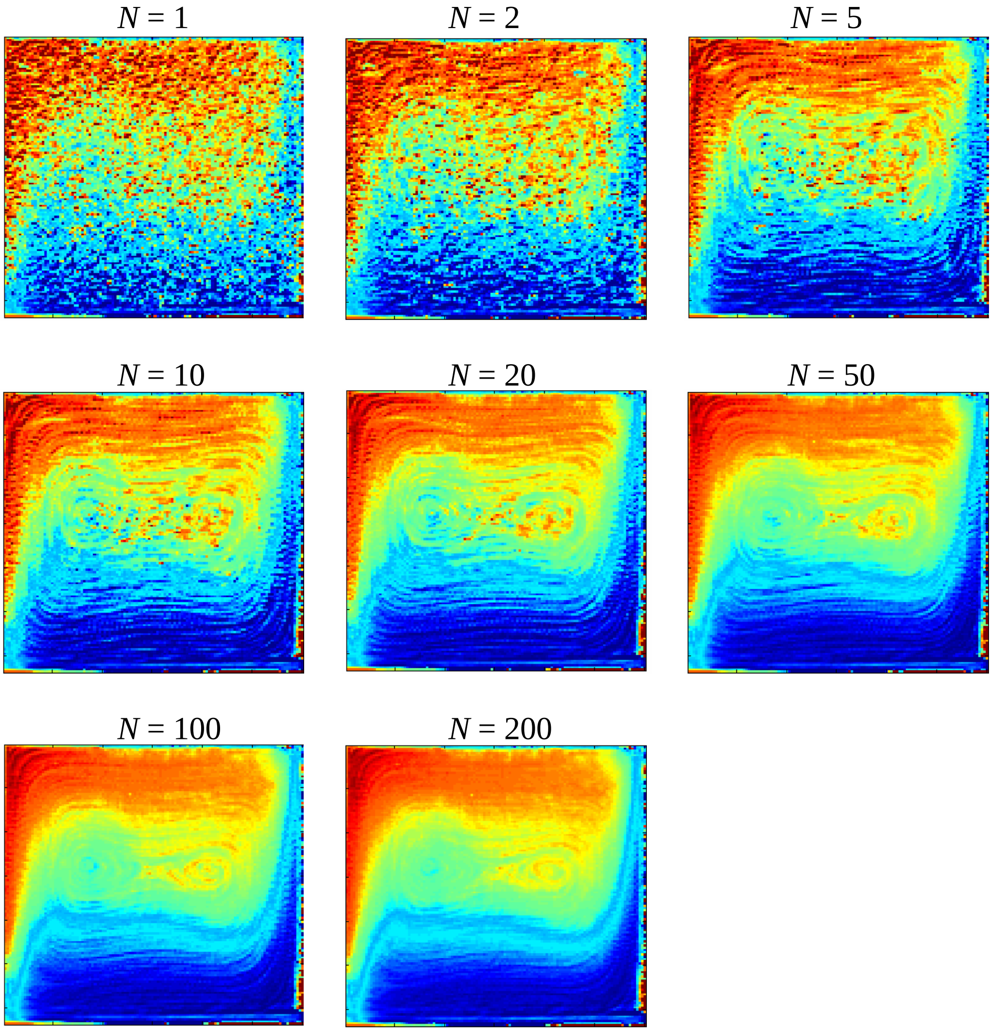

$N = 1$ $N = 2$ $N = 5$

$N = 10$ $N = 20$ $N = 50$

$N = 100$ $N = 200$

Figure 4.29: Influence of temporal averaging. N donates the number of images incorporating in arithmetical average

Fluid properties	Water	Glycerin
Density ρ $[kg/m^3]$	993.4	1249.3
Kinematic viscosity ν $[m^2/s]$	$7.016 \cdot 10^{-7}$	$2.529 \cdot 10^{-4}$

Table 4.1: Fluid properties of water and glycerin at 38 °C

other to a cooling[18] thermostat. The secondary flows are piped through the copper blocks which serve as temperature dampers and work as side walls in the cavity. With this method, an almost constant wall temperature of the copper blocks can be achieved, which is measured by four thermocouples soldered in each wall. Because both copper walls must have the same temperature during the calibration process, the tempering liquid flow can be looped in a way that both copper blocks are streamed with the liquid from the cooling thermostat. Beside the copper walls, the other walls are made of PMMA with a wall thickness of 10 mm so that they are almost adiabatic and a cubic cavity is formed with a side length of 12 mm. The liquid is filled into the cavity through a hole in the bottom wall by means of a syringe and the air can exhaust through four holes in the top wall.

As test liquid deionized water was used which is chemically compatible with the polymer shell of the encapsulated TLCs and does not affect the PMMA walls. On the other hand, water has a lower density than the encapsulated TLCs which results in the sinking of the TLC capsules. To minimize this effect, glycerin was applied. It showed that glycerin did not perfectly mix with water and due to this the TLC capsule distribution was not homogeneous. Pure glycerin has a too low viscosity which again leads to low thermal induced free convection at moderate temperatures. Eventually, the sedimentation of the TLC capsules in water was accepted and its velocity in direction of gravitation can be calculated with equation 4.4. The sedimentation velocities for water and glycerin at 38 °C were calculated to $u_{s,water} = 1.62 \cdot 10^{-5}\,\mathrm{m/s}$ and $u_{s,glycerin} = -8.5 \cdot 10^{-9}\,\mathrm{m/s}$ with the fluid properties taken from table 4.1.

Because water absorbs air gases (N_2, O_2, CO_2)[19], it was degassed before the measurement. The ability to dissolve gases in water decreases with increasing temperature which is due to hydrogen bonds between water and the gas molecules. These bonds are released with increasing temperature. On this account, the water

---

[18] Huber Ministat 125 cc3

[19] e.g. water at a temperature of 20°C has 15 mg/l of N_2, 9 mg/l of O_2, 0.8 mg/l of CO_2 [50]

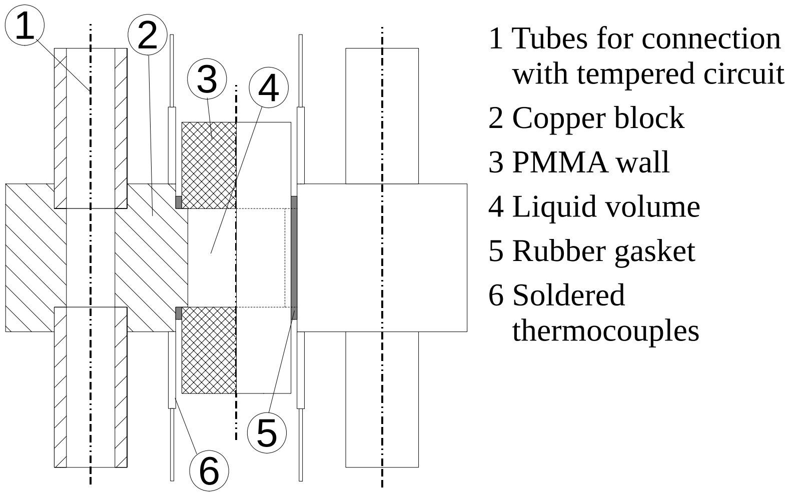

Figure 4.30: Sketch of the measurement setup as crop on the left side and side view on the right side. The camera view corresponds to the side view

was heated to 80 °C in an ultrasonic bath. Ultra sonic has the additional effect that due to the periodic pressure changes, cavitation bubbles are formed. These agglomerate to larger bubbles and support the degassing procedure. Hermann and Fuhrland [50]figured out that after heating water for 100 min approximately 65 % of the air gasses are discharged. The encapsulated TLCs should not be heated far above their blue stop temperature and therefore they are added with a volumetric concentration of $5 \cdot 10^{-3}$ to the degassed water afterwards.

Optical Setup

To obtain 2D temperature fields, the suspension was illuminated by a light sheet and the reflected light was captured with a three chip CCD camera[20]. Because it is very difficult to generate a white light sheet with high intensity, maximum camera exposure time and continuous illumination have been chosen. A cold light source[21] was employed as light source and the light was guided with a fiber to the light sheet setup shown in figure 4.31. It is obvious that the greatest part of light is excluded by the pinhole and the slit mask. With this setup, a lightsheet with an approximate thickness of 1 mm and an opening angle of 2° is realized. With

---

[20] Hitachi, HV-C20M

[21] Schott KL 2500

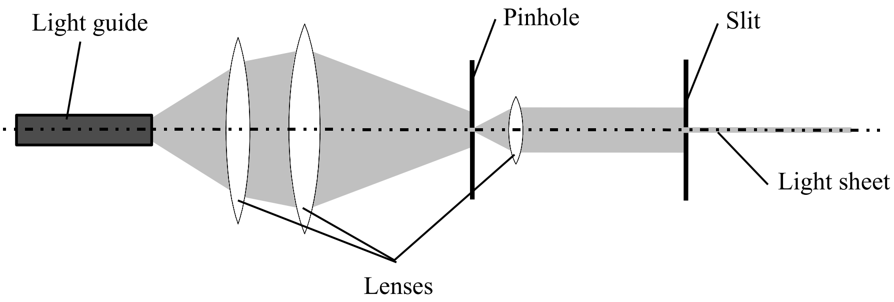

Figure 4.31: Optical setup for generating a light sheet behind a fiber light guide

the applied objective[22] and the resolution of the camera (748 x 576 pixel) one pixel images the area of 25 x 25 µm^2. The frame rate of the camera is 2 Hz.

4.6.2 Results

To verify the LCT measurement method, numerical calculations were performed with boundary conditions according to the experimental procedure. Therefore, the commercial finite element program Comsol Multiphysics[23] was employed to solve the coupled conservation equations. Using the Boussinesq approximation to describe the linear dependency between the liquid density and temperature simplified the numerical procedure. To further simplify matters, only the liquid volume was modeled. Near the isothermal walls, the grid was discretized more precisely in x-direction because higher temperature gradients are expected in this area. Corresponding to the experiment, two opposite vertical walls are defined as isothermal, while the remaining walls are adiabatic.

Temperature Fields

The measured temperature fields were generated by first applying a temporal averaging of 100 images and a spatial averaging of 4 x 4 pixel. Further, the background was subtracted from every single image and one global calibration curve was applied. Figure 4.32 shows the comparison between the calculated and the measured temperature field. Although the temperature profile near the hot wall

---

[22] Schneider, f = 50 mm

[23] Version 3.5

shows discrepancies, all in all, fairly good accordance can be found. Moreover, the occurring noise for the high spatial resolution of 100 µm is relatively low.

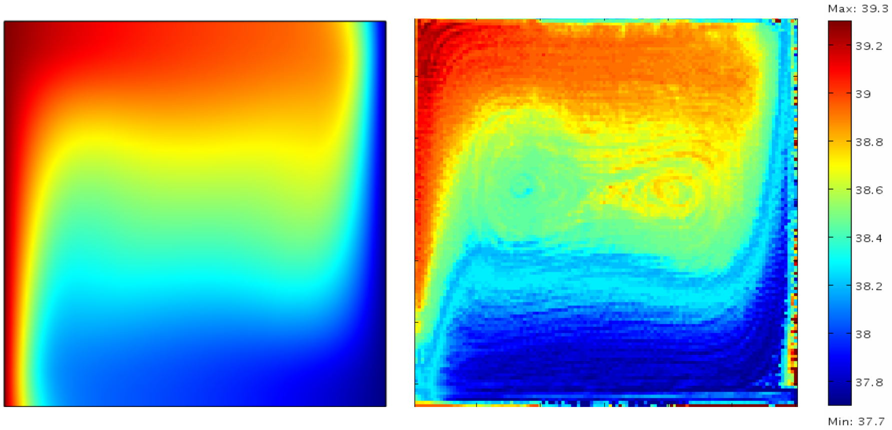

Figure 4.32: Numerically calculated (left) and measured temperature field (right) of thermal induced free convection. Side length is $L = 12\,\mathrm{mm}$

A more detailed comparison is shown in figure 4.33. Here the one-dimensional temperature distribution along the x-axis through the center in the y-z-plane is shown. Discrepancies can be found especially near the walls. The reasons therefore are reflections or shadow effects. Another conspicuous deviance from the numerical temperature field can be seen in the right eddy of the flow. It is assumed that TLC capsules which show a certain abnormality in their light reflective properties, remained on path lines within this eddy. This effect can also be seen in figure 4.34 left, which shows the particle path lines.

Flow Fields

When superimposing the intensity images, the path lines of the particles become visible which are shown in figure 4.34 (left) for $N = 200$ images. On the right side of figure 4.34, the velocity field, achieved by PIV algorithms, can be seen. For the PIV procedure, the program ED PIV was employed and a total amount of 200 images was analyzed. Because the acquisition rate of the CCD camera is rather low (2 Hz), the particle movement in the region of highest velocities (near the hot wall) was approx. 20 pixels from image to image. This again leads to the demand of a large interrogation area - in the present case 44 *x* 44 pixels. The interrogation area

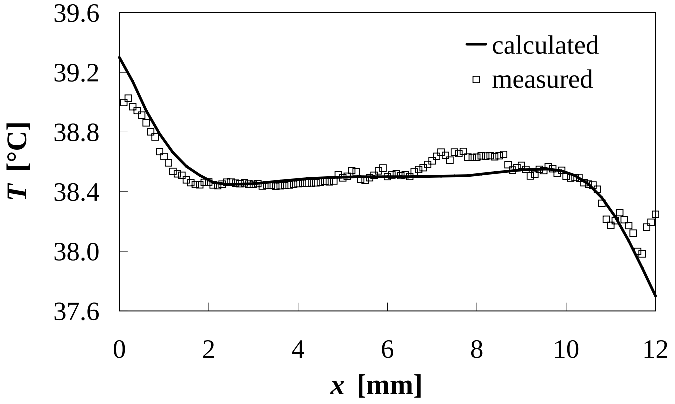

Figure 4.33: Measured and calculated temperature distribution over x at $y = z = 0.5\,L$

needs to be at least twice the size of the highest occurring particle displacement. Of course, large interrogation areas lead to low spatial resolution which can be seen in the near wall resolution of figure 4.34 (right).

The influence of the large interrogation area can also be seen in figure 4.35. The peaks of the velocity in y-direction near the wall are dampened. Nevertheless, it is possible to use TLCs as tracer particles for PIV measurements and therefore to obtain velocity fields simultaneously.

4.7 Measurement of Temperature Fields in a Mini Channel

In this section, the temperature and velocity measurements of a recirculating flow through a mini channel are presented. The flow was scanned in the third dimension, meaning along the camera axis, by moving the camera stepwise. To the author's knowledge, volume illumination is applied for the first time for flow measurements in a channel, and it is shown that volume illumination in combination with scanning the flow can be used for 3D temperature measurements in stationary flows. Furthermore, the measurements were conducted with frequencies up to 1 kHz to prove that it is principally possible to capture with such high frequencies.

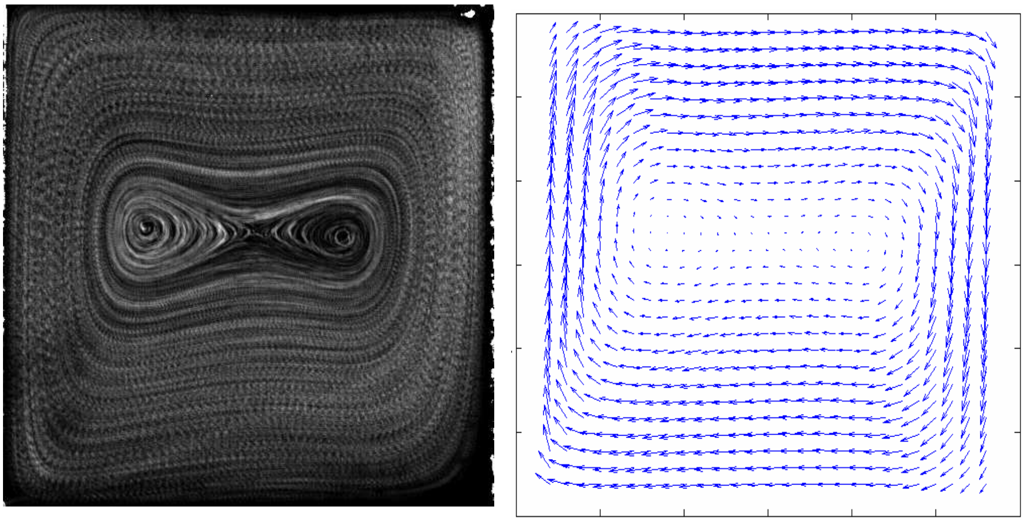

Figure 4.34: Path lines (left), velocity field (right) of thermal induced free convection in a cube with side length $L = 12\,\text{mm}$. The overlapping of the interrogation areas of the velocity field is 75 %

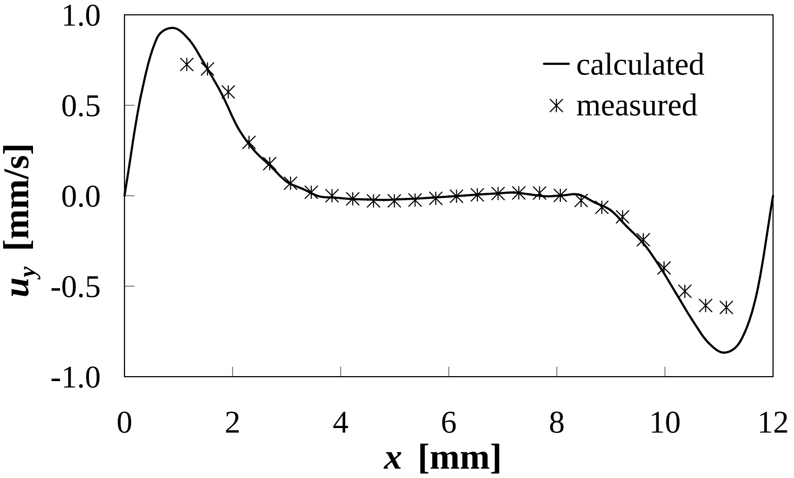

Figure 4.35: Measured and calculated distribution of velocity in y-direction over x at $y = z = 0.5\,L$

4.7.1 Experimental Procedure

The measurements were performed in a narrow channel with a width of 2 mm and a height of 4 mm which is the middle channel of three parallel channels milled in a copper block. The copper block is heated by heating cartridges, and the temperatures are sensed by thermocouples[24]. The upper channel wall is provided by an PMMA wall, which is at the same time an adiabatic wall (see figure 4.36). A detailed description of the setup is given in [114]; the setup has been merely modified for lower volume rates by establishing a second bypass and additional needle valves.

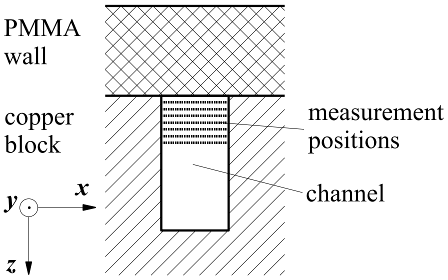

Figure 4.36: Sketch of the channel, flow direction is in y-direction

As already mentioned, volume illumination was employed, using two cold light sources[25]. As can be seen in figure 4.37, the light was guided by two fibers to the measurement section. During the experiment, an opaque drapery enclosed the optical setup so that no background light affects the measurements. The optical setup is mounted on a carriage and the step-wise movement of the camera is realized by a step motor which is controlled by a computer. To measure the z-position, an optical sensor[26], based on the chromatic principle, was employed. In combination with the optical setup, an accuracy of approximately 1 µm is achieved.

The encapsulated TLCs[27] were suspended with a volumetric concentration of $3 \cdot 10^{-3}$ in water. Problems of TLC sedimentation during the measurements can be neglected due to high flow velocities. In the reservoir, where the suspension has a higher residence time, an electric stirrer was installed. For the calibration, two needle valves, right before the entrance and behind the exit of the channel, were

---

[24] Type K, Electronic Sensor, $d = 0.5\,\text{mm}$

[25] Schott KL 2500

[26] Precitek Optronik GmbH, CHRocodile E

[27] Hallcrest, BM/R40C8W/S-40

integrated. When they are closed, the suspension rests in the channel. The liquid in the channel was heated up slowly and every 0.05 K, 10 images were captured according to the description of the signal flow given in section 3.3.

Due to the low liquid circulation, the TLCs start to sink and a change of the suspension every few minutes became necessary. The calibration process was therefore split into several parts. Nevertheless, the parts of the calibration curve fitted together and a calibration curve over the whole activity range was reconstructed. During the measurement, first the upper interface between liquid and PMMA was focused by means of adhering TLC particles. The camera was moved stepwise and every 50 µm, 10 images were acquired which is exemplarily indicated as black dotted lines in figure 4.36.

With the optical setup, a pixel image size of 2.48 µm/pixel was achieved which results in a FOV of 3.17 *x* 2.54 mm^2 at full resolution (1280 *x* 1024 pixel). The measurement depth is estimated to be $\delta z_{PIT} = 200\,\mu\text{m}$ for the temperature measurements and $\delta z_{PIV} = 250\,\mu\text{m}$ for velocity measurements. In this section, the determination of the measurement depth is briefly explained. Ideally, a point source with an infinite small diameter which is located at the object plane is imaged as a point on the image plane. In reality, the intensity distribution of the imaged point source is Gaussian like due to aberration and diffraction effects. With increasing distance from the object plane, the imaged light source appears larger and blurred. Meinhart et al. [89] define the correlation depth as the maximum distance of a point source from the object plane, so that it still contributes to the PIV analysis. The determining factor is ξ which describes the intensity attenuation of the imaged point source. Meinhart et al. use $\xi_{PIV} = 0.1$, which means that all particles images contribute to the PIV analysis, which have an intensity of 0.1 of the in-focus particle image intensity. The depth of correlation, δz, then can be determined by

$$\delta z = \frac{3n \cdot \lambda}{NA^2} + \frac{2.16 d_P}{\tan(\beta)} + d_P \tag{4.13}$$

with the wavelength of the reflecting light, λ, the particle diameter, d_P, the numerical aperture, NA and β, which is related to $NA = n \cdot \sin(\beta)$. However, the numerical aperture NA is not available for the employed optical setup. On this account, measurements were performed to estimate the depth of field which are presented in figure 4.38. TLC particles were dried on a glass plate and heated from

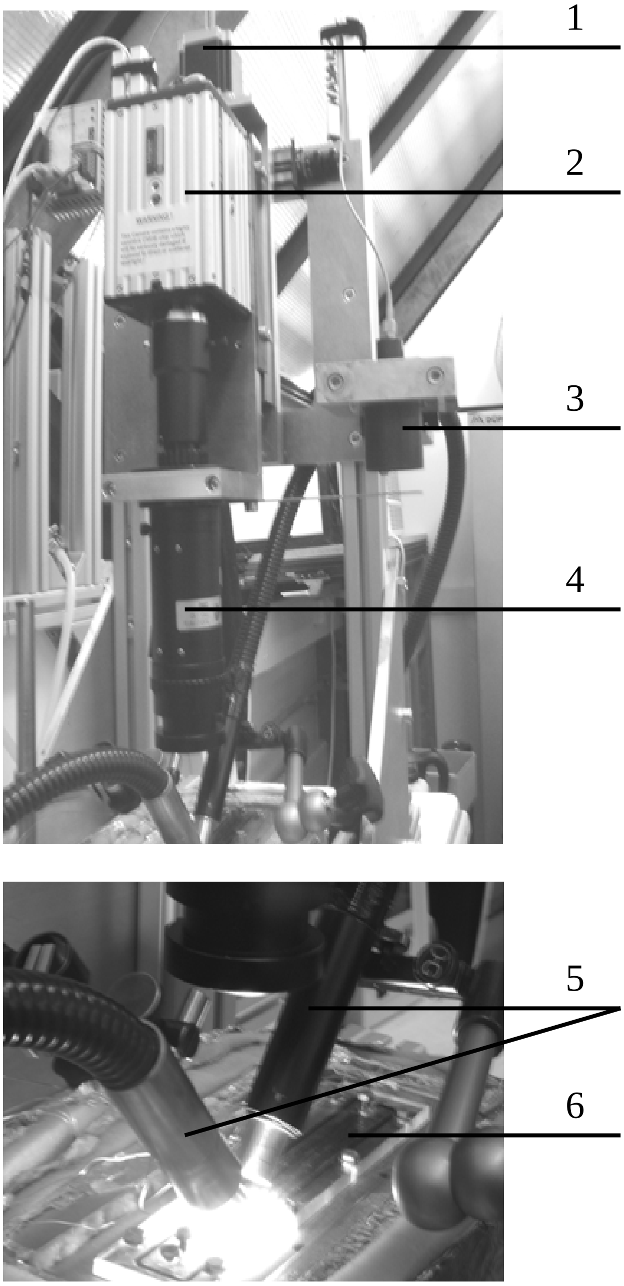

Figure 4.37: Optical setup with 1: step motor, 2: RGB CMOS camera, 3: optical distance sensor, 4: long distance microscope, 5: optical fibers connected to two light sources, 6: mini channel

the bottom. The camera was moved stepwise by means of the setup described above. The image algorithms (see section 3.3) including particle detection and diameter determination were applied to achieve both the particle image diameter and maximum intensity of the particles. The intensity distribution shown in figure 4.38 is normalized to the maximum intensity in the focal plane $\xi = \frac{I}{I_{max}}$. From figure 4.38, it can be seen that both distributions are Gaussian like. Further, it should be noted that the particle detection of the out-of-focus images is prone to error. According to Meinhart et al. [89], the correlation depth for PIV is $\delta z_{PIV} \approx 2 \cdot 125\,\mu\text{m}$, when $\xi_{PIV} = 0.1$. In the present work, only TLC particles contribute to the temperature measurement whose intensity is $I > 0.3 I_{max}$. This was found by comparing the minimum and maximum particle intensities of the particle info sheets from several measurements. For $\xi_{PIT} = 0.3$, the measurement depth is $\delta z_{PIT} \approx 2 \cdot 100\,\mu\text{m}$.

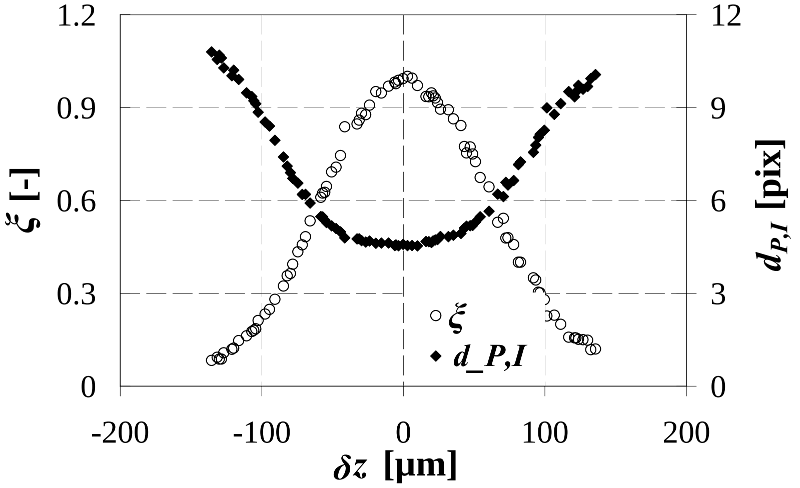

Figure 4.38: Diameter and normalized intensity of TLC particles depending on the distance from the object plane

4.7.2 Results

The measured temperature and velocity distributions are shown in figure 4.39. Because neither the temperature field nor the velocity field vary much in flow direction (this assumption can be made for high flow rates and small considered lengths), the temperature and velocity distributions are plotted against a line in x-direction (see also figure 4.36). Both, the temperature and the velocity distribution exhibit the expected behavior: The velocity distribution shows the expected parabolic shape and tends to zero near the wall. With increasing distance from the top wall, the velocity increases too. Along the wall, the temperature is almost homogeneous which can be explained by the good heat conductive properties of copper. Because the liquid velocity increases in direction of $z = h/2$, the temperature decreases. As can be seen in figure 4.39, only measurements up to a depth of $z = 1\,\mathrm{mm}$ were possible. This is caused by growing measurement noise with increasing depth and thus a drawback of volume illumination.

Validating these results with numerical calculations is not possible since important boundary conditions are not known. Although the temperature in the copper block right beneath the channel was measured, it can not be assumed that the temperature distribution at the walls in z- and x-direction is homogeneous. Another unmeasurable error source is the heat input caused by continuous intense illumination. To minimize this effect, the illumination needs to be pulsed.

Nevertheless, it has been shown volume illumination is a possibility for measurements with high spatial resolution as long there is not too much bulk between the measurement volume and the camera. With the particle tracking method, only TLC capsules which are within the measurement volume contribute to the temperature measurement. Scanning of the flow for 3D temperature field measurements also works when using volume illumination. Further, it has been shown that measurement frequencies up to 1 kHz are principally possible when employing high speed cameras.

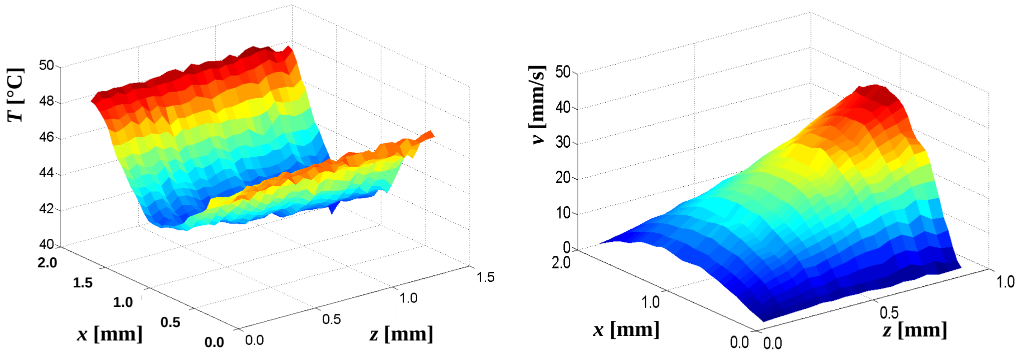

Figure 4.39: Temperature field (left) and velocity field (right)

Part II

Laser Induced Fluorescence

Chapter 5

Experimental Method

This chapter explains the experimental methods for the investigations of the particular LIF techniques. Instead of dividing into experimental setup, experimental procedure and data analysis, it is structured in relation to the extensiveness of the LIF method. The simplest LIF technique, namely the 1C-LIF method, is introduced in section 5.1. As an essential preliminary work for the 2C-LIF, presented in section 5.3, the spectral analysis of different fluorescence dyes is described in section 5.2. Furthermore, in section 5.2 some results of the spectral investigation are anticipated, which are necessary for the comprehension of the optical setup for 2C-LIF. However, the sections of 1C-LIF (5.1) and 2C-LIF (5.3) are again structured in experimental setup, experimental procedure and data analysis.

5.1 One-Color LIF

This section describes the experimental method for the characterization of the 1C-LIF method. To characterize the 1C-LIF method, temperature fields need to be measured, which are comparable with well defined numerically calculated ones. For this reason, measurements were performed with the same setup as the LCT method, namely the convection cube (see section 4.6).

5.1.1 Experimental Setup

In the present work, pulsed illumination is realized with a Nd:YAG laser[1] which has the advantage that high light intensities can be achieved (which again is important for measurements with high temporal resolution). Because laser light is parallel, a light sheet can easily be formed by combining a spherical convex[2] and cylindrical concave lens[3]. Depending on the lens types and their focal lengths, a broad range of different light sheet shapes can be created. In the present case, the laser light was guided by a light arm, which is a special tubing with implemented mirrors. The fluorescent volume was imaged by a long distance objective[4] and the fluorescent signal was extracted from the laser light by means of a longpass filter[5]. To point out the applicability of the measurement method for high speed measurements, a CMOS high speed camera[6] is employed for image capturing. Because the laser is pulsed, the laser and the camera must be synchronized, which is done by a synchronizer[7] and controlling software[8].

Comparable to the LCT measurements in the convection cube, the camera axis is perpendicular to the light sheet and the light propagation direction is vertical through the convection cube (see figure 5.1).

5.1.2 Experimental Procedure

The temperature measurements in the convection cube are conducted with deionized water as a solvent and Rhodamine B (RhB) as fluorescent dye. Because of its distinctive temperature sensitivity ($\approx 2\,\%/\mathrm{K}$), RhB is also used by many authors for temperature field measurements in water or ethanol (e.g. [24, 123, 124, 128]). Preliminary tests have shown that a RhB mass-volume-concentration of $2\,\mathrm{mg/l}$ in water offers a good fluorescence signal and therefore a good signal to noise ratio on the one hand and a negligible fluorescence intensity decrease due to absorbtion along the optical path on the other hand.

---

[1] Lee Laser Inc., Series 800, 2 x 14 mJ/pulse at 1000 Hz

[2] Two spherical lenses were employed with a total focal length of $f = 333\,\mathrm{mm}$

[3] $f = -100\,\mathrm{mm}$

[4] Leica Z16 APO, Lens: Planapo 1.0x, camera tube: 1.0x, Leica Microsystems GmbH Wetzlar

[5] Transmission of $\lambda > 540$ nm

[6] PCO, Powerview HS-650, 1024 x 1280 pixels, 10 bit, 650 fps at full resolution

[7] Laser Pulse Synchronizer Model 610035

[8] TSI Inc., Insight 3G

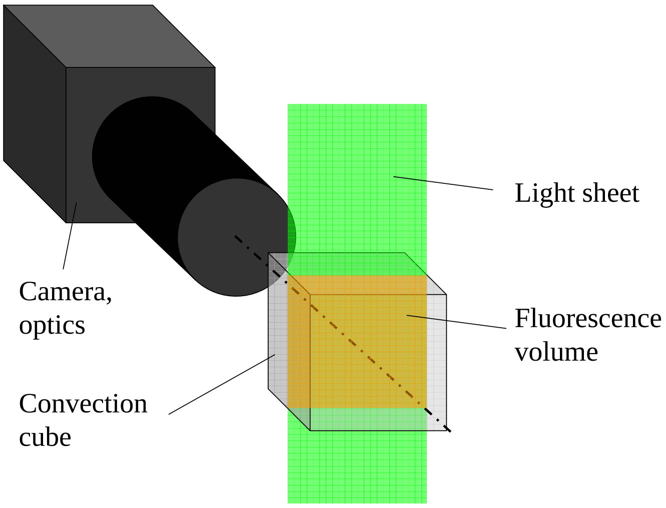

Figure 5.1: Schematic illustration of the measurement setup for 1C-LIF

Before the measurements, the air gases in water (N_2, O_2, CO_2) are for the most part removed by heating in an ultra sonic bath. This is done to prevent bubble formation during the measurements.

To allocate the fluorescence intensities to temperatures, a calibration needs to be carried out, which is done in-situ under measurement conditions. This is especially of concern to optical setup, since the lightsheet intensity is strongly inhomogeneous which is due to several reasons. Only with an unchanged measurement setup local calibration procedures and intensity field normalization can be applied as described in section 5.1.3. The light sheet was adjusted and the image capturing optics were focused on the light sheet. During the calibration procedure, the temperature of the two vertical opposite walls was kept homogeneously by using two bath thermostats[9]. Thus, the wall temperatures can be adjusted quite precisely with an accuracy of ±0.05 K. In most cases, a temperature range of 20 K is calibrated by measuring successively with a step size of 2 K. Before every measurement, the temperature is kept constant for 15 min, so that an almost homogeneous temperature distribution can be assumed.

Generally three different kind of measurements are conducted to characterize the 1C-LIF method.

First, an almost homogeneous temperature distribution in the liquid volume is realized with the background to figure out how accurate homogeneous tempera-

---

[9] Huber Ministat 125

ture distribution can be measured. The measurement accuracy is quantified by determining the standard deviation of the intensity values. Further, a stratified temperature distribution is achieved by adjusting a hot wall on the top and a cold wall at the bottom. The measured, stratified temperature distribution can be easily compared to analytically calculated one. Finally, a temperature field of free convection, induced by two tempered opposite vertical walls, is measured and the result is compared to a numerically calculated temperature field.

5.1.3 Image Analysis

The principle to obtain local temperatures from measured fluorescence intensity is conceivably simple - with the calibration curve, the fluorescence intensity is directly transformed into temperature values. To reduce measurement errors, several image processing algorithms can be applied which are explained as follows.

Pre-Processing

Some digital cameras exhibit the feature dark image subtraction whereby the dark noise is minimized. If the utilized camera does not provide this feature, the dark noise needs to be subtracted manually. Therefore a dark image is captured under conditions, where no illumination takes place, which is then subtracted from every image. To filter out white noise which is mainly caused by photon noise in image capturing, the images can be temporally or spatially averaged. This is done by local averaging (high frequencies are removed) or, respectively, by forming the arithmetic average from several images.

Processing

Two possibilities to minimize the influence of low frequency spatial noise, are local calibration or image normalization. The sources for low frequency spatial noise are mainly inhomogeneous illumination caused by the Gaussian intensity distribution of the beam, reflections, disturbances in the optical path and Lambert-Beer intensity attenuation due to absorption.

When doing local calibration, calibration curves for every pixel or at least for small areas exist. The temperature is then calculated depending on the local position. Another possibility to reduce low frequency spatial noise is the normalization.

Therefore, the measured image is divided by a characteristic image, I_0, resulting in $I_{norm} = I/I_0$. The characteristic image normally represents the highest fluorescence intensity, which equals the lowest measurement temperature. Many authors use 20 °C when doing measurements above room temperature. It is obvious that neither the FOV nor the illumination must change after the calibration or during the measurement. The different calibration methods are compared regarding their measurement accuracy in chapter 6.3.

Post-Processing

The subject of post-processing is to sort out erroneous values. Compared to LCT, erroneous temperature values caused by calibration procedures are less numerous, since the calibration curves are nearly linear. The post-processing then constricts to smoothing the temperature fields by local and/or temporal averaging.

5.2 Spectral Investigation

In literature, most 2C2D-LIF measurements are conducted with RhB and Rh110 (Rhodamine 110) excited by an Argon Laser (488 nm). For measurements with high temporal resolution, the use of a Nd:YAG laser is advantageous, since pulses with high intensity can be generated. Nevertheless, Rh110 is not excitable with a Nd:YAG laser because its absorption spectrum is too far in the shorter wavelength region. Therefore, another dye constellation needs to be found which fits to the exciting wavelength of an Nd:YAG laser and whose emission spectra are well defined and separable with the according optics. Natrajan and Christensen [94] applied RhB and Sulforhodamine 101, dissolved in ethanol. However, the maxima of the spectra of RhB and Sulforhodamine 101 in ethanol are very close to each other and therefore not clearly separable. Therefore, they captured a spectral part of Sulforhodamine 101 which is far from the emission spectrum of RhB but shows only little fluorescence intensity.

As explained in section 2.3.1, the most elegant method for 2C-LIF is 2C1D-LIF, where only one dye is used, which exhibits a wavelength dependent temperature sensitivity. To the author's knowledge, the only 2C1D-LIF planar measurements were done by Bruchhausen et al. [17]. By solubilizing RhB in water and applying a frequency doubled Nd:YAG laser (532 nm), they found a lower temperature sensitivity at smaller wavelengths of the fluorescence spectrum. With two interference filters, they captured the intensities of two small wavelength bands of 10 nm. For unknown reasons, these measurements were not repeatable in the own laboratories.

The aim of the spectral investigation is to find a dye which shows wavelength dependent temperature sensitivity for 2C1C-LIF and a combination of two dyes, suitable for 2C2D-LIF. On this account, the following demands on the dyes arose:

- Soluble in water and/or ethanol
- Excitable with frequency doubled Nd:YAG laser (532 nm)
- Emission maxima between 550 nm and 700 nm[10]
- Significant temperature sensitivity respectively insensitivity
- Low susceptibility for photobleaching effects

5.2.1 Experimental Procedure

To resolve the emission spectra of the specific dye, a spectrometer[11] was used. The test liquid (water or ethanol) was filled with the dissolved fluorescence dye into the convection cube and the fluorescent light was imaged with the long distance objective[12]. The whole measurement procedure is described in detail in [138]. A monochrome CMOS camera[13] was employed, because its relatively wide sensor chip and, according to this, a broad spectrum ($520 - 670\,\text{nm}$) with a spectral resolution of 2.5 nm could be imaged. To achieve information about the temperature sensitivity, the measurement procedure is quite similar to the calibration procedure; different temperatures are set and the emission spectra are measured. The temperature sensitivity is determined by approximating a linear function through every single wavelength value and can be expressed as

$$\zeta(\lambda) = \frac{\Delta I(\lambda)}{\Delta T} \cdot \frac{1}{I_0} \cdot 100\,\%. \tag{5.1}$$

---

[10] The lower maximum is limited by the longpass filter, which blocks the laser light and the upper maximum is limited by the camera

[11] Triax 320

[12] Leica Z16, 1.0x objective

[13] HS 650, PCO

To normalize the fluorescence intensity, it is divided by the characteristic fluorescence intensity I_0, which corresponds to the fluorescence intensity at 20 °C.

A possibility to compare fluorescence characteristics of different dyes regarding their emitted fluorescence intensities is to generate a relative fluorescence intensity. In the present case relative fluorescence intensity is defined as the fluorescence intensity of the particular dye referred to the fluorescence intensity of RhB in water at a concentration of $C_{mv} = 2\,\mathrm{mg/l}$ and at $T = 20\,^{\circ}\mathrm{C}$. If the concentration or illumination of the particular dye is different from the reference dye, equation 2.8 is used to modulate the values. Of course this procedure will not lead to an accurate result, but it will give an idea of the fluorescence intensity of the particular dye. Table 5.1 shows the results of the spectral investigations, which includes the wavelength of the emission maxima, $\lambda_{em,max}$, the maximum temperature sensitivity, ζ_{max}, the concentration used for the spectral investigation, C_{mv}, and the relative fluorescence intensity, I_{rel}.

An investigated dye, which suites for 2C1D-LIF, in respect to the excitation wavelength of 532 nm, is Pyridine 1[14]. Pyridine 1 is only soluble in ethanol and has its emission maximum at $\lambda_{max} = 670\,\mathrm{nm}$. The temperature sensitivity is, compared to other dyes, distinctive and approximately $\zeta = 2\%/\mathrm{K}$. Figure 5.2 shows the emission spectra of Pyridine 1. A broad range of high temperature sensibility can be found between 640 and 670 nm, while the range of low temperature sensitivity is between 550 and 590 nm. Pyridine 1 is photo stable, which means that only little photobleaching effects occur at intense illumination. Nevertheless, employing Pyridine 1 also has disadvantages, which are a low photon absorption coefficient at 532 nm and poor solubility in water.

As already mentioned, when 2C2D-LIF is applied, the maxima of the sensitive dye and reference dye should have a certain spectral shift, which is important for separating the spectra. A large spectral shift offers the combination of Pyridine 1 as sensitive and Rh6G as reference dye. Due to its weak absorption coefficient, the concentration of Pyridine 1 needs to be 20 times higher than the concentration of Rh6G. The spectra of Pyridine 1 and Rh6G in ethanol are shown in figure 5.3. A detailed description of the spectra of the investigated dyes concerning their temperature dependent spectra can be found in [138]. Furthermore [138] discusses the measurement accuracy of the spectral measurements.

---

[14] LDS 698, Radiant Dyes Laser Accessories GmbH, Wermelskirchen

Dye	Solvent: ethanol	Solvent: water
Rhodamine B	$\lambda_{em,max} \approx 570\,\mathrm{nm}$ $\zeta_{max} \approx -1\,\%/\mathrm{K}$ $C_{mv} \approx 2\,\mathrm{mg/l}$ $I_{rel} \approx 2.9$	$\lambda_{em,max} \approx 580\,\mathrm{nm}$ $\zeta_{max} \approx -2.5\,\%/\mathrm{K}$ $C_{mv} \approx \mathrm{mg/l}$ $I_{rel} \approx 1$
Fluorescein 27	not measured because poorly excitable	$\lambda_{em,max} \approx 555\,\mathrm{nm}$ $\zeta_{max} \approx 4\,\%/K$ $C_{mv} \approx 40\,\mathrm{mg/l}$ $I_{rel} \approx 0.005$
Sulforhodamine B **(Kiton Red)**	$\lambda_{em,max} \approx 580\,\mathrm{nm}$ $\zeta_{max} \approx -1\%/K$ $C_{mv} \approx 2\,\mathrm{mg/l}$ $I_{rel} \approx 2.1$	$\lambda_{em,max} \approx 590\,\mathrm{nm}$ $\zeta_{max} \approx -2.5\,\%/K$ $C_{mv} \approx 2\,\mathrm{mg/l}$ $I_{rel} \approx 0.5$
DCM	$\lambda_{em,max} \approx 570\,\mathrm{nm}$ $\zeta_{max} \approx -1\,\%/\mathrm{K}$ $C_{mv} \approx 2.5\,\mathrm{mg/l}$ $I_{rel} \approx 0.4$	not soluble
Rhodamine 6G	$\lambda_{em,max} \approx 560\,\mathrm{nm}$ not sensitive $C_{mv} \approx 2\,\mathrm{mg/l}$ $I_{rel} \approx 5.3$	$\lambda_{em,max} \approx 560\,\mathrm{nm}$ not sensitive $C_{mv} \approx 1\,\mathrm{mg/l}$ $I_{rel} \approx 5.2$
Sulforhodamine 101 **(Sulforhodamine 640)** **(Texas Red)**	$\lambda_{em,max} \approx 595\,\mathrm{nm}$ not sensitive $C_{mv} =\approx 4\,\mathrm{mg/l}$ $I_{rel} =\approx 1.4$	$\lambda_{em,max} \approx 610\,\mathrm{nm}$ not sensitive $C_{mv} =\approx 4\,\mathrm{mg/l}$ $I_{rel} =\approx 1.4$
Rhodamine 19	$\lambda_{em,max} \approx 555\,\mathrm{nm}$ not sensitive $C_{mv} \approx 10\,\mathrm{mg/l}$ $I_{rel} \approx 1.6$	poorly soluble
Pyridine 1 **(LDS 698)**	$\lambda_{em,max} \approx 670\,\mathrm{nm}$ $\zeta_{max} \approx -2\,\%/\mathrm{K}$ $C_{mv} \approx 20\,\mathrm{mg/l}$ $I_{rel} \approx 0.06$	poorly soluble

Table 5.1: Fluorescence properties of different dyes

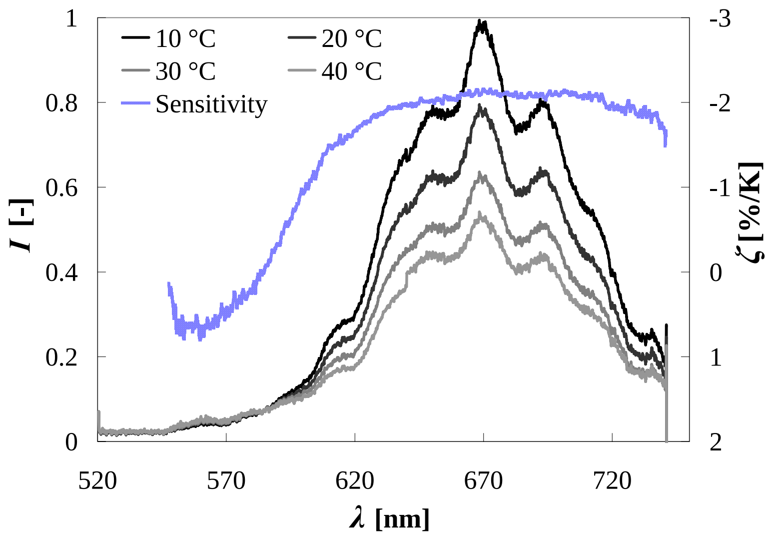

Figure 5.2: Emission spectra of Pyridine 1 in ethanol depending on temperature. Wavelength dependent temperature sensitivity is recognizable

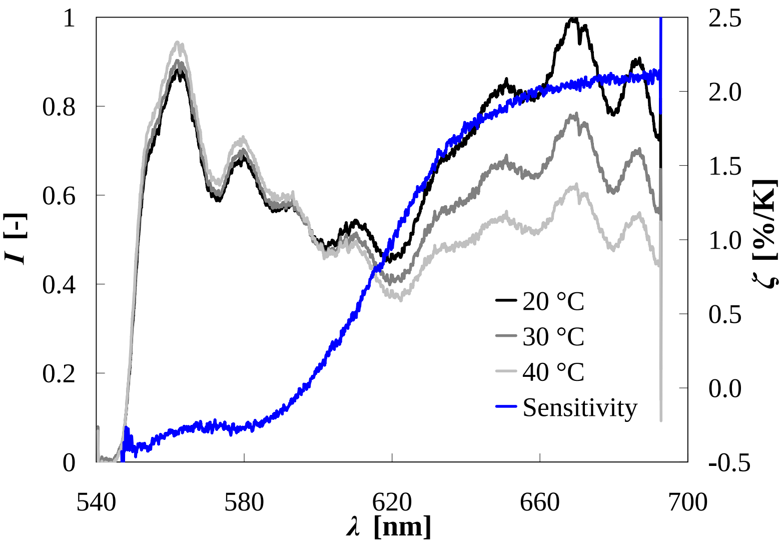

Figure 5.3: Emission spectra of Pyridine 1 and Rh 6G in ethanol. The non sensitive and the sensitive part can be separated easily

5.3 Two Color LIF

Based on the emission spectra obtained from the spectral investigation, the optical setup for the two color LIF can be designed and is described in the following section. The description of the illumination system and the image capturing is the same as for 1C-LIF, given in section 5.1.

5.3.1 Experimental Setup

As can be seen in figures 5.3 and 5.2, both spectra can be divided into a sensitive and insensitive part at a wavelength of 590 nm. On this account, the optical setup, which is shown in figure 5.4, was designed and is described in this section. The incident light consists of laser light and fluorescent light. The part of the laser light is blocked by the longpass filter, which transmits light with $\lambda_{t,LP} > 540\,\text{nm}$ and is located in front of the microscope objective[15]. The transmitted fluorescent light is then separated by a dichroic mirror, which reflects light with $\lambda_{r,M} < 585\,\text{nm}$ and transmits light ($t > 0.9$, t is the transmission coefficient) with $\lambda_{t,M} > 605\,\text{nm}$. Nevertheless, the dichroic mirror also reflects a certain part of the lower wavelength spectrum, which demands an additional shortpass filter in front of the low wavelength sensor. The used shortpass filter transmits wavelengths with $\lambda_{t,SP} > 585\,\text{nm}$ and blocks higher wavelengths with $t_{\lambda>605} < 10^{-5}$. Figure 5.5 shows the wavelength dependent temperature sensitivities and the captured spectral bands depending on the applied optics. The images were recorded by using two CMOS cameras[16] which allow high speed capturing up to a rate of 600 frames per second.

5.3.2 Experimental Procedure

The experimental procedure and the image analysis is in many parts similar to the discussed experimental procedure of 1C-LIF (section 5.1). Of course, different complexity arises due to the alignment of the optical setup and the extraction of the temperature information out of two images. Because it is not possible to precisely adjust the optical setup in a way that both cameras capture exactly the

---

[15] Leica Z16 Apo, 1.0 X

[16] HS650 PCO, Photron Fastam 512

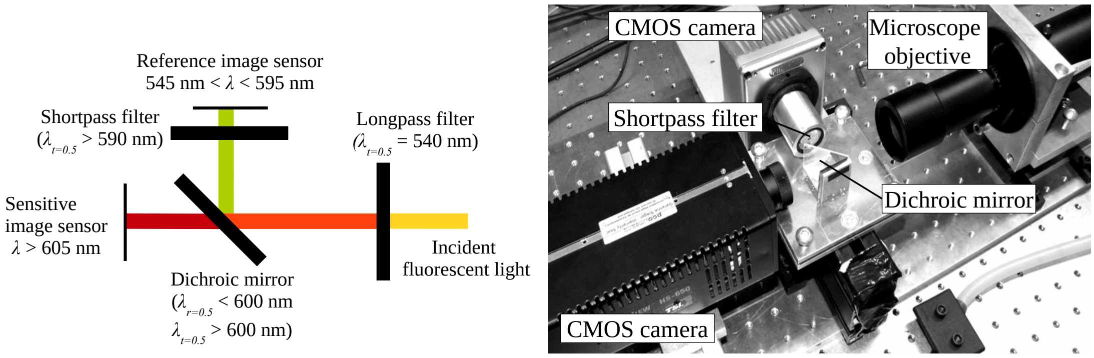

Figure 5.4: Optical setup to separate the emission spectra. Schematic sketch on the left side and photo of the setup on the right side

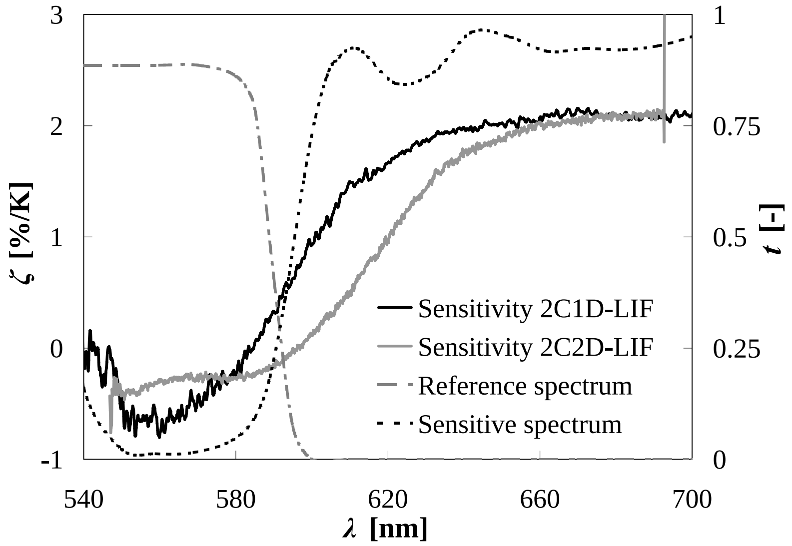

Figure 5.5: The dashed lines represent the spectral parts, which are transmitted to the cameras. As noticeable from temperature sensitivity curves, the two spectral parts capture a temperature sensitive signal and a reference signal. The temperature sensitivity curves are shown for Pyridine 1 (2C1D-LIF) and the constellation of Rh6G and Pyridine 1 (2C2D-LIF)

same FOV, image algorithms need to be applied to correct this variation. Therefore, the images are resized, superimposed and, if necessary, dewarped and rotated. On this account, a test grid is recorded after the adjustment of the objective and the cameras.

After subtracting the dark images, the ratio between the sensitive and the reference image is generated by

$$R = \frac{I_{sens}}{I_{ref}}. \tag{5.2}$$

Comparable to the 1C-LIF image analysis, local calibration,

$$R(i,j) = \frac{I_{sens,i,j}}{I_{ref,i,j}} \tag{5.3}$$

or normalization

$$R_{norm} = \frac{I_{sens}/I_{sens,0}}{I_{ref}/I_{ref,0}} \tag{5.4}$$

procedures can be applied. The influences of the different image analysis is presented in chapter 6.3.

Chapter 6

Experimental Characterization and Deployment

In the following, the results of the LIF measurements are presented. These consist of results of 1C-LIF (6.1) and 2C-LIF (6.1). Furthermore, error sources are pointed out and the possibility to minimize these error sources applying 2C-LIF is shown. At the end of this chapter, the achieved measurement accuracies of the different LIF techniques are presented. The measurements were performed in the convection cube described in section 4.6.

6.1 Measurement Accuracy of 1C-LIF

The topic of this section is the discussion of the applicability of 1C-LIF for temperature measurements in liquids and of the error sources of the LIF measurement technique. Therefore, measurements of different temperature fields are presented. A mass-volume-concentration of 2 mg/l RhB was dissolved in water and all temperature fields presented in this section were evaluated with local calibration procedures.

6.1.1 Homogeneous Temperature Distribution

Contrary to the LCT method, the measurement uncertainty is not dependent on an activity range. The measurement uncertainty can be considered as absolute instead. To determine the measurement accuracy, homogeneous temperature fields were measured employing the convection cube. The standard deviation of an image with its size m by n pixels is calculated from

$$\sigma_T = \sqrt{\frac{1}{m \cdot n} \sum_{i}^{m \cdot n} (T_i - T_{TC})^2}, \tag{6.1}$$

where T_{TC} is the temperature measured by the thermocouples and is seen as a set point temperature. An overview of the standard deviation depending on the spatial and temporal averaging is given in figure 6.1. Temporal averaging was conducted by generating the arithmetic mean of a certain amount of images and spatial averaging by applying an averaging box filter with a certain size. It is obvious that the standard deviation decreases with an increasing number of averaged images. After a certain number of averaged images, the standard deviation shows an asymptotic behavior which is rooted in spatial noise. Further decreasing the uncertainty is only possible by spatial averaging. Depending on the application, the spatial and temporal averaging should be chosen in a reasonable matter.

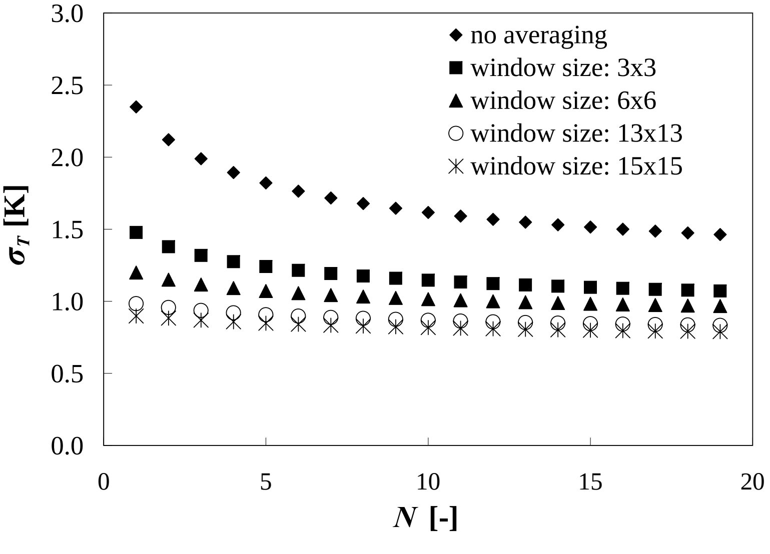

Figure 6.1: Standard deviation of homogeneous temperature distribution measurement in dependency on the averaging window size plotted against the number of averaged images

6.1.2 Stratified Temperature Layer

When the top wall of the facility has a higher temperature than the bottom wall while all other walls are adiabatic, a stratified temperature distribution forms. Because the temperature distribution is linear in vertical direction, y, the measurement accuracy can be investigated easily. Figure 6.2 shows the measured temperature along the y-axis, the analytical temperature and the deviation between the two temperatures, ΔT. The values are averaged over 10 pixels in horizontal (x) direction.

It can be seen from figure 6.2 that the stochastic error is around $\pm 2\,\mathrm{K}$, while a systematic error is assumed near the colder wall, which is around 4 K (e.g. due to reflections or shadows). The high frequency noise is mainly caused by stripes in the light sheet which are induced by the surface roughness of the PMMA wall. A material like glass would lead to better results. The presented stratified temperature distribution is one out of several measurements which all show similar behavior. Reasons might be effects of refraction due to high temperature differences or the erroneous wall temperature measurement. Because it is not possible to directly measure the temperature at the wall, it is measured inside the wall and extrapolated, which again causes additional errors.

6.1.3 Thermally Induced Free Convection

Thermally induced free convection is caused by temperature dependent density differences. When one vertical side wall has a higher temperature than the others, a circulating flow arises. To obtain a reference temperature field, numerical calculations are performed as described in section 4.6. The measured temperature field is exclusively temporally averaged over 10 images which results in a high spatial resolution of $75\,x\,75\,\mu\mathrm{m/pixel}$. Both the calculated and measured temperature fields are shown in figure 6.3, and a good agreement is noticeable. The high temperature gradients near the vertical side walls in particular are resolved fairly well. The aforementioned stripes can be seen in the measured temperature field which again makes clear that the transparent side walls need to have good optical properties.

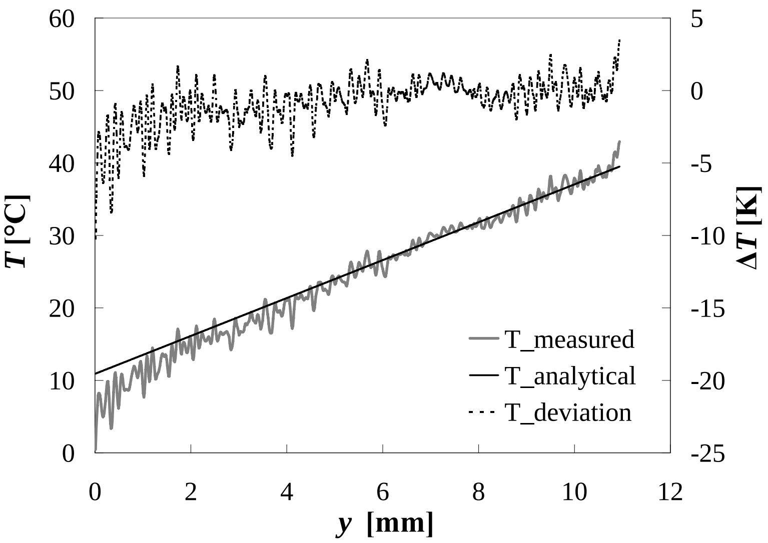

Figure 6.2: Analytically and experimentally determined temperature distributions of stratified temperature layers. The y-direction is contrary to the gravity direction. Further the difference between the calculated and measured temperature is shown.

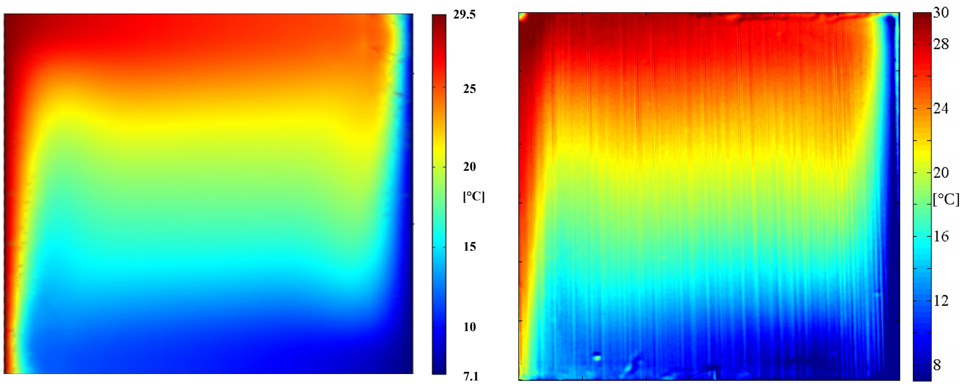

Figure 6.3: Temperature field of thermally induced free convection in a cube with side length of 12 mm. Left: numerically simulated, right: measured temperature field. RhB in water was used for 1C-LIF

6.1.4 Error Sources

Assuming that the pH-value of the liquid and the air gas concentration do not change during the measurement, the remaining factors which affect the measurement accuracy are the dye concentration, image capturing and illumination.

The error sources in particular, which lead to inhomogeneity and fluctuations of the illumination, are multifarious and have a significant influence on the measurement signal.

Additional errors arise when two phase flows with changing interfaces are conducted. At interfaces between liquid and gas, the refractive index changes strongly.

The resulting measurement errors show different spatial and temporal frequencies and can be divided into spatial and temporal errors. One kind of error sources mainly influences the temporal devolution (e.g. fluctuations in laser pulse energy) while others have their main influence in the spatial distribution (e.g. different sensitivities of pixel sensors, inhomogeneous laser light distribution, reflections at interfaces, refraction effects) and some influence both (e.g. photon noise, inhomogeneous dye concentration). The influence of the spatial and temporal noise on the measurement accuracy can be directly seen in figure 6.1. The asymptotic behavior of the measurement uncertainty over the number of averaged images indicates that spatial noise exists, which cannot be minimized by temporal averaging. Similarly, the measurement uncertainty will show an asymptotic behavior over the averaging window size which is assigned to the temporal noise.

Table 6.1 shows the main error sources. It is nearly impossible to list all error sources and to quantify them. Most of the described error sources produce noise with a broad spectrum of frequencies and the listed frequencies are the most often observed ones. Nevertheless, table 6.1 can help to improve the measurement accuracy, when the measurement errors are identified and image analysis is applied.

Error source	Description	Temporal or spatial noise	Noise frequency
Dye concentration			
Solubility	Solubility of dye in test liquid is poor, → local concentration differences	Spatial	Low
Phase change	Phase change leads to local enhancement of concentration	Spatial (temporal)	Low
Illumination			
Laser pulse	Different energies of laser pulses	Temporal	High
Lightsheet inhomogeneity	Intensity distribution of lightsheet is Gaussian like	Spatial	Low
Shadowgraphy effects	refractive index of liquid is temperature dependent	Spatial temporal	Spatial: low-medium temporal: depends
Lightsheet disturbed	Caused e.g. by surface roughness of transparent walls	Spatial	Medium till high
Photobleaching	Caused by intense illumination	Spatial temporal	Low
Image capturing			
Digitalization	Depends on number of bits of camera, influence negligible for for cameras with high bit number	- -	- -
Photon noise	Number of photons hitting the pixel sensor is stochastic, especially for signal intensity	Spatial temporal	High
Pixel sensor inhomogeneities	Sensitivity of pixel sensors is not homogeneous	Spatial	High
Amplifiers	Noise is also amplified, amplification often not linear	Spatial temporal	
Others			
Optical way	Length of optical way changes (e.g. two phase flows)	Spatial temporal	Spatial: low temporal: depends
Moving interfaces	Leads to reflections and diffractions (especially at two phase flows)	Spatial temporal	Spatial: medium till high temporal: depends

Table 6.1: Error sources of 1C-LIF

6.2 Two-Color LIF for Enhancement of Measurement Accuracy

As shown in table 6.1, the illumination plays a significant role for the total measurement error. The 2C-LIF technique is a possibility to minimize the influence of illumination as clarified by equation 2.9 and 2.10. On this account, different investigations concerning the applicability of 2C-LIF were conducted and are presented in the following section.

6.2.1 2C1D-LIF

Principally, the 2C1D-LIF technique is the best method regarding its independency on concentration and illumination influences. Nevertheless, Pyridine 1, appropriated for 2C1D-LIF, shows very little fluorescence intensity in the spectral region for the reference image (figure 5.2). The same effect can be seen in the spectrum for RhB when it is excited with an argon-ion laser ($\lambda = 514.5\,\mathrm{nm}$) [75, 17]. The spectral region which comprises low temperature sensitivity shows very low fluorescence intensity. This fact excludes the applicability of the 2C1D-LIF method from measurements with high spatial and temporal resolution. An increase of the dye concentration is problematic due to self-absorption effects and significant decrease of the illumination intensity described by Beer-Lambert law (equation 2.7). On this account, further investigations of the 2C1D-LIF technique were not performed.

6.2.2 2C2D-LIF

When applying RhB and Pyridine 1 with a Nd:YAG laser, distinctive fluorescence intensities can be achieved, which principally enables high resolution measurements. To achieve comparable fluorescence intensities, the ratio between the mass-volume-concentrations of Pyridine 1 and Rh6G was chosen 66.7 : 1.

Influence of Dye Concentration

In figure 6.4 the influence of the concentration on the temperature dependency of the ratio is shown. The default concentration of Rh6G and Pyridine 1 is composed

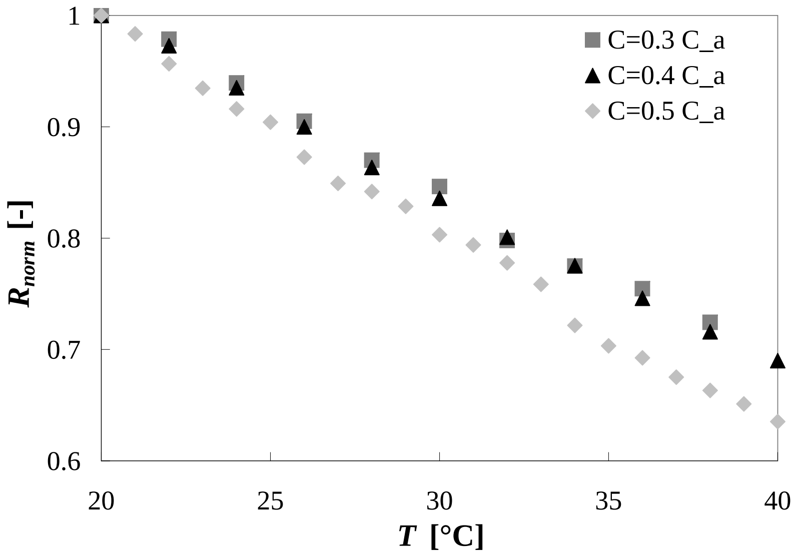

Figure 6.4: Influence of concentration on the normalized ratio

from the mass-volume-concentrations $C_a = C_{Rh6G} + C_{Pyr}$ with $C_{Pyr} = 20\,\mathrm{mg/l}$ and $C_{Rh6G} = 0.3\,\mathrm{mg/l}$. Ideally the normalized intensity is not dependent on the concentration of the dyes in the liquid as long as the ratio between the dyes is constant. This behavior can be seen for the concentrations of $C = 0.3 \cdot C_a$ and $C = 0.4 \cdot C_a$. The temperature dependency of $C = 0.5 \cdot C_a$ instead differs significantly from the others. The reason therefore might be different air gas concentrations or others because the measurement was performed the following day. It becomes apparent that an in-situ calibration before the actual measurement is necessary.

Influence of Illumination Intensity

The influence of the illumination intensity on the ratio was observed in changing the pulse energy of the laser. Therefore, a homogeneous temperature field was measured with different dye concentrations. As it was not possible to adjust the illumination intensity of the laser exactly, the intensity of the temperature sensitive spectrum and the ratio of both images is plotted over the intensity of the reference image.

It can be seen in figure 6.5 that the ratio is not independent of the illumination intensity, which is attributed to the nonlinearity of the cameras. Further, a dependency on the concentration is not recognizable. This allows the introduction of a

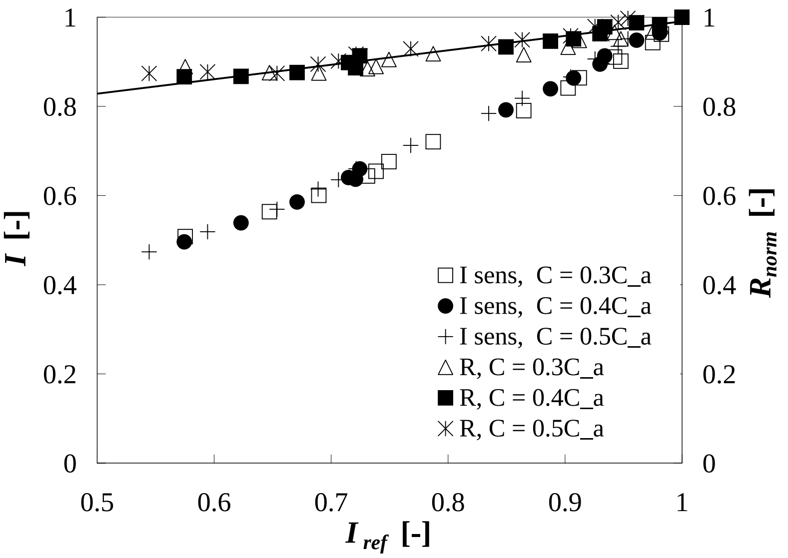

Figure 6.5: Ratios between sensitive and reference images over illumination intensity for different concentrations

correction factor k to minimize the dependency of the ratio on the illumination intensity.

$$R_{corrected} = R_{norm} + k \cdot I_{ref} \tag{6.2}$$

The assumption of nonlinear cameras is affirmed when examining the ratio between the reference and temperature sensitive part obtained by one camera. The ratio is created by dividing the sensitive through the reference spectral part achieved from the spectral investigations of the dyes (chapter 5.2). As can be seen in figure 6.6, the ratio is nearly constant.

Example for Accuracy Enhancement through Employing 2C2D-LIF

In this section, a disruption of the illumination is simulated by putting a scratched glass plate between the lightsheet and the transparent wall. As a result, spatial inhomogeneities in the illumination intensity occur in form of stripes (figure 6.7). Figure 6.8 shows the normalized intensity profiles along a line in x-direction. The intensity distribution is filtered by a window of 2 pixel in $x-$direction and 5 pixel in $y-$direction. When looking at the temperature distributions in figure 6.8, the advantage of the 2C2D-LIF method becomes apparent. The (69 %) standard deviation for 2C2D-LIF using the correction factor (equation 6.2) is seven times

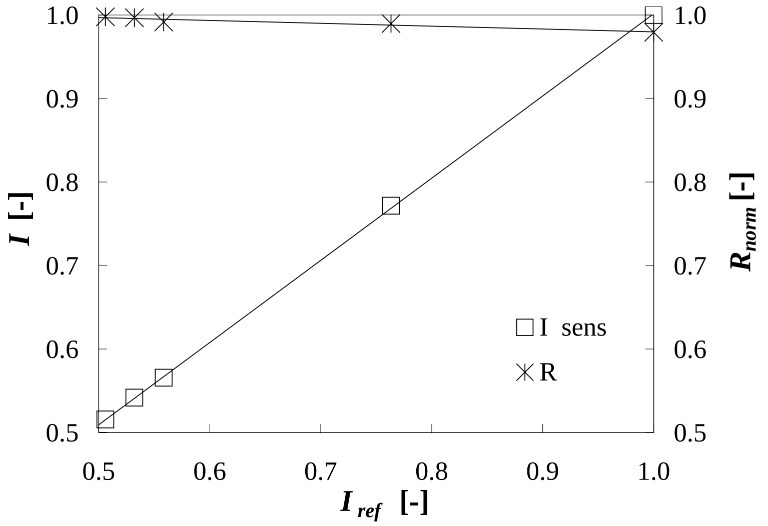

Figure 6.6: Ratios of sensitive and reference spectral parts for Pyridine 1 and Rh6G over illumination intensity

smaller than for 1C-LIF. Even better results can be expected for 2C2D-LIF with better cameras.

6.3 Resume

In table 6.2, an attempt to quantify the measurement method concerning their measurement accuracy is presented. Therefore, the standard deviations for different methods of image analysis (normalization and local/global calibration) are

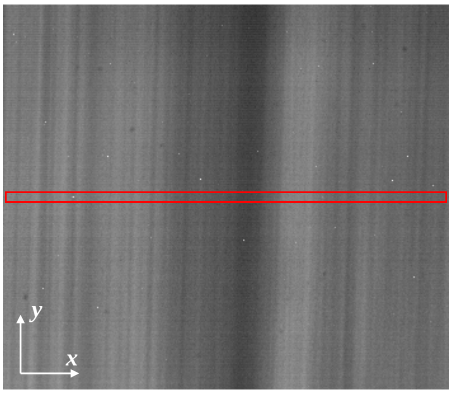

Figure 6.7: Stripes in the lightsheet caused by a scratched glass plate within the optical way

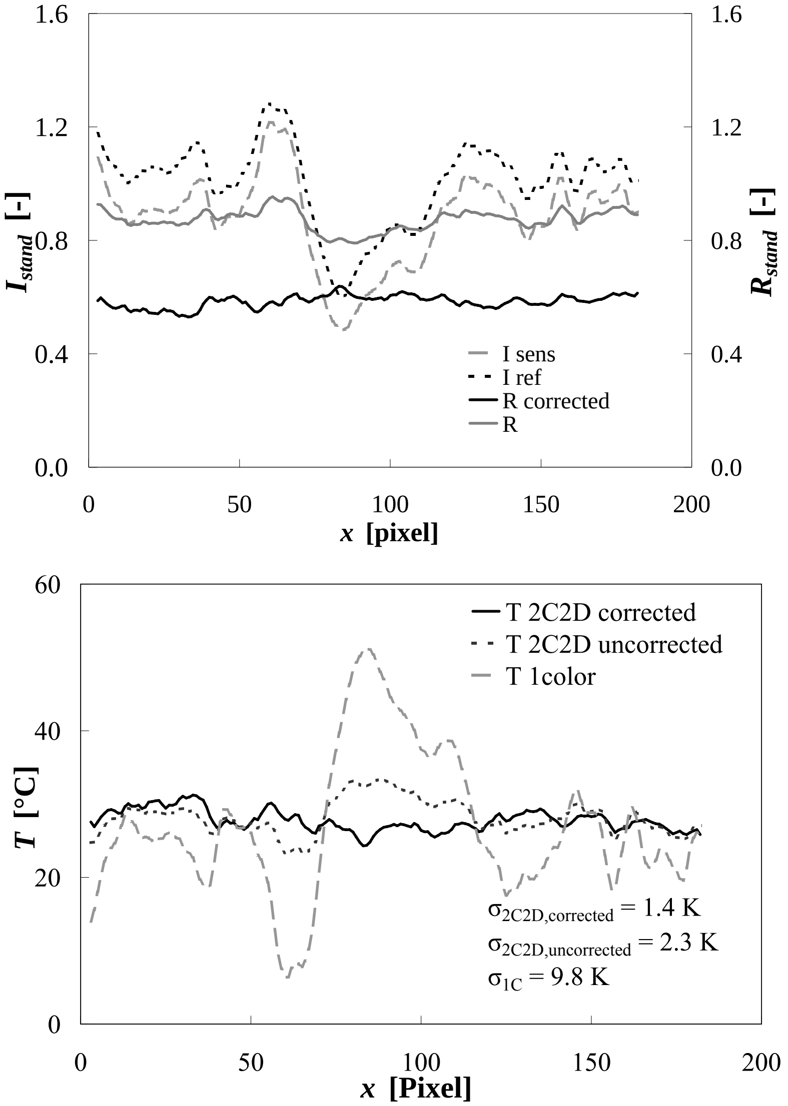

Figure 6.8: Intensity and ratio profiles along x-direction for the image with stripes in laser light sheet. Temperature profiles are calculated with different analysis methods. The minimization of measurement error becomes significant for 2C2D-LIF

presented. Further the image analysis methods have been applied for 1C- and 2C2D-LIF which results in eight different possibilities. While the temperature fields are averaged over 200 images in time, no spatial averaging was conducted. In regards of comparability, the different LIF techniques were applied on the same images.

	Local calibration		Global calibration	
With normalization	1C-LIF:	$\sigma_T = 1.72$ K	1C-LIF:	$\sigma_T = 0.94$ K
	2C2D-LIF:	$\sigma_T = 1.14$ K	2C2D-LIF:	$\sigma_T = 0.87$ K
Without normalization	1C-LIF:	$\sigma_T = 0.73$ K	1C-LIF:	$\sigma_T = 12.26$ K
	2C2D-LIF:	$\sigma_T = 0.57$ K	2C2D-LIF:	$\sigma_T = 2.95$ K

Table 6.2: Standard deviation for measurements of homogeneous temperature distributions for 1C-LIF and 2C2D-LIF using different image analysis methods

It is obvious that 1C-LIF with global calibration procedures and without normalization leads to a significant temperature measurement error. This error is mainly due the inhomogeneous illumination intensity distribution and can be decreased with local calibration or normalization. Applying both methods, normalization and local calibration again leads to a worse result. The reason therefore is error propagation due to multiplying defective factors. The best result is obtained by 2C2D-LIF method combined with local calibration.

It can be concluded that 1C-LIF works adequately for one-phase flows which are static and allow temporal averaging. Further, the concentration of the dyes must not change. Because the whole setup and the data analysis are, compared to 2C-LIF, less complex, 1C-LIF should be preferred under these circumstances. For two-phase flows or spatially and temporally changing illumination properties, 2C-LIF needs to be applied.

Due to the weak fluorescence intensity of the reference signal, it was not possible to accomplish measurements with high spatial and temporal resolution with the

2C1D-LIF method employing Pyridine 1 as dye. However, the method can be applied for measurements which do not require high temporal resolution and therefore allow multiple pulses per image.

When employing Pyridine 1 and Rh6G, distinctive fluorescence signals are achieved, and thus measurements with high spatial and temporal resolution are possible.

Chapter 7

Comparison of LCT with LIF

In the following chapter, the measurement methods LCT and LIF are compared. The chapter is divided into the sections applicability (7.1), implementation (7.2), resolution (7.3) and accuracy (7.4).

7.1 Applicability

The measurement range of available TLCs is restricted and varies from 0.5 K to 40 K, while the start temperature lies between -30 °C and 120 °C. Fluorescence dyes show a broader spectrum of applicability that is often restricted by the boiling point of the fluid or the point, where thermal dissociation of the dye sets in. While the measurement accuracy of the LCT method is strongly dependent on the measurement range, the measurement accuracy of the LIF method mainly depends on the temperature sensitivity of the particular dye (up to 3%/K). On this account, the LIF method is preferred for measurements with higher temperature differences while the LCT method is able to resolve small temperature differences down to a few hundredth of Kelvin.

A further point, especially important for micro applications, is the illumination. Often light sheets cannot be generated and the whole measurement volume needs to be illuminated. Applying LIF results in a fluorescence of the whole liquid volume, which again makes real 2D temperature measurements impossible. To counter this problem, an expensive technique has to be applied like confocal microscopy, which in addition leads to a loss in the signal to noise ratio. Volume illumination however can be applied for LCT without restriction as shown in section 4.7. This is due to the fact that particles, which are within the focal depth, are recognized as particles and contribute to the temperature information.

Simultaneous measurements of temperature and velocity fields are possible, employing TLCs as tracer particles. When using LIF, further effort has to be made to obtain velocity fields simultaneously. For example, extra particles can be added and an additional camera needs to be employed to receive proper measurement accuracy.

7.2 Implementation

The implementation of the measurement method LCT is principally simple: a white light source and a RGB camera are needed. The measurement setup of the 2C-LIF becomes more complex because a second camera is required. Further, special optics like dichroic mirrors and filters need to be employed. The advantage of LIF is the possibility to use a monochromatic light source, like a laser. A laser combines on the one hand high irradiance and on the other hand good controllability of the laser light. It is nearly parallel and can be easily shaped, directed and controlled. Because white light is needed for LCT, one is restricted to thermal or luminescence light sources which exhibit a limited irradiance. Further, apertures and slits are necessary to generate a light sheet, which again leads to losses of the radiant flux.

Also the choice of the test liquid is restricted. When applying LCT, the density of test liquid should match that of the TLCs and the liquid needs to be chemically compatible with the capsule material of the TLCs. For LIF, the dye must be soluble in the liquid. Both methods show a dependency on the test liquid, which mainly leads to changes in the activity range (LCT) and the temperature sensitivity (LIF).

The complexity of the image processing of LCT depends on the application. If PIT is performed, the particles with the particular temperature information need to be detected first. This, and the need for proper averaging algorithms due to the high uncertainty, demand elaborate image processing algorithms. The image analysis of LIF is in principal simple and only gets elaborate, if two cameras are applied. Then the images need to be geometrically matched.

7.3 Resolution

It can be said that both, the spatial and temporal resolution of the LIF method, mainly depend on the measurement equipment. Due to the physical principle of LIF, the thermal response time is a few nanoseconds (fluorescence decay time) and the spatial resolution (size of molecules) is in the range of nanometers. The main restriction is an insufficient fluorescence signal intensity, conducting high temporal and spatial resolution measurements simultaneously. On this account, a higher sensitivity of the camera chip and a higher illumination intensity is demanded. Nevertheless, with the nowadays existing measurement equipment, temporal resolutions in the range of 1 kHz and spatial resolutions less than microns are conceivable.

For several reasons, neither the spatial nor the temporal resolution of the LCT method can be as high as for the LIF method. A crucial factor is the high uncertainty of the measurement method. This demands temporal or spatial averaging going along with a reduction of the particular resolution. Available encapsulated TLCs have a minimum diameter of 10 μm and therefore a maximum resolution of approximately 100 μm is possible. The main restriction of the temporal resolution are for certain the thermal response time which is about 10 ms and the need for temporal averaging, as presented in section 4.5.3. Measurements with both high temporal and spatial resolution are therefore not possible.

7.4 Accuracy

The LCT measurement method is depending on many measurement parameters, like light intensity, reflections and others. Therefore the calibration has to be conducted in-situ and the particular conditions must not change during the measurement. This again leads to a constricted applicability of the LCT method for temperature measurements in flows with phase change. In this case, moving interfaces lead to unwanted reflections and refractions. Applying the complex 2C-LIF method, the main influences like illumination intensity and concentration, are minimized and do not affect the result significantly. Nevertheless, an in-situ calibration is highly recommended. Beside that, effects like chemical or photo bleaching exist for 2C-LIF, which are neither reversible nor reducible. These effects can be compared to the TLC damage by ultra violet radiation, chemical effects or aging. Generally the LCT technique shows a much higher uncertainty which is up to ±20 % of the measurement range. Because the measurement uncertainty mainly occurs in form of white noise, temporal or spatial averaging can be applied to minimize the uncertainty. In the present work, uncertainties of $\pm 0.75\,K$ for 1C-LIF and $\pm 0.57\,K$ for 2C2D-LIF were achieved with temporal averaging over 200 images but without spatial averaging. Regarding section 6.1.2, temporal averaging over 20 images would lead to similar accuracy.

Concluding the main advantages and disadvantages of the measurement methods are presented in table 7.1.

	LCT	LIF
Measurement range	⊖ limited ($\Delta T = 0.5 - 40\text{K}$, $T_{RS} = -30 \cdots 120°\text{C}$) ⊕ small temperatures resolvable in range of hundredth K	⊕ broad temperature spectrum ⊖ absolute error of 0.57 K reduces resolution
Volume illumination	⊕ real 2D measurements possible due to depth of focus	⊖ real 2D measurements not possible, complex confocal microscopy is needed
Simultaneous velocity field measurements	⊕ easy to realize with PIV and TLC particles as tracers	⊖ additional effort is required
Measurement setup	⊕ simple	⊖ complex, when applying several cameras
Spatial resolution	⊖ 100 µm achieved, mainly limited by TLC diameter and required averaging	⊕ very high resolution in range of sub-microns possible, depending on measurement equipment
Temporal resolution	⊖ limited by thermal response time of TLCs (≈ 10 ms) and required averaging, 0.5 kHz possible	⊕ very high resolution possible, depending on measurement equipment, > kHz
Simultaneous high temporal and spatial resolution	⊖ not possible due to required averaging	⊕ possible
Additional effects	• UV light causes damage of TLCs • hysteresis effects after super-heating • aging of TLCs	• photo bleaching at extensive illumination • sensitive to pH-value
Uncertainty	⊖ 20 % from measurement range	⊕ absolute $0.5 - 1$ K

Table 7.1: Advantages and disadvantages of measurement techniques LCT and LIF

Chapter 8

Summary and Outlook

8.1 Summary

Microscale heat transfer mechanisms in liquids are very important for various applications. Whether these are nucleate boiling, evaporation of menisci or heat transfer enhancement through micro-structured surfaces, most of the mechanisms are not fully understood. The reason for this is that they yet cannot be described precisely by theoretical or numerical models, and the demand for experimental measurements becomes clear. While velocity field measurement techniques in micro scales have progressed rapidly in the last ten years and even three-dimensional velocity fields can be determined, the measurement of temperature fields is still not established. An additional complexity is caused by the fact that many heat transfer mechanisms are transient and furthermore highly dynamic, which requires a high temporal resolution of the measurement technique.

The two techniques, which are probate for temperature measurements in macro regions are liquid crystal thermography (LCT) and laser induced fluorescence (LIF). The attraction of the LCT technique is the possibility to simultaneously measure temperature and velocity fields because the encapsulated TLCs can be applied as tracer particles for temperature and velocity measurements. If LCT is applicable for high spatial and temporal resolution measurements, it was not clarified at this point, though. In principal, the LIF method can be applied for high spatial and temporal resolution measurements due to its physical principle. The size of fluorescence molecules is in region of nanometers and the fluorescence lifetime lasts only few nanoseconds.

On this account, the measurement methods LCT and LIF were characterized regarding their spatial and temporal resolutions and applicability. Moreover parameters which affect these measurement techniques were identified and possibilities to minimize the error sources were presented. As the analysis of the measurement data plays an important role in the enhancement of the measurement accuracy, it was investigated in detail and new processing methods were developed.

To determine the measurement accuracy of the LCT method, measurements of homogeneous temperature distributions and thermal induced convection were conducted. Therefore a cubic facility was constructed, which enables the adjustment of homogeneous wall temperature and homogeneous liquid temperatures. The measured temperature fields of a thermal induced convection flow were compared with numerically calculated ones. Based on these results and known results from literature, parameters were investigated which affect the measurement accuracy. Furthermore, volume illumination was employed with regard to the applicability of LCT for high spatial resolution measurements. The influence of the angle between the illumination and the camera axis was investigated and compared with results from literature. For volume illumination, similar results were found as for the common illumination technique, employing a light sheet. Due to diverse statements in literature concerning hysteresis effects caused by super-heating of the TLCs, adequate measurements were conducted. It was found, that hysteresis occurs but it does not depend on the grade of super-heating. Further, the hysteresis disappears, when the TLCs are cooled beyond the start temperature of the activity range. The main restriction of the temporal resolution is assumed in the thermal response time of the encapsulated TLCs. Therefore, measurement concerning the response characteristics of TLCs were performed. The TLCs were excited by sinusoidal and ramp-like temperature changes of the surrounding liquid and a thermal response of less than 10 ms at high frequencies respectively high temperature gradients was observed in both cases.

Because the LCT method shows extensive deviation in the temperature indication of the particular particles, careful data analysis is demanded. Algorithms like background subtraction and local temperature calibration were developed and applied in order to enhance the measurement. A further point is the strong dependency of the temporal resolution on the R, G, and B values of the camera.

On this account, an algorithm was developed to separately weight the *R*, *G* and *B* signals. By applying this algorithm, the measurement accuracy could be enhanced.

Volume illumination was employed for the first time in a channel flow, and it was shown that extraction of temperature fields by applying special image analysis methods is possible. Moreover the optical setup was extended and scanning of the channel flow was realized so that 3D temperature fields could be achieved.

Similar to the LCT method, the accuracy of the LIF method was investigated employing the cubic facility. Here the LIF technique shows very good results concerning the accuracy and spatial resolution. Nevertheless, the LIF technique exhibits a distinctive dependency on the dye concentration and the illumination. This dependency strongly decreases the applicability of the technique for two phase flows, since gas liquid interfaces lead to refraction and reflection effects which cause inhomogeneous illumination.

Two-color-LIF, which uses an additional reference signal, which does not depend on temperature is a probate method to overcome these problems. In principle, two methods exist which were both applied. Either an additional dye is employed for the reference signal (2C2D-LIF) or the reference signal is extracted from a dye which exhibits a wavelength dependent temperature sensitivity (2C1D-LIF). In both cases, the fluorescence spectrum bands need to be captured selectively with two sensors. Nevertheless, it was found that dyes used in literature for 2C-LIF are not appropriate for the use with a Nd:YAG laser. For this reason, spectral investigations on eight different dyes were conducted. As a result, Pyridine 1 was found as dye which offers the wavelength dependent temperature sensitivity and is suitable for 2C2D-LIF. The combination of Pyridine 1 and Rhodamine 6G shows all the required properties for 2C2D-LIF. The two fluorescence spectra have a certain distance between their fluorescence maxima and therefore are properly separable. Pyridine 1 shows a good temperature sensitivity while Rhodamine 6G is approximately temperature insensitive. Both dyes are soluble in ethanol and do not show high susceptibility to photobleaching. Although the exciting laser light wavelength does not coincidence with the maximum in the absorption spectra of Pyridine 1, the fluorescence signal quality is good when enhancing the concentration of Pyridin 1.

Based on the results of the spectral investigations, an optical setup was realized which enables the separation of the temperature sensitive and the reference signal.

Again the cubic facility was employed for determining the measurement accuracy and it was found, that the fluorescence intensity of Pyridine 1 is too low in the temperature insensitive spectral region. The 2C1D-LIF method using Pyridine 1 is therefore not applicable for high resolution measurements. In contrast, the combination of Pyridine 1 and Rhodamine 6G provided a good signal to noise ratio and therefore potential for high resolution measurements. Further, it was proved that the 2C2D-LIF method significantly reduce the influence of inhomogeneities in illumination.

When reckoning the TLC capsule diameter and the measurement uncertainty, the limitation in the spatial resolution of LCT becomes clear. The temporal resolution is limited by the thermal response time of the TLC capsules and the demand for temporal averaging. Considering these factors, it is obvious that measurements with simultaneous high spatial and temporal resolution are not possible. Nevertheless, due to the simplicity of the measurement setup and the possibility for simultaneous measurements of temperature and velocity fields, LCT is attractive for applications like static flows. A further advantage is the possibility to resolve small temperature differences of hundredth of Kelvin when applying TLCs with small measurement ranges. TLCs also offer an important advantage for applications in micro flows. Volume illumination can be applied instead of a light sheet and the temperature fields can be extracted by image algorithms from each particle within the focal depth.

The LIF technique exhibits the possibility of very high spatial and temporal resolution and the limitation is mainly caused by the optical equipment like the laser and the camera.

Further the basis for high temporal and spatial resolution measurements using 2C2D-LIF was established. Employing an Nd:YAG laser as a powerful illumination source in combination with Pyridine 1 and Rhodamine 6G enables high acquisition rates (up to 500 Hz with the employed equipment) and high spatial resolution.

8.2 Outlook

Liquid Crystal Thermography

In the first instance, the measurement accuracy of LCT needs to be enhanced. A better measurement quality in combination with higher temporal and spatial resolutions of the LCT technique could be achieved, if cameras with higher sensibilities were employed. One possibility is a CMOS camera with three sensor chips based on the common CCD technique which would significantly increase the sensibility. Further, pulsed illumination sources with high radiance enable high illumination intensities and less heat input at the same time. Nevertheless the greatest part of the measurement uncertainty arises from the encapsulated TLCs itself whereas it is assumed that the capsule process is the crucial factor. On this account, alternative encapsulation processes and thinner capsule walls might be a solution to this problem. A further decrease of the TLC capsule radius appears problematic as this would lead to a reduction of the amount of reflected light, which is dependent on the particle radius.

Laser Induced Fluorescence

Based on the optimized 2C2D-LIF method, measurements with high spatial and temporal resolution can be performed. A potential one is the temperature field measurement near an evaporating and fast moving meniscus. One the one hand, this shows how far the method is applicable for high resolution measurements including moving gas-liquid-interfaces; on the other hand this provides interesting results regarding the complex heat transfer mechanism near moving contact lines.

Compared to LCT, the LIF method has the disadvantage, that a light sheet is needed for illumination and that the simultaneous measurement of velocity fields requires additional effort. These problems were partly solved by employing confocal microscopy for temperature field measurement with volume illumination and adding tracer particles for simultaneous velocity field measurements. Both methods could be combined for measurements of temperature and velocity fields at high spatial resolution with volume illumination. Nevertheless a reduced signal to noise ratio is expected which restricts the temporal resolution.

Novel Particle Image Thermometry Methods

Particle image thermometry exhibits several advantages compared to dye based methods. As mentioned above, temperature and velocity fields can be obtained with volume illumination. Due to this elementary advantages, novel PIT methods should be developed to overcome the restrictions of LCT.

Generally there are particular physical effects which are conceivably useful for PIT. For example, the decay time of phosphorescence often shows strong temperature dependency. Phosphor particles could be exited by pulsed laser light and the phosphorescence decay time can be determined from successive images captured by a high speed camera. As a result, the temperature of every single particle can be achieved.

Besides the decay time phosphorescence shows another temperature dependent characteristic. Some phosphorescence materials exhibit wavelength dependent temperature sensitivity which can be measured selectively [15]. Compared to the decay time measurement, only one image is required to obtain the particle temperatures. Because it is not sure if sufficient signal intensities can be achieved with these methods, elementary tests should be performed in the beginning.

[118] has shown that surfaces coated with a polymer containing fluorescence dyes are applicable for temperature measurements. If the dyed polymer was used to form particles, these could be applied for temperature measurements. Here, the combination of temperature sensitive and reference dyes as suggested in section 5.2 can be applied for.

All mentioned novel PIT methods allow to use laser light for illumination, which is the greatest advantage compared to the established PIT method employing liquid crystals. If one of these novel methods can be realized with sufficient signal to noise ratio and temperature sensitivity, this would mean an important progress in the simultaneous temperature and velocity measurement in micro scales.

Appendix A

Appendix

In this chapter, high resolution velocity field measurements near a moving meniscus (A.1) and 3D velocity measurements of a toroidal flow in micro scales (A.2) are presented.

These works are presented in the appendix because they are not part of the main subject. Nevertheless, the principle of velocity field measurements is close to that of temperature field measurements. On the one hand, many similarities in the optical setup exist, and, on the other hand, applied image algorithms like particle detection also occur in LCT.

A.1 Velocity Field Measurements Near a Fast Moving Meniscus

This section describes the velocity field measurement behind a fast moving meniscus using micro Particle Image Velocimetry (µPIV). The measurements were performed with the background that no experimental data exist which deal with the velocity field in vicinity of a moving meniscus. The flow pattern here is extremely complex. While the typical Hagen-Poiseuille profile without radial velocity component is to be found far from the meniscus, the flow near the meniscus cannot have a convex velocity profile. As a matter of fact, the meniscus movement is characterized by adsorption of the liquid near the wall and liquid transport from the middle of the flow towards the three-phase contact line.

A.1.1 Basics of Capillary Invasion

A detailed discussion about previous studies dealing with capillary invasion and experimental measurement of contact angles and flow fields near contact lines is given in [93]. With regard to a discussion of the measured velocity fields in the vicinity of the three phase contact line, it is important to know some basics about capillary flows and moving contact lines.

In a vertical cylindrical capillary, where laminar flow is assumed, the overall balance of forces on the liquid is described by:

$$\left[z\frac{d^2z}{dt^2}+\left(\frac{dz}{dt}\right)^2\right]+\frac{8\eta\cdot z}{r^2}\frac{dz}{dt}+\rho\cdot g\cdot z-\frac{2\sigma\cdot cos(\Theta)}{r}=0 \tag{A.1}$$

where z is the height of the liquid column, ρ is the density of the liquid (the density of the gas is neglected), r the radius of the capillary, η the dynamic viscosity, σ the interfacial tension and Θ the contact angle. In equation A.1 the first term describes the inertial force, the second the viscous force, the third the gravity force and the last the capillary force. Nevertheless, there are some factors in capillary flows that are not considered in equation A.1: at the beginning of the filling process, the rise is impulsive and non-steady. The liquid sucked into the tube also causes a resistive force working against the capillary force. This has been taken into account by Kornev [65] who developed several models for the flow field around a capillary tube. Because the velocities are quite high at the beginning of the capillary rise, turbulence effects can occur which lead to a higher pressure drop. In the present work, these effects can be neglected since the maximum occurring Reynolds number is 55 - quite safely laminar. Another point is that the flow near the entrance is not fully developed so that the assumption of a parabolic Hagen-Poiseuille-profile is not correct. It is supposed that the flow develops to the parabolic Hagen-Poiseuille-profile after the characteristic entrance length. The entrance length depends on the Reynolds number and thus on the mean flow velocity [136] and is calculated to

$$\frac{L_E}{d}=\frac{0.6}{1+0.035\cdot \mathrm{Re}}+0.056\cdot \mathrm{Re} \tag{A.2}$$

with

$$\mathrm{Re}=\frac{\bar{u}\cdot d}{\nu} \tag{A.3}$$

where $\bar{u}$ is the mean velocity, d the inner diameter of the glass capillary, and ν the kinematic viscosity of the liquid. Near the meniscus, in the so-called meniscus zone, the flow is also not parabolic and rather complex. The length of the meniscus zone is estimated to be a few radii [151]. A schematic view is shown in figure A.1.

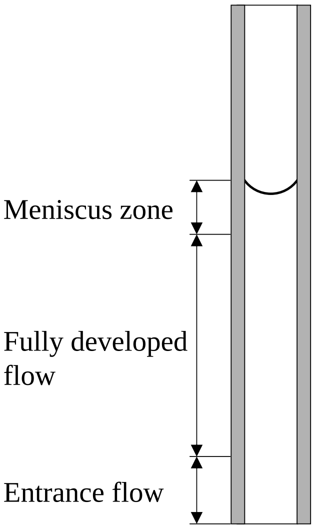

Figure A.1: Different flow regimes at capillary invasion

An additional important factor is the contact angle where it is distinguished between static and dynamic contact angles. Generally a contact line develops between a solid and two fluids. When a fluid is replaced by another one, a dynamic contact line develops. The static contact angle depends on the surface properties of the solid wall and surface tensions of the fluids. In addition to that, the dynamic contact angle depends on the contact angle speed and liquid properties like density and viscosity [20]. The typical flow field behind a meniscus is shown in figure A.2. In the macroscopic view, it can be seen that liquid is transported from the middle of the flow towards the three phase contact line. The flow field in the vicinity of the contact angle offers a rolling motion; the liquid is transported from the interface to the contact line where it adheres to the wall [29, 28, 129].

A.1.2 Experimental Method

In section A.1.2, the measurement setup and the measurement technique µPIV is described. Further, it also includes the measurement performance and the image analysis.

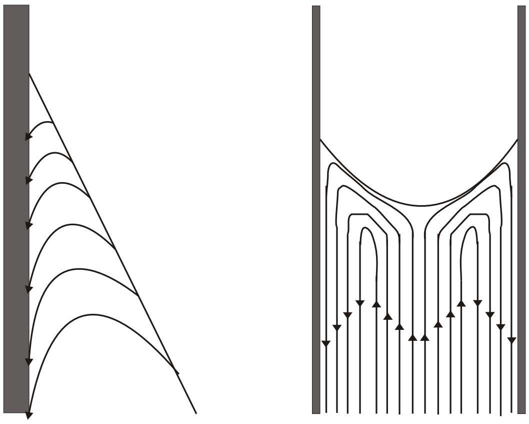

Figure A.2: Streamlines of capillary flow. Left: near the contact line. Right: near the meniscus

Experimental Setup

A glass capillary tube with an inner diameter of $d = 720$ µm is installed vertically. The bottom of the capillary is held beneath the top-surface of a reservoir. The reservoir has an inner diameter of 10 mm and is connected to a syringe-pump with silicon tubing (see figure A.3). When the reservoir is filled with the working fluid from the syringe, the interface of the working fluid rises and eventually contacts the capillary tube, beginning the capillary infiltration. A syringe pump is used to guarantee repeatable initial boundary conditions for the experiment as the rising velocity in the reservoir has a significant influence on the capillary rising velocity. Measurements without using the syringe pump have shown large differences in capillary raising height and velocity.

In the present experiments, the µPIV method is employed instead of the standard PIV. One major difference to the standard PIV technique is that the whole volume around the FOV is illuminated. The depth of the measurement volume is defined by the depth of field of the image capturing optics. Particles in front or behind the measurement volume appear blurred. Another difference is the use of special fluorescent particles[1] as tracer particles [90]. The fluorescent particles which are seeded in ethanol[2] have a diameter of 1 µm and are dyed with

---

[1] Duke Scientific Cooperation fluorescent microsphere suspension

[2] 3.125 ppm

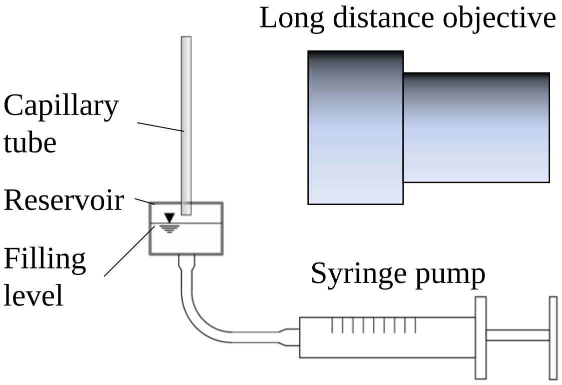

Figure A.3: Sketch of measurement section, laser beam direction is in viewing direction

rhodamine[3]. The dye of the particles is excited with laser light of 532 nm and starts to emit fluorescent light after a few nanoseconds. Following the Stokes law, the fluoresced light has a lower frequency and thus a higher wavelength than the excited light. This property is used to separate the fluorescence from the laser light using an optical long pass filter[4]. Doing so, any unwanted reflections of the liquid-gas-interface or glass walls are eliminated and only the fluoresced light from the particles is captured.

For the excitation of the particles, a double-pulsed frequency-doubled Nd:YAG-laser[5] is used and the images are captured by a CMOS camera[6]. With a long distance microscope[7], a pixel size of 1.9 µm and a working distance of 45 mm are achieved. The magnification, low pulse energy and small emitted light intensity from the small particles lead to a low photon density which necessitates an image intensifier[8].

Experimental Procedure

Before every measurement, the reservoir is filled with the suspension of ethanol and fluorescent particles until the ethanol surface is intimately beneath the capillary tube. Then the image capturing and the syringe pump are started simultane-

---

[3] maximum excitation wave-length at 542 nm, maximum emission wavelength at 612 nm

[4] $t > 545$ nm

[5] Lee 800-PIV/40G, $\lambda = 532$ nm, pulse energy: 14 mJ, pulse length: 90 ns at 1 kHz repetition rate

[6] HS 650 Powerview, 12bit, 318 image pairs per second at 1024 x 1280 pixels)

[7] Leica Z16

[8] Videoscope VS4-1845HS

ously, and the infiltration begins as soon as the ethanol surface hits the bottom of the capillary tube. After each measurement, the tube is flushed with pure ethanol and ventilated with hot air so that the fluorescence particles are removed and ethanol is evaporated. This procedure is necessary because ethanol droplets or particles adhering to the glass wall significantly influence the capillary flow. Using ethanol (see table A.1) as the working fluid is advantageous as it evaporates faster than water, due to its higher vapor pressure.

The measurements are conducted on different positions in flow direction (z = 1, 2, 3, 6, 9, 12 mm) where z donates the distance to the tube entry. This is done to study the dependency of the shape of the meniscus on its velocity and on the flow pattern behind the meniscus. The measurement frequency lies between 200 Hz and 600 Hz depending on the meniscus velocity.

To investigate the infiltration height over time for the whole filling process, measurements with a lower magnification (pixel size: 16 μm) are performed. The FOV now includes the reservoir and a sufficient length of the tube. It appeared more important to investigate the high dynamic flow in the beginning of the rise since there are already many experiments which are engaged in the raising height over time [46, 78, 112, 134, 147]. The rising height of the ethanol column is determined by processing the data with the lower spatial resolution. Here, the interface is the brightest part of the capillary flow and therefore delivers information about the infiltration height.

The velocity fields were extracted from the acquired images using a custom-written PIV code called ED PIV[9]. In all cases, $32\,x\,32$ pixel interrogation areas are used, spaced evenly on a $16\,x\,16$ pixel grid. The images were recorded in pairs with a time step of 100 ms between the two images comprising each pair. The meniscus position was tracked as it moved through the FOV by determining the intensity of the flow averaged in radial direction. Then the intensity of the meniscus is indicated by the intensity maximum. The images are trimmed such that the meniscus in the first image of each pair always occurs at the same position. The meniscus position in the second image of each pair is displaced according to its speed. This trimming creates effectively a reference frame that moves with the meniscus and a quasi-steady velocity field. The quasi-steady velocity field then allows the correlation averaging technique to be used. Correlation averaging in

---

[9] Written by Lichuan Gui

ρ [10^3 kg/m^3]	σ [10^{-3} N/m]	η [10^{-3} Pa·s]
0.789	22.55	1.2

Table A.1: Fluid properties of ethanol at 20 °C

turn allows the interrogation area size to be minimized without introducing noise into the velocity fields.

When light passes through curved bodies with different refractive indices, the effect of refraction has to be taken in account. This happens in the present case, as particles in a glass tube are observed. To determine this effect, the velocity profile far from the meniscus has been measured and compared to the typical laminar flow profile which is described by the Hagen-Poiseuille law,

$$u(r) = u_{max}\left[1 - \left(\frac{r}{R}\right)^2\right] \tag{A.4}$$

where u_{max} is the maximum velocity in flow direction. For a cylindrical tube, u_{max} is twice as large as the mean velocity, $\bar{u}$. As indicated in figure A.4, the measured velocity profile differs from the calculated one. There are two main reasons for this deviation. On the one hand the measurement volume is not a straight plane in radial direction but curved due to the refractive indices of the materials (ethanol, glass, air). For this reason, the particles in the middle of the flow appear deformed in one direction, while the particles near the wall appear sharp. Even if the measurement volume followed a straight plane through the center of the tube, the fact remains that the measurement volume does not have an infinitesimal thickness. Because the measurement volume is defined by the depth of field of the optics (estimated to 70 µm), particles also contribute to the velocity field, which follow the slower liquid in front and behind the center line.

A.1.3 Results

A change of the contact angle over the infiltration process is qualitatively observed; a quantitative measurement was not possible due to aforementioned refractive properties. In figure A.5, the meniscus shape as a function of the Capillary number

$$\mathrm{Ca} = \frac{\eta}{\sigma}\frac{\mathrm{d}z}{\mathrm{d}t} \tag{A.5}$$

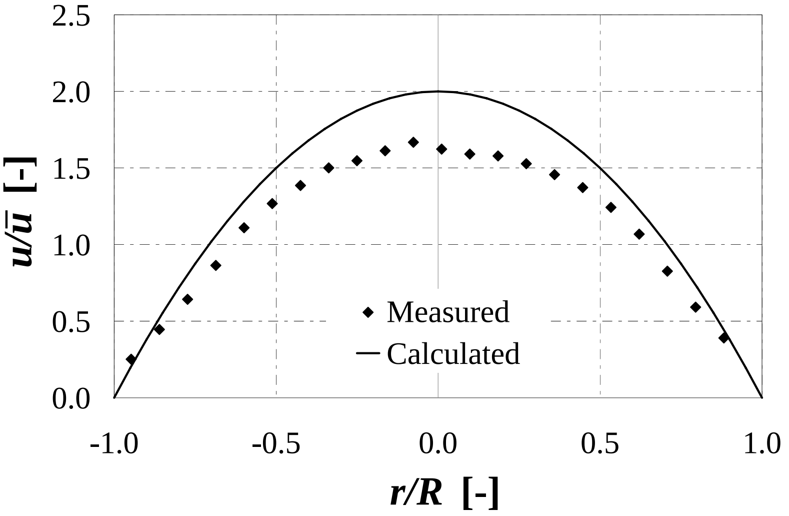

Figure A.4: Comparison between calculated and measured flow profile. Measurement was performed at z = 6 mm

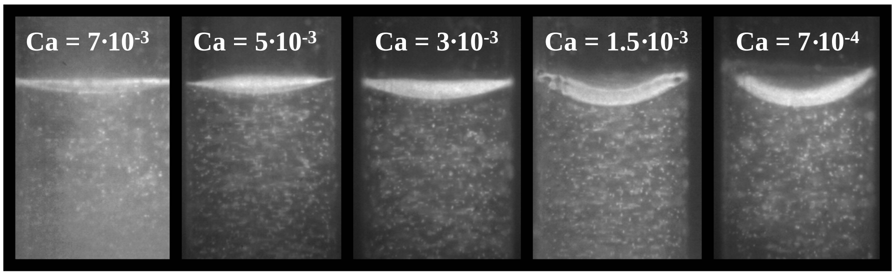

Figure A.5: Meniscus shapes at different Capillary numbers and thus different positions in flow direction

is shown. It can be seen that the curvature of the meniscus gets larger and thus the contact angle gets smaller with decreasing Ca. This qualitative result - a decreasing contact angle with increasing contact line velocity - corresponds to existing results in literature.

In figure A.6, the initial velocity is presented. The data was achieved by the mentioned global measurements of the whole liquid column. From the data of measurement 2 in figure A.6, it can be seen that the meniscus is accelerated in the beginning of the suction and after a certain maximum velocity (120 mm/s) is decelerated. This corresponds to the results of the model of Kornev and Neimark [65].

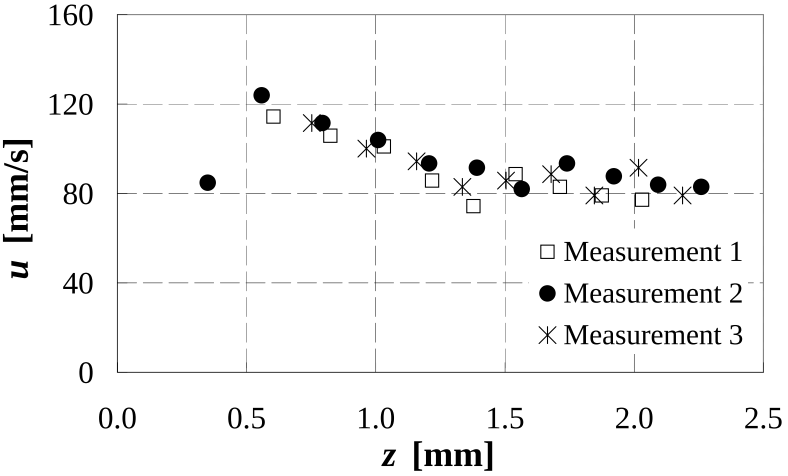

Figure A.6: Initial velocity of the meniscus at different z-positions

When the meniscus is trapped with the automatic trimming of the images, it is possible to watch the particle movement by superimposing all images of one measurement (figure A.7). The flow shows the typical rolling form; the liquid from the middle of the flow is transported towards the three-phase contact line. Furthermore, it can be seen that in the middle of the flow, behind the meniscus, a zone is formed where only little liquid movement relative to the meniscus movement takes place.

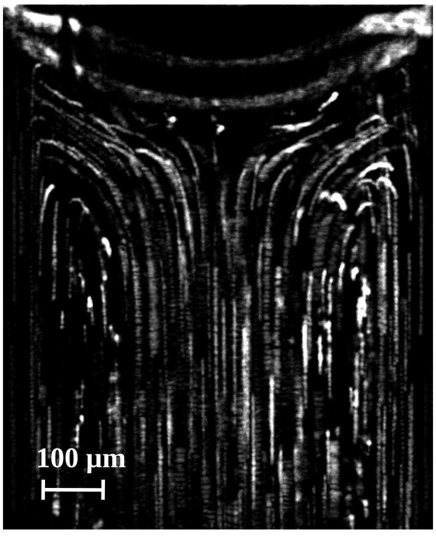

Figure A.7: Particle pathlines at z = 9 mm. Obtained by superimposing multiple particle images

To explain the velocity profile near the meniscus more precisely, beside the velocity field in figure A.8 top, also the development of the velocities in z- and r-direction with increasing distance from the meniscus is presented in the lower part. Here it becomes apparent that the profile of the velocities, u against r is flattened at the meniscus and changes to the typical Hagen-Poiseuille profile after a certain distance from the meniscus. This becomes clear when considering the diagram in figure A.8. At the meniscus, u is independent on r and equal to the propagating velocity $\bar{u}$. After a certain distance, the flow develops into a typical pipe flow with its parabolic u over r distribution (see also figure A.4. Another indication for an fully developed pipe flow is the absence of radial velocity components. From the diagram in figure A.8 it can be concluded that the length of the meniscus zone is less than one radius, which contradicts the assumption of [151] of a few radii.

The flow fields at different z-positions from the tube entrance are shown in figure A.9 for a better illustration. The velocities in z- and r-direction were normalized with

$$\overrightarrow{u}' = \frac{\overrightarrow{u} - \bar{u}}{\bar{u}}. \tag{A.6}$$

So the typical rolling flow field can be recognized more easily. It can be seen that the curvature of the meniscus increases with increasing z-position where the mean velocity and thus the Capillary number decreases. This directly influences the flow field, which adapts to the meniscus shape.

To summarize, it can be said that new measurements are provided that confirm theories of the flow field behind a moving meniscus in a capillary tube [129]. Flow fields were observed which are in some points similar to the observed flow profiles of related experiments [33, 127, 22]. Further, new experimental data regarding the initial velocity is provided which agrees with the predicted behavior from [65].

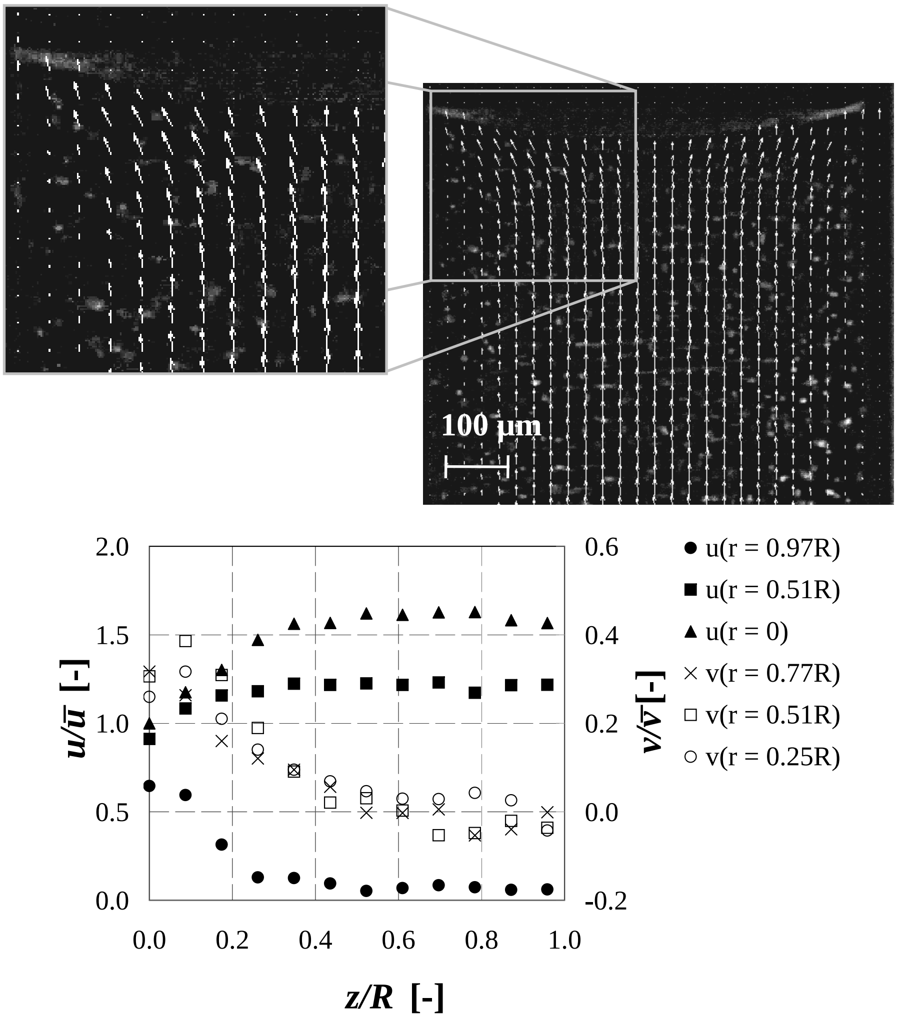

Figure A.8: Top: velocity field at $z = 3$ mm. Bottom: Velocities in z- (u) and r-direction (v) on several radii over the distance from the meniscus, z/R

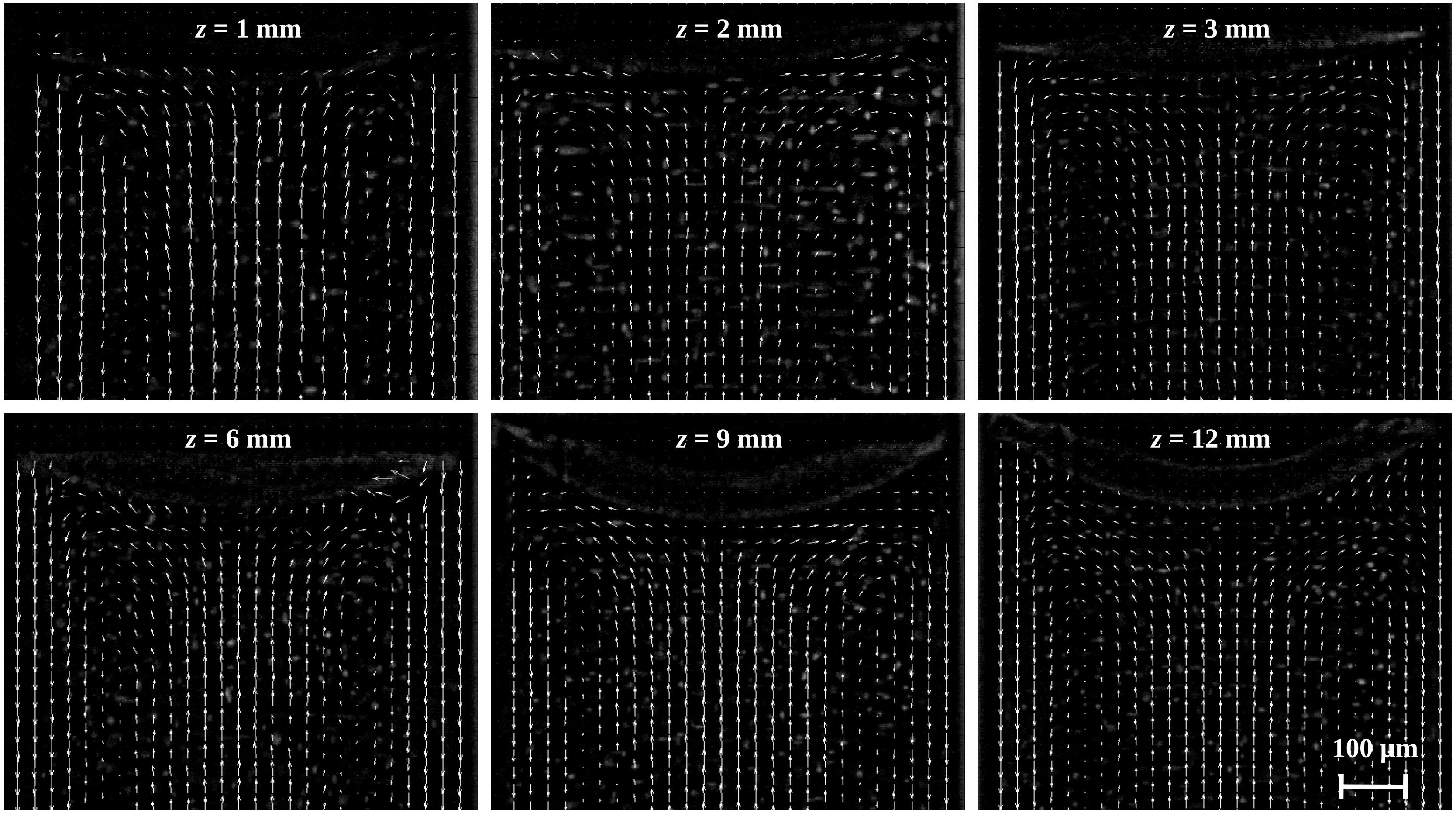

Figure A.9: Velocity profiles at different z-positions. The velocity-vectors are normalized as shown in equation A.6

A.2 Three Dimensional Velocity Measurement of a Toroidal Flow using Defocussing Particle Tracking Velocimetry

In this chapter, the 3D velocity measurement of a toroidal micro flow is presented. It focuses on the description of the measurement technique of defocussing particle tracking velocimetry. The generation of the toroidal flow is described in detail in [71].

A.2.1 Basics of 3D-μDPTV

State of the Art

Two-dimensional μPIV, where x- and y- velocity components are measured, has been introduced 1998 by Santiago et al. [125] and further developed by Meinhart et al. [90] and Wereley et al. [141]. Since many flows show 3D characteristic, effort has been put in 3D micro flow visualization to additionally determine the third velocity component.

The stereoscopic μPIV method has been successfully applied by Lindken et al. [83, 85] and Bown et al. [14]. A resolution of $10\,x\,10\,x\,10\,\mu\text{m}^3$ was achieved by using two cameras which optical axes are not centrical to the illumination axis [14]. Thus, two vector fields are captured from different angles and a recombination of the third velocity component is possible from the deviation of the two vector fields. The first implementation of the stereoscopic principle for micro applications was done by Klank et al. [63] in 2002. They did not use two cameras but a translation stage which made a shifting of the area of interest possible. The overlapping part of the two images was recorded with a slightly different angle and the third velocity component could be determined from the deviation of the velocities. Because the images were not captured simultaneously, only stationary flows could be investigated. With the stereoscopic method, a high spatial resolution can be achieved due to a high particle seeding density. The temporal resolution is comparable to the temporal resolution of 2D μPIV applications and therefore mainly depends on the optical equipment and the acceptable laser irradiance. Disadvantageous are the complex alignment of the two cameras which also necessitates the calibration and in-situ dewarping of the two fields of view. Different image processing algorithms (3D-μPTV (micro particle tracking velocimetry), stereoscopic μPIV, tomographic μPIV) were investigated by Lindken et al. [84]. The different kinds of image processing were conducted on images taken with one particular stereoscopic setup.

A very accurate but also very complex method to measure 3D flow fields with high spatial and temporal resolution exhibits digital holographic PIV. Recent works were presented from [77, 126, 148] and measurements with a frequency up to 4 kHz were reported in a measurement volume of $300 \, x \, 100 \, x \, 100 \, \mu m^3$ [77]. The three dimensional particle images are analyzed with PTV algorithms to determine the velocity vectors.

Another rather simple method which provides high accuracy in all three dimensions is the combination of the scanning 2D PIV measurement method and the continuity equation and has been applied by Bown et al. [13] for micro flows. For each interrogation area, the out of plane velocity component is calculated following the mass conservation. Bown et al. [13] investigated a flow over a step in a micro channel and received a spatial resolution of $45 \, x \, 45 \, x \, 11$ μm. Because scanning is stepwise, only stationary flows can be investigated. Furthermore the direction of the out-of-plane component is not known and the method therefore reliant on boundary conditions.

Three velocity components of micro flows have been measured by Speidel et al. [131] who used the defocussing concept. Particles with a diameter of 200 nm which are out-of-focus show diffraction rings at a certain distance from the object plane. The diameter of this diffraction rings depends on the distance to the object plane. Wu et al. [146] used the same technique and were able to track multiple particles. Park and Kim [103] used the outer diffraction ring to determine the z-position of 500 nm fluorescent particles. They achieved a resolution of 5.16 μm in all three spatial directions.

An extension of the defocussing concept is the use of a special pinhole mask within the optical way. For macro scales, the method has first been implemented by Willert and Gharib 1992 [143] who measured three dimensional structures of a vortex ring. Pereira et al. [107] used three cameras, one behind each pinhole. The advantages of this complex setup are higher measurement accuracy due to higher particle seeding densities and higher temporal resolution due to a greater amount of captured light. Pereira et al. [106] observed the measurement technique concerning its accuracy and applicability for 3D velocity measurements. To achieve the velocity in all directions, a grid with dots was employed. They found that the in-plane error is 0.08 pixel, while the out-of-plane error is 1.3 pixel. To determine the error of the velocity measurement, a rotating disk with spots was used. The out-of-plane error therefor was 15 times higher than the in-plane error. The applicability of the technique was observed on a propeller flow. On this account, a bubble generator is placed below a propeller with a diameter of 67 mm and the bubbles were taken as tracer particles for 3DPIV.

The defocussing principle was first applied for micro-scale measurements by Yoon and Kim [149] in 2006. They measured a flow over a backward facing step in a channel with a height of 50 µm. In 2007, Pereira et al. [108] measured the velocity distribution in an evaporating water droplets with a measurement volume of $400\,x\,300\,x\,150$ µm^3 and a measurement rate of 250 frames per second. In both works, an inverted microscope was used and the fluorescence particles were excited from the top, which is opposed to the direction of observation.

In the present work, the illumination and the image capturing was accomplished from the same direction. This has the advantage that the technique can also be applied in applications where an optical access from two sides is not possible. With the defocussing technique, a toroidal flow in a channel with a height of 50 µm which is caused by an electrical field in combination with a focused IR laser is observed.

Measurement Principle

When a point source has a certain distance from the object plane, the image of the point source appears blurred. Placing a pinhole mask within the optical way leads to a projection of its shape on the image plane (see figure A.10). The effect can be seen at apertures with a small diameter: the point spreading is reduced, the image of the out of focus point source still appears as a point image and as a result, the focal depth is greater.

When using masks with e.g. three holes, the image of the out-of-focus point source appears as three points at the image plane (figure A.11).

The distance between the points increases with increasing distance of the point source from object plane (figure A.11). Therefore, the z-position of the point source

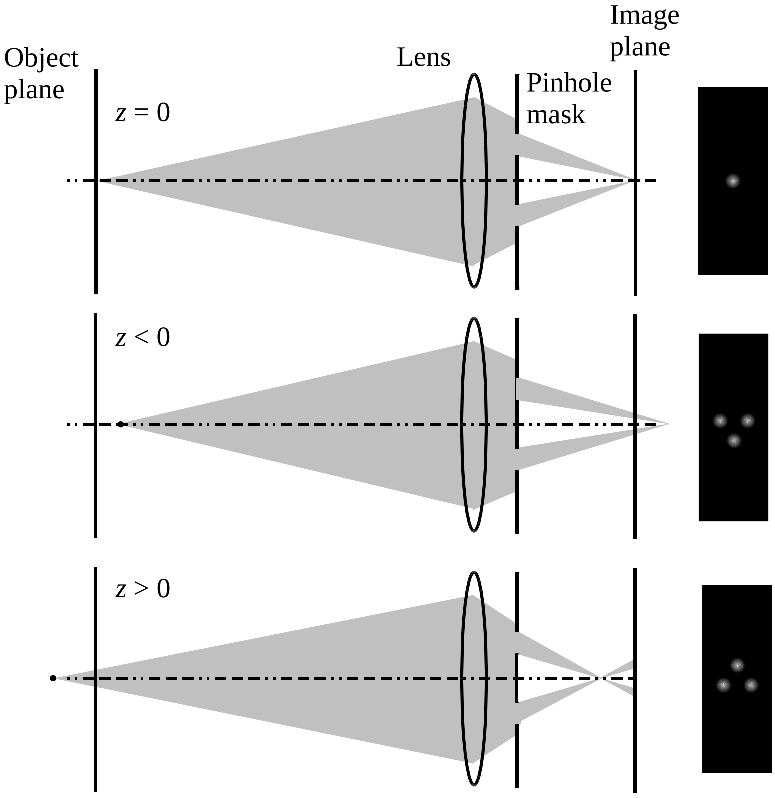

Figure A.10: Schematic illustration of the basic defocussing concept. Different z-positions of the point source lead to different point source images

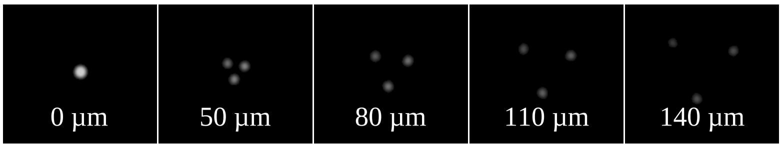

Figure A.11: Particle images at increasing distance from object plane using a mask with three pinholes can be determined from the point images. If the distance from the point source to the lens plane is smaller than the distance from the lens plane to the object plane, the point image appears mirrored (see figure A.11).

Pereira and Gharib [106] did geometrical analysis on the defocussing principle and calculated the separation of the point images b depending on the distance z of the point source to the object plane with

$$b = M \cdot d \cdot \left| \frac{z}{L - z} \right| . \tag{A.7}$$

In equation (A.7), d is the distance of the pinhole centers, L the distance between the aperture and the object plane and M the optical magnification.

As can be seen from equation (A.7), the dependency of b on z is not linear over the whole range of z. In the present experiments, b is described by r, which is the radius of the circumcircle through the three image points. The dependency between r and z shows quadratic character, which can be seen in figure A.12.

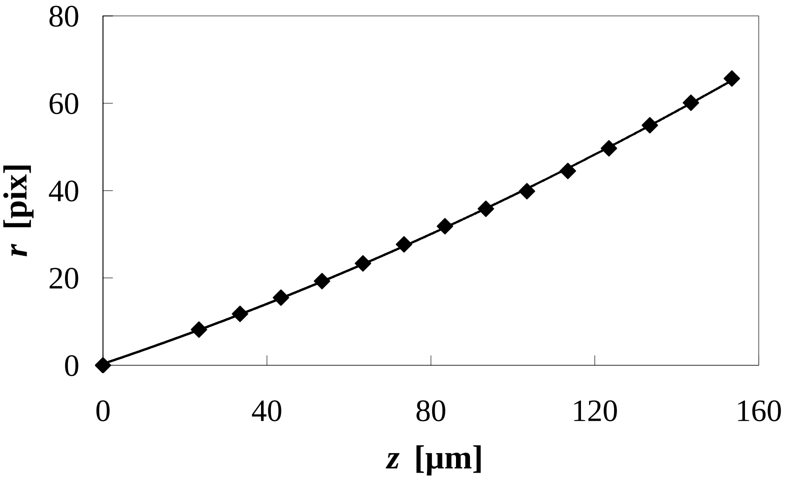

Figure A.12: Measured radius of circumscribed circle through particle images in dependency of z-direction. The gradient shows quadratic properties.

The dependency of the pinhole diameter d on the distance of the imaged points b can also be seen in equation (A.7). In the practical sense, this means that $\mathrm{d}b/\mathrm{d}z$, which represents the measurement sensitivity, is increased with d. On that account, the choice of the mask should be done with regard to the application, which means the extension of the measurement range in z-direction. On the other hand, when the distance of the particle images is too great, problems arise with over-lapping triangles at higher particle concentration. Smaller pinholes automatically lead to smaller diameters of the particle images which increases the measurement accuracy. The disadvantage is the smaller amount of light inclining on the sensor chip and therefore the lower signal to noise ratio. Since the intensity of the particle images follows the point spread function of an out-of-focus point source, the intensity of spots drastically decreases with increasing z. At a certain distance, the background noise drowns out the measurement signal.

A.2.2 Experimental Method

Experimental Setup

A pinhole mask with three holes and a hole diameter of $d_h = 1\,\text{mm}$ was used. The circumcircle through the centers of the holes has a diameter of $d = 4\,\text{mm}$. The pinhole mask was located in the image-capturing part of the optical way which made coaxial illumination possible. A schematic sketch of the microscope is shown in figure A.13. The flow is seeded with 1 µm fluorescence particles, which were illuminated by green light and emitted red light. A dichroic mirror separates the emitted light from the exciting light so that only the particle images were captured with a CCD-camera and unwanted background reflections were removed. The toroidal flow was generated by focusing an near-infrared (IR-) laser (1064 nm) within a micro channel in combination with an alternating electrical field. The specific setup is described in detail in [71].

Experimental Procedure

The measurement method is calibration based, which necessitates in-situ calibration for every change in the optical setup. A validation with the theoretically determined $\mathrm{d}r/\mathrm{d}z$, respectively $\mathrm{d}b/\mathrm{d}z$ dependency which can be found in [106] is not possible, since optical parameters like the relative position of the mask within the optical path are not known. The calibration itself was conducted before the measurement and the optical setup had to remain unchanged thereafter. Further, it is important to choose the position of the object plane outside the channel. Particles which stick to the wall next to the object plane should appear as three single spots.

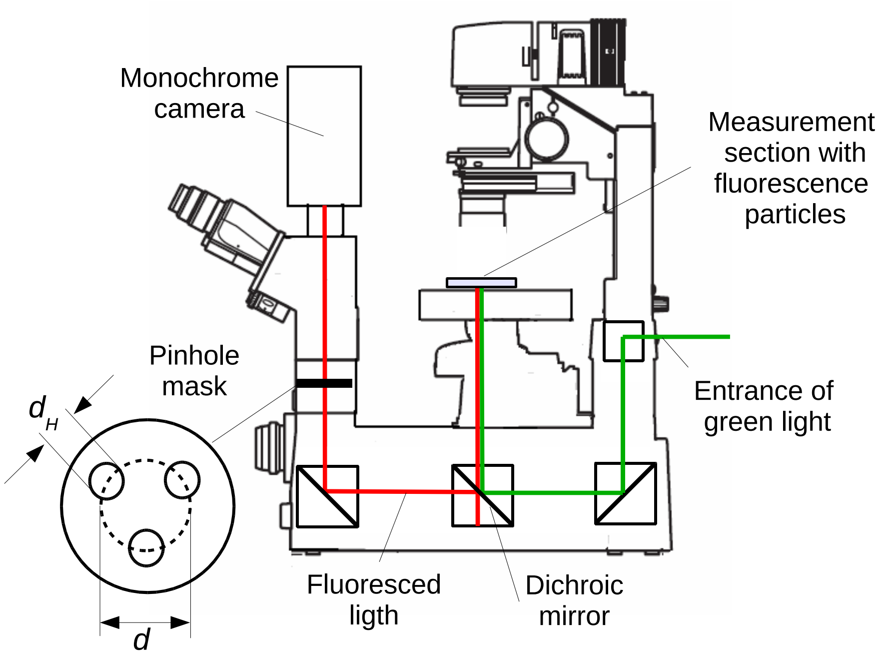

Figure A.13: Schematic of the optical setup, the pinhole mask is within the optical way

To obtain the dr/dz dependency, the object plane was moved in 10 µm steps. This led to an erroneous influence of the changing optical path. The actual z-position can be calculated from $z_{act} = z_{cal}\ n_1/n_2$. The adjusted length z_{cal} is the length which the optical table was moved during the calibration process, and n_1, n_2 the refractive indices of the medium between lens and object and of the medium inside the channel. Since an immersion objective[10] was used, the occurring error is negligible compared to a normal lens with air between lens and object. The result from the calibration procedure is the dependency dr/dz as shown in figure A.12. With a quadratic approximation, the z-position was from the radius of the circle r through the three particle images. For the calibration and the measurement itself, the liquid was doped very dilute so that only a few particles were found in the field of view. The reason therefore is that particles which follow the toroidal flow sooner or later encounter in the center of the torus, where the IR-laser is located. This leads to erroneous triangle detection. To measure the exact position of the particles in the middle of the torus, overlapping triangles had to be avoided.

---

[10] 20x water immersion objective, Nikon

Therefore, the x- and y- position of the FOV respectively IR-laser was moved until a particle was captured and the measurement was started.

Image Analysis

In this section, the image analysis for the calibration procedure and the actual measurement is described. Since both analysis procedures contain similar algorithms, they are only described once, primarily in the calibration analysis part. To minimize confusion, the concept is explained again: Three particle images span a triangle. The triangle has a circumcircle with the radius r and a diameter b. The center of the circumcircle represents the center of the out-of-focus particle plus a certain deviation, which is described in detail in section A.2.3.

The exact particle positions are specified by an in-focus-image of the particles which is done in respect to determine the x-, y-, and z-dependent deviation of the triangle centers. The positions of the particle images are detected by means of a threshold filter and algorithms are employed to achieve subpixel accuracy. The x-, y-coordinates of the triangle center and the radius of the circumcircle r are calculated from the particle image coordinates x_i and y_i with

$$r = \sqrt{(x - x_i)^2 + (y - y_i)^2}. \tag{A.8}$$

Further, the three vectors from the triangle center towards the particle images are determined. They are needed to sort out erroneous triangles and for the generation of the examination mask which is employed in the measurement data analysis (figure A.14).

By means of the automatically created correlation mask, it is possible to detect particle images which belong to one particle, even if the triangles overlap.

The procedure to detect the particle images is similar to the calibration procedure. To detect the triangles, the image is cross correlated with the examination mask. The maxima of the resulting correlation matrix represent the centers of the triangles. Further, an interrogation area in the original image around the detected centers is defined. The interrogation area is multiplied with the examination mask so that particle images, which do not belong to the triangle, are minimized. Particle images belong to the triangle when they all have nearly the same distance to the center.

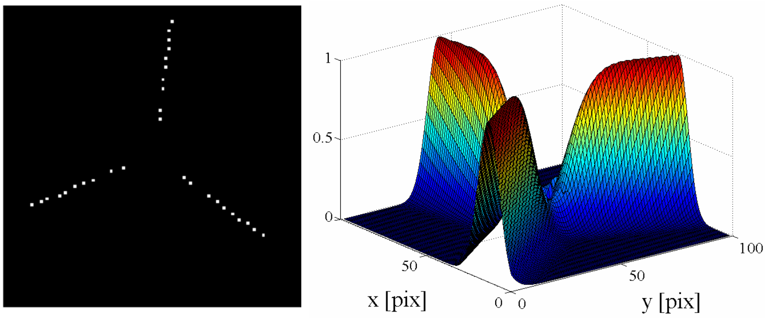

Figure A.14: Left: measured relative distance of spots from triangle center, achieved from calibration data. Right: constructed correlation mask for triangle detection in the analysis of the measurement data

When considering the movement of only one or two particles, particle trajectory is not necessary. The path of the particle can be directly reconstructed from the estimated coordinates from each image.

A.2.3 Results

In this section, the observed particle pathlines of the toroidal flow are explained shortly, while more effort is put into the discussion of the measurement accuracy.

3D Pathlines

Assuming that the flow profile is rotation symmetric in the X and Y-plane, the position in radial direction can be calculated from

$$R = \sqrt{X^2 + Y^2}. \tag{A.9}$$

The coordinates in the image plane are described by x, y, and z, while X, Y, and Z are used for the position of the object.

The constructed 3D particle pathlines in figure A.15 left and right show the expected flow field of the torus. Due to wall effects, the flow field is elliptical. Further, the main axis of the ellipse is not parallel to the wall which is caused by the acceleration of the liquid near the torus axis.

When considering the R-position over time (figure A.16), the periodical behavior can be seen. A Fourier transformation of the Z-position of the particle leads to

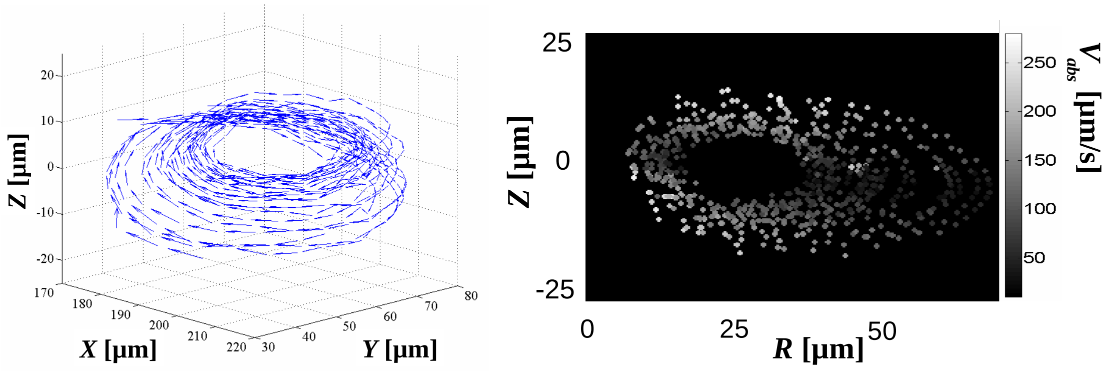

Figure A.15: Left: Velocity vector lines of a circulating particle. Right: Particle positions in Z- R-plane

the power spectral density function which affirms the periodical behavior. The particle has a rotation frequency of approximately 1.2 Hz.

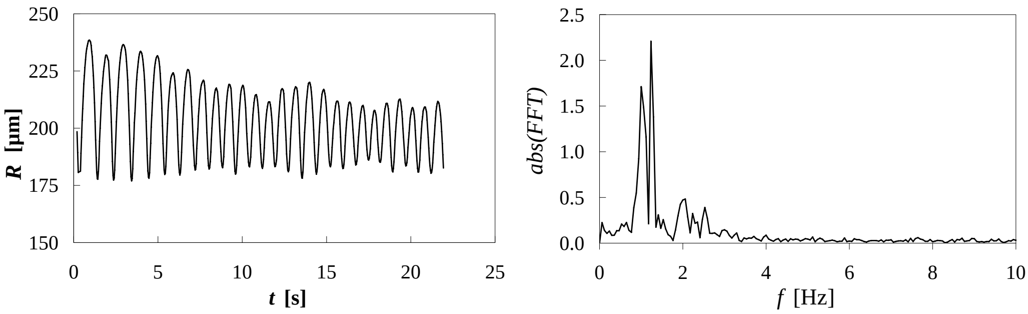

Figure A.16: Left: Particle position in X- Y-plane over time. Right: Power density distribution for R-position of particle

Measurement Accuracy

As already mentioned, deviations δ_x and δ_y exist between the actual X-, Y- particle positions and the center x, y of the particle image triangle. The dependency is described by $X = x + \delta_x$ and $Y = y + \delta_y$. The deviations are strongly dependent on the X-, Y-, and Z-positions. The gradients $\mathrm{d}\delta_x/\mathrm{d}Z$ and $\mathrm{d}\delta_y/\mathrm{d}Z$ are further dependent on X and Y which describe the position of the particle: the greater the distance from the optical center, the greater the deviation gets. This fact can be easily explained by the theorem of intersecting lines and the simplified classical optics shown in figure A.17.

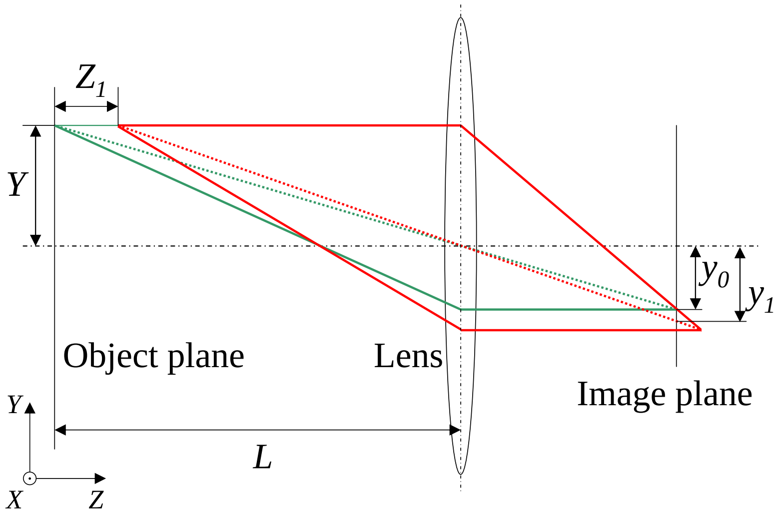

Figure A.17: Simplified schematic sketch of the optical path. An out-of-focus point source (red line) with the same distance Y like the in-focus point source (green line) has another image center (y_1) than the image of the in focus point source (y_0).

When regarding equation (A.10) for the calculation of the deviation dy, the dependency on Z and Y becomes clearly.

$$\delta_y(Y,Z) = Y\left(\frac{L}{Z} - 1\right)^{-1} \tag{A.10}$$

When assuming $L >> Z$, equation (A.10) shows an approximate linear dependency on Z. The limit of the function then calculates to

$$\left(\delta_y\right)_{L>>Z} = \frac{Y \cdot Z}{L}. \tag{A.11}$$

The derivation of A.10 with respect to Z is

$$\frac{\mathrm{d}\delta_y}{\mathrm{d}Z} = \frac{Y \cdot L}{\left(\frac{L}{Z} - 1\right)^2 \cdot Z^2}. \tag{A.12}$$

Again, for $L >> Z$, (A.12) simplifies to

$$\left(\frac{\mathrm{d}\delta_y}{\mathrm{d}Z}\right)_{L>>Z} = \frac{Y}{L}. \tag{A.13}$$

This approximate linearity has been observed in the present experiments and is shown in figure A.18. Although only five particles have been investigated, the approximate linearity is clearly recognizable.

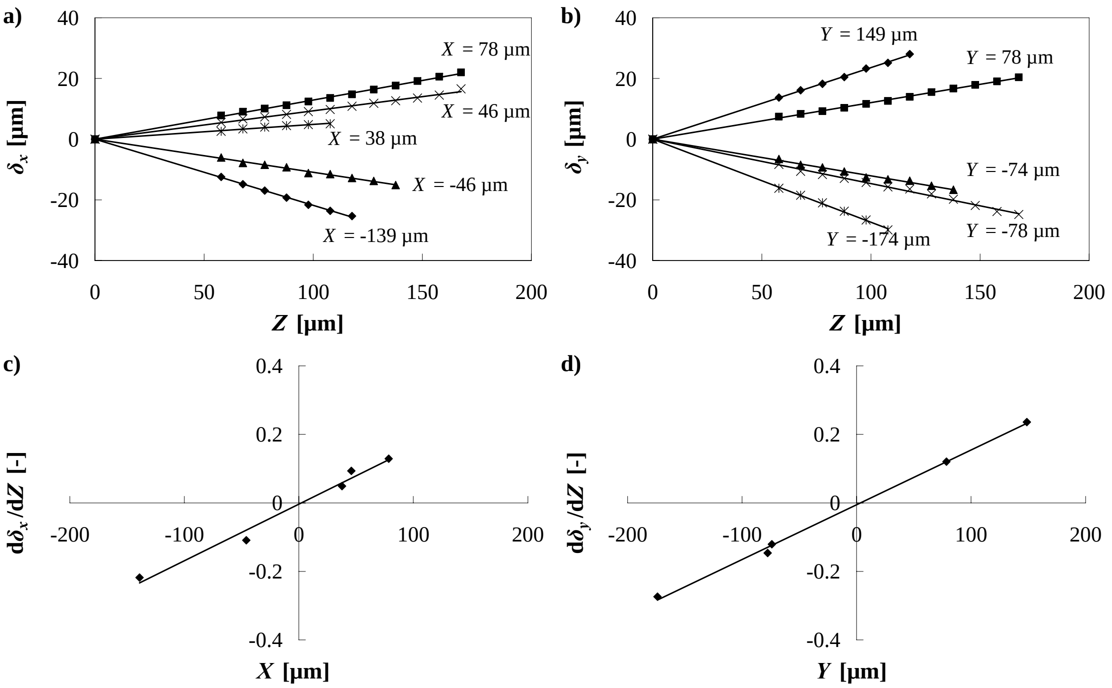

Figure A.18: a) and b): X-, Y-deviations over Z for several particles show approximately linearity. c) and d): gradients $\mathrm{d}\delta_x/\mathrm{d}Z$ and $\mathrm{d}\delta_y/\mathrm{d}Z$ are approximately linearly depending on the X-, Y-position. The gradients increase with increasing distance from image center respectively the center of the mask.

	$C_1[-]$	$C_2[-]$	$C_3[1/pix]$	$C_4[pix]$
X	$-2.19 \cdot 10^{-2}$	0.194	$-4.460 \cdot 10^{-3}$	-8.396
Y	0.131	0.361	$-1.846 \cdot 10^{-3}$	-11.200

Table A.2: Coefficients for x-, y-position correction

Based on the accepted linearity, a linear polynomial function is approximated

$$\begin{aligned} Y &= y + y \cdot C_{1,y} + r \cdot C_{2,y} + y \cdot r \cdot C_{3,y} + C_{4,y} \\ X &= x + x \cdot C_{1,x} + r \cdot C_{2,x} + x \cdot r \cdot C_{3,x} + C_{4,x}, \end{aligned} \tag{A.14}$$

where r is the radius of the circumcircle. The coefficients for X- and Y- directions are calculated for the used optical setup and are shown in Table A.2.

Besides the deviation in x- and y- position, there are further errors. In the following, known error sources are addressed and the achieved accuracy is estimated.

- During the calibration, the table was moved manually and therefore reproducibility is not assured. Further, the adjustment has a certain unknown play.

- The accuracy of the particle image determination is approximately 0.1 pixels [113].

- Due to the pinhole principle, the incident light is minimized which necessitated amplification of the camera. This again led to amplification of the measurement noise and a decrease of the signal to noise ratio, which affects the particle detection.

- When the motion of the particle is fast, the particle image shows a trail which is caused by the exposure time of the camera. Due to the above mentioned minimized incident light, the exposure time could not be further reduced. This trail affects the correct detection of the particle centers.

- During the measurements, it was not possible to totally suppress the flow in X- and Y-direction which caused an additional unwanted X- and Y- velocity component, released from the toroidal flow.

- The optical setup affects the measurement accuracy with the lens aberration and the limitation in resolution due to diffraction. Further, it was not possible to adjust the mask in the way that the optical axis fits to the center of the mask.
- The effect of Brownian motion has been calculated using the equation of [103]. For 500 μm particles in water, the diffusion length is calculated to 0.2 μm which is small compared to the total error.

For the estimation of the present accuracy it showed that the influence of the subpixel accuracy of 0.1 pixel is negligible compared to the polynomial approximation of the values, presented above. Here the measurement accuracy is generously estimated to be ±2 pixels which is ±2 μm with the applied optical setup. The deviation in z-direction is determined from the mean standard deviation of the measured radii from the calibration procedure. The standard deviation (95 %) is ±1.3 pixels which corresponds to ±3.8 μm absolute.

Bibliography

[1] ADRIAN, R. J.: *Particle-Imaging Techniques for Experimental Fluid Mechanics*. Annu. Rev. Fluid Mech, 23:261 – 304, 1991.

[2] ANDERSON, M. R. and J. W. BAUGHN: *Hysteresis in Liquid Crystal Thermography*. Journal of Heat Transfer, 126:339 – 346, 2004.

[3] ANDERSON, M. R. and J. W. BAUGHN: *Liquid-Crystal Thermography: Illumination Spectral Effects. Part 1 - Experiments*. ASME J. Heat Transfer, 127:581 – 587, 2005.

[4] ANDERSON, M. R. and J. W. BAUGHN: *Liquid-Crystal Thermography: Illumination Spectral Effects. Part 2 - Theory*. ASME J. Heat Transfer, 127:588 – 597, 2005.

[5] ARBELOA, T. L., M. J. T. ESTEVEZ, F. L. ARBELOA, I. U. AGUIRRESACONA and I. L. ARBELOA: *Luminescence properties of rhodamines in water/ ethanol mixtures*. Journal of Luminescence, 48&49:400 – 404, 1991.

[6] ASHFORTH-FROST, S. and U. W. RÜDEL: *Thermal and Hydrodynamic Visualisation of a Water Jet Impinging on a Flat Surface using Microencapsulated Liquid Crystals*. International Journal of Fluid Dynamics, pages 111 – 119, 2003.

[7] BAKRANIA, S. and A. M. ANDERSON: *A Transient Technique for Calibrating Thermochromic Liquid Crystals: The Effects of Surface Preparation, Lighting and Overheat*. Proc. ASME International Mechanical Engineering Congress & Exposition, November 17 - 22, 2002, New Orleans, pages 1–7.

[8] BAUGHN, J.W., M. R. ANDERSON, J. E. MAYHEW and J. D. WOLF: *Hysteresis of thermochromic liquid crystal temperature measurement based on hue*. Journal of Heat Transfer, 121:1067 – 1072, 1999.

[9] BEDNARZ, T., E. FORNALIK, T. TAGAWA, H. OZOE and J. S. SZMYD: *Convection of Paramagnetic Fluid in a Cube Heated and Cooled from Side Walls and Placed below a Superconducting Magnet - Comparison between Experiment and Numerical Computations*. Thermal Science and Engineering, 14 No. 4:107–114, 2006.

[10] BEDNARZ, T. P., C. LEI and J. C. PATTERSON: *Particle Image Thermometry for Natural Convection Flows*. 16th Australasian Fluid Mechanics Conference Crown Plaza, Gold Coast, Australia, pages 1165–1170, 2007.

[11] BEDNARZ, T. P., C. LEI and J. C. PATTERSON: *An experimental study of unsteady natural convection in a reservoir model cooled from the water surface*. Experimental Thermal and Fluid Science, 32:844–856, 2008.

[12] BEHLE, M., K. SCHULZ, W. LEINER and M. FIEBIG: *Color-Based Image Processing to Measure Local Temperature Distributions by Wide-Band Liquid Crystal Thermography*. Applied Scientific Research, 56:113 – 143, 1996.

[13] BOWN, M. R., J. M. MACINNES and R. W. K. ALLEN: *Three-component micro-PIV using the continuity equation and a comparison of the performance with that of stereoscopic measurements*. Experiments in Fluids, 42:197 – 205, 2007.

[14] BOWN, M. R., J. M. MACINNES, R. W. K. ALLEN and W. B. J. ZIMMERMANN: *Three-dimensional, three-component velocity measurements using stereoscopic micro-PIV and PTV*. Meas. Sci. Technol., 17:2175 – 2185, 2006.

[15] BRÜBACH, J., A. PATT and A. DREIZLER: *Spray thermometry using thermographic phosphors*. Appl. Phys. B, 83:499–502, 2006.

[16] BRÜBACH, J., J. ZETTERBERG, A. OMRANE, Z. S. LI, M. ALDEN and A. DREIZLER: *Determination of surface normal temperature gradients using thermographic phosphors and filtered Rayleigh scattering*. Appl. Phys. B, 83:537–541, 2006.

[17] BRUCHHAUSEN, M., F. GUILLARD and F. LEMOINE: *Instantaneous measurement of two-dimensional temperature distributions by means of two-color planar laser induced fluorescence (PLIF)*. Experiments in Fluids,, 38:123 – 131, 2005.

[18] CAMCI, C., K. KIM and S. A. HIPPENSTEELE: *A New Hue Capturing Technique for the Quantitative Interpretation of Liquid Crystal Images Used in Convective Heat Transfer Studies*. Journal of Turbomachinery, 114:765–775, 1992.

[19] CASTANET, G., P. LAVIEILLE, M. LEBOUCHÉ and F. LEMOINE: *Measurement of the temperature distribution within monodisperse combusting droplets in linear streams using two-color laser-induced fluorescence*. Experiments in Fluids, 35:431 – 440, 2003.

[20] CERRO, R. L.: *Moving contact lines and Langmuir-Blodgett film deposition*. Journal of Colloid and Interface Science, 257:276 – 283, 2003.

[21] CHAN, T. L., S. ASHFORTH-FROST and K. JAMBUNATHAN: *Calibrating for viewing angle effect during heat transfer measurements on a curved surface*. International Journal of Heat and Mass Transfer, 44:2209 – 2223, 2001.

[22] CHEN, Q., E. RAMÉ and S. GAROFF: *The velocity field near moving contact lines*. Journal of Fluid Mechanics, 337:49 – 66, 1997.

[23] CIOFALO, M., M. SIGNORINO and M. SIMIANO: *Tomographic particle-image velocimetry and thermography in Raleigh-Benard convection using suspended thermochromic liquid crystals and digital image processing*. Experiments in Fluids, 34:156–172, 2003.

[24] COOLEN, M. C. J., R. N. KIEFT, C. C. M. RINDT and A. A. VAN STEENHOVEN: *Application of 2-D LIF temperature measurements in water using a Nd:YAG laser*. Experiments in Fluids, 27:420 – 426, 1999.

[25] COPPETA, J. and C. ROGERS: *Dual emission laser induced fluorescence for direct planer scalar behavior measurements*. Experiments in Fluids, 25:1 – 15, 1998.

[26] DABIRI, D. and M. GHARIB: *Digital particle image thermometry: The method and implementation*. Experiments in Fluids, 11:77 – 86, 1991.

[27] DKD: *Richtlinie DKD-R 5-3 Kalibrierung von Thermoelementen*. Deutscher Kalibrierdienst, 2001.

[28] DUSSAN, E. B.: *On the spreading of liquids on solid surfaces: static and dynamic contact lines*. Ann. Rev. Fluid Mech., 11:371 – 400, 1979.

[29] DUSSAN, E. B. and S. H. DAVIS: *On the motion of a fluid-fluid interface along a solid surface*. J. Fluid Mech., 65:71 – 95, 1974.

[30] FARINA, J., J. M. HACKER, R. J. MOFFAT and J. K. EATON: *Illuminant Invariant Calibration of Thermochromic Liquid Crystals*. Experimental Thermal and Fluid Science, 9:1 – 12, 1994.

[31] FERGASON, J. L.: *Liquid Crystals in Nondestructive Testing*. Applied Optics, 7:1729 – 1737, 1968.

[32] FILAR, P., E. FORNALIK, T. TAGAWA, H. OZOE and J. SZMYD: *Numerical and Experimental Analyses of Magnetic Convection of Paramegnetic Fluid in a Cylinder*. Journal of Heat Transfer, 128:183 – 191, 2006.

[33] FUENTES, J. and R. L. CERRO: *Flow patterns and interfacial velocities near a moving contact line*. Experiments in Fluids, 38:503 – 510, 2005.

[34] FUJISAWA, N. and S. FUNATANI: *Simultaneous measurement of temperature and velocity in a turbulent thermal convection by the extended range scanning liquid crystal visualization technique*. Experiments in Fluids, 29:158 – 165, 2000.

[35] FUJISAWA, N., S. FUNATANI and N. KATOH: *Scanning liquid-crystal thermometry and stereo velocimetry for simultaneous three-dimensional measurement of temperature and velocity field in a turbulent Rayleigh-Bérnard convection*. Experiments in Fluids, 38:291 – 303, 2005.

[36] FUJISAWA, N. and Y. HASHIZUME: *An uncertainty analysis of temperature and velocity measured by a liquid crystal visualization technique*. Measurement Science and Technologie, 12:1235 – 1242, 2001.

[37] FUJISAWA, N., T. NAKAJIMA, N. KATOH and Y. HASHIZUME: *An uncertainty analysis of temperature and velocity measured by stereo liquid-crystal thermometry and velocimetry*. Measurement Science and Technologie, 15:799 – 806, 2004.

[38] FUNATANI, S. and N. FUJISAWA: *Simultaneous measurement of temperature and three velocity components in planar cross section by liquid-crystal thermometry combined with stereoscopic particle image velocimetry*. Measurement Science and Technologie, 13:1197 – 1205, 2002.

[39] FUNATANI, S., N. FUJISAWA and H. IKEDA: *Simultaneous measurement of temperature and velocity using two-colour LIF combined with PIV with a colour CCD camera and its application to the turbulent buoyant plume.* Measurement Science and Technologie, 15:983 – 990, 2004.

[40] GLUCKMAN, B. J., H. WILLAIME and J. P. GOLLUB: *Geometry of isothermal and isoconcentration surfaces in thermal turbulence.* Phys. Fluids A, 5 No. 3:647–661, 1993.

[41] GÜNTHER, A.: *Large-Scale Structures in Rayleigh-Bénard Convection and Flow over Waves.* PhD thesis, ETH Zürich, Switzerland, 2001.

[42] GÜNTHER, A. and P. RUDOLF VON ROHR: *Influence of the optical configuration on temperature measurements with fluid-dispersed TLCs.* Experiments in Fluids, 32:533 – 541, 2002.

[43] GÜNTHER, A. and P. RUDOLPH VON ROHR: *Structure of the temperature field in a flow over heated waves.* Experiments in Fluids, 33:920 – 930, 2002.

[44] GREWAL, G. S., M. BHARARA, J. E. COBB, V. N. DUBEY and D. J. CLAREMONT: *A novel approach to thermochromic liquid crystal calibration using neural networks.* Measurement Science and Technology, 17:1918 – 1924, 2006.

[45] HALLCREST: *Handbook of Thermochromic liquid crystal technology.* Hallcrest, 1991.

[46] HAMRAOUI, A., K. THURESSON, T. NYLANDER and V. YAMINSKY: *Can a Dynamic Contact Angle be Understood in Terms of a Friction Coefficient?* Journal of colloid and Interface Science, 226:199 – 204, 2000.

[47] HAY, J. L. and D. K. HOLLINGSWORTH: *A Comparison of Trichromic Systems for Use in the Calibration of Polymer-Dispersed Thermochromic Liquid Crystals.* Experimental Thermal and Fluid Science, 12:1 – 12, 1996.

[48] HAY, J. L. and D. K. HOLLINGSWORTH: *Calibration of micro-encapsulated liquid crystals using hue angle and a dimensionless temperature.* Experimental Thermal and Fluid Science, 18:251 – 257, 1998.

[49] HEILAND, H. G., G. WOZNIAK and K. WOZNIAK: *Flow and temperature field measurements of thermal convection in a small vertical gap using liquid crystals*. Heat Mass Transfer, 43:863–870, 2007.

[50] HERMANN, S. and M. FUHRLAND: *Zum Langeinsatz von Schlauchwaagensystemen*. Allgemeine Vermessungsnachrichten, 4:142–145, 2006.

[51] HÖHMANN, C.: *Temperaturmessverfahren zur räumlich hochauflösenden Untersuchung des Wärmetransports an einem verdampfenden Flüssigkeitsmeniskus*. PhD thesis, Technische Universität Darmstadt, Technische Thermodynamik, 2004.

[52] HILLER, W. J., ST. KOCH, T. A. KOWALEWSKI and F. STELLA: *Onset of Natural Convection in a Cube*. International Journal of Heat and Mass Transfer, 13:3251 – 3263, 1993.

[53] HOFFMANN, M., M. SCHLÜTER and N. RÄBIGER: *Untersuchung der Mischvorgänge in Mikroreaktoren durch Anwendung von Micro-LIF und Micro-PIV*. Chemie Ingenieur Technik, 79 No. 7:1067–1075, 2007.

[54] HOHREITER, V., S. T. WERELEY, OLSEN M.G. and J.N. CHUNG: *Cross-correlation analysis for temperature measurement*. Measurement Science Technology, 13:1072–1078, 2002.

[55] HU, H. and M. M. KOOCHESFAHANI: *Molecular tagging velocimetry and thermometry and its application to the wake of a heated circular cylinder*. Measurement Science Technology, 17:1269–1281, 2006.

[56] ICHIYANAGI, M., Y. SATO and K. HISHIDA: *Optically sliced measurement of velocity and pH distribution in microchannel*. Exp. Fluids, 43:425–435, 2007.

[57] IRELAND, P. T. and T. V. JONES: *The response time of a surface thermometer employing encapsulated thermochromic liquid crystals*. J. Pys. E: Sci. Instrum., 20:1195 – 1199, 1987.

[58] JÄHNE, BERND: *Digital Image Processing*. Springer Verlag, 2005.

[59] KARASSO, P. S. and M. G. MUNGAL: *PLIF measurements in aqueous flows using the Nd:YAG laser*. Experiments in Fluids, 23:382 – 387, 1997.

[60] KEANE, R. D., R. J. ADRIAN and Y. ZHANG: *Super-resolution particle imaging velocimetry*. Meas. Sci. Technol., 6:754 – 768, 1995.

[61] KIM, H. J. and K. D. KIHM: *Application Of A Two-Color Laser Induced Fluorescence (LIF) Technique For Temperature Mapping*. ASME International Mechanical Engineering Congress and Exposition, New York, NY, November 11-16, 2001.

[62] KIM, H. J., K. D. KIHM and J. S. ALLEN: *Examination of radiometric laser induced fluorescence thermometry for microscale spatial measurement resolution*. International Journal of Heat and Mass Transfer, 46:3967 – 3974, 2003.

[63] KLANK, H., G. GORANOVIC, J. P. KUTTER, H. GJELSTRUP, J. MICHELSEN and C. H. WESTERGAARD: *PIV measurements in a microfluidic 3D-sheating structure with three-dimensional flow behaviour*. Journal of Micromechanics and Microengineering, 12:862 – 869, 2002.

[64] KOBAYASHI, T. and T. SAGA: *Time Response Characteristics of Microencapsulated Liquid-Crystal Particles*. Heat Transfer-Japanese Research, 27:390 – 398, 1998.

[65] KORNEV, K. G. and A.V. NEIMARK: *Spontaneous Penetration of Liquids into Capillaries and Porous Membranes Revisited*. Journal of Colloid and Interface Science, 235:101 – 113, 2001.

[66] KOWALEWSKI, T. A., A. CYBUILSKI and T. SOBIECKI: *Experimental model for casting problems*. Computional Methods and Experimental Measurements, pages 179 – 188, 2001.

[67] KOWALEWSKI, T. A., W. J. HILLER and G. DE VAHL DAVIS: *Computational and experimental visualization in heat and mass transfer problems*. Proc. of the First Japanese-Polish Joint Seminar in Advanced Computer Simulation, Tokyo, pages 60 – 69, 1993.

[68] KOWALEWSKI, T. A., J. PAKLEZA, J.-B. CHALFEN, M.-C. DULUC and A. CYBULSKI: *Visualization of vapor bubble growth*. 9th. International symposium on flow visualization, pages 176 – 179, 2000.

[69] KRUSE, N.: *Isothermal and Non-Isothermal Turbulent Flow over solid Waves: Transport and Structure.* PhD thesis, ETH Zürich, Switzerland, 2005.

[70] KUHN, S.: *Transport mechanisms in mixed convective flows over complex surfaces.* PhD thesis, ETH Zürich, 2008.

[71] KUMAR, A., S. J. WILLIAMS and S. T. WERELEY: *Experiments on opto-electrically generated microfluidic vortices.* Microfluidics and Nanofluidics, published online, 2008.

[72] LAGERWAARD, R.: *An experimental study of the interface temperature at free convective flow using liquid crystal thermography.* Master's thesis, Delft University of Technology, Department of Applied Physics, 2002.

[73] LARSEN, L.G. and J.P. CRIMALDI: *The effect of photobleaching on PLIV.* Experiments in Fluids, 41:803 – 812, 2006.

[74] LAVIEILLE, P., A. DELCONTE, D. BLONDEL, M. LEBOUCHÉ and F. LEMOINE: *Non-intrusive temperature measurements using three-color laser-induced fluorescence.* Experiments in Fluids, 36:706 – 716, 2004.

[75] LAVIEILLE, P., F. LEMOINE, G. LAVERGNE and M. LEBUOCHÉ: *Evaporating and combusting droplet temperature measurements using two-color laser-induced fluorescence.* Experiments in Fluids, 31:45 – 55, 2001.

[76] LEE, D. H., J. H. CHUNG, S. Y. WON, Y. T. KIM and S. BOO, K.: *A New Liquid Crystal Color Calibration Technique Using Neural Networks and Median Filtering.* KSME Int. J., 14:113 – 120, 2000.

[77] LEE, S. J. and S. KIM: *Micro Holographic PTV Measurements of Dean Flows in a Curved Micro-tube.* 14th International Symposium on Applications of Laser Techniques to Fluid Mechanics, Lisbon, Portugal, 07-10 July, 2008.

[78] LEGRAND, E. J. and W. A. RENSE: *Data on Rate of Capillary Rise.* Journal of Apllied Physics, 16:843 – 846, 1945.

[79] LEMOINE, F., Y. ANTOINE, M. WOLFF and M. LEBOUCHE: *Simultaneous temperature and 2D velocity measurements in a turbulent heated jet using combined laser-induced fluorescense and LDA.* Experiments in Fluids, 26:315 – 323, 1999.

[80] LEMOINE, F., M. WOLFF and M. LEBOUCHE: *Simultaneous concentration and velocity measurements using combined laser-induced fluorescence and laser Doppler velocimetry: Application to turbulent transport*. Experiments in Fluids, 20:319 – 327, 1996.

[81] LI, H., M. J. BRAUN and G. PAUDEL: *Flow structure and heat transfer in a lower half heated and upper half cooled rectangular enclosure*. International Journal of Heat and Mass Transfer, 49:3462–3476, 2006.

[82] LI, H., C. XING and M. J. BRAUN: *Natural convection in a bottom-heated top-cooled cubic cavity with a baffle at the median height: experiment and model validation*. Heat Mass Transfer, 43:895–905, 2007.

[83] LINDKEN, R., J. WESTERWEEL and B. WIENEKE: *Development of a Self-Calibrating Stereo-μ-PIV System and its Application to the Three-Dimensional Flow in a T-Shaped Mixer*. 6th International Symposium on Particle Image Velocimetry, Pasadena, California, USA, September 21 - 23, 2005.

[84] LINDKEN, R., J. WESTERWEEL and B. WIENEKE: *3D micro-scale velocimetry methods: A comparison between 3D-μPTV, stereoscopic μPIV and tomographic μPIV*. 13th International Symposium on Applications of Laser Techniques to Fluid Mechanics, Lisbon, Portugal, 26-29 June, 2006.

[85] LINDKEN, R., J. WESTERWEEL and B. WIENEKE: *Stereoscopic micro particle image velocimetry*. Experiments in Fluids, 41:161–171, 2006.

[86] LUTJEN, P. M., D. MISHRA and V. PRASAD: *Three-Dimensional Visualization and Measurement of Temperature Field Using Liquid Crystal Scanning Thermography*. Journal of Heat Transfer, 123:1006 – 1014, 2001.

[87] MA, X., G. E. KARNIADAKIS, H. PARK and M. GHARIB: *DPIV/T-driven convective heat transfer simulation*. International Journal of Heat and Mass Transfer, 45:3517 – 3527, 2002.

[88] MAQUA, C., G. CASTANET, F. LEMOINE, N. DOUÉ and G. LAVERGNE: *Temperature measurement of binary droplets using three-color laser-induced fluorescence*. Experiments in Fluids, 40:786 –797, 2006.

[89] MEINHART, C. D., S. T. WERELEY and M. H. B. GRAY: *Volume illumination for two-dimensinal particle image velocimetry*. Meas. Sci. Technol., 11:809 – 814, 2000.

[90] MEINHART, C. D., S. T. WERELEY and J.G. SANTIAGO: *PIV measurements of a microchannel flow*. Experiments in Fluids, 27:414 – 419, 1999.

[91] MEYER, K. N. and P. S. LARSEN: *Temperature and velocity fields in natural convection by PIV and LIF*. 11th Intl. Symposium on Applications of Laser Techniques to Fluid Mechanics, Lisboa, Portugal : Instituto Superior Técnico, pages 1–12, 2002.

[92] MOCHIZUKI, T., T. NOZAKI, Y.H. MORI and N. KAJI: *Heat transfer to liquid drops passing through an immiscible liquid medium between tilted parallel-plate electrodes*. International Journal of Heat and Mass Transfer, 42:3113–3129, 1999.

[93] NASAREK, R., S. WERELEY and P. STEPHAN: *Flow Field Measurements Near a Moving Meniscus of a Capillary Flow with Micro Particle Image Velocimetry (µPIV)*. Proceedings of the Sixth International ASME Conference on Nanochannels, Microchannels and Minichannels, ICNMM2008 June 23-25, 2008, Darmstadt, Germany, 2008.

[94] NATRAJAN, V. K. and K. T. CHRISTENSEN: *Development of Fluorescent Thermometry Methods for Microfluidic Systems*. 14th Int Symp on Applications of Laser Techniques to Fluid Mechanics Lisbon, Portugal, 07-10 July, pages 1–13, 2008.

[95] NICHOLSON, W. V. and R. M. GLAESER: *Review: Automatic Particle Detection in Electron Microscopy*. Journal of Structural Biology, 133:90 – 101, 2001.

[96] NISHIMURA, T., M. FUJIWARA and H. MIYASHITA: *Visualization of temperature fields and double-diffusive convection using liquid crystals in an aqueous solution crystallizing along a vertical wall*. Experiments in Fluids, 12:245 – 250, 1992.

[97] NOZAKI, T., T. MOCHIZUKI, N. KAJI and Y. H. MORI: *Application of liquid-crystal thermometry to drop temperature measurements*. Experiments in Fluids, 18:137 – 144, 1995.

[98] OLSEN, M. G. and R. J. ADRIAN: *Out-of-focus effects on particle image visibility and correlation in microscopic particle image velocimetry*. Experiments in Fluids [Suppl.], pages 166 – 174, 2000.

[99] OZAWA, M., U. MÜLLER, I. KIMURA and T. TAKAMORI: *Flow and temperature measurement of natural convection in a Hele-Shaw cell using a thermo-sensitive liquid-crystal tracer*. Experiments in Fluids, 12:213 – 222, 1992.

[100] PARK, H. G: *A Study of Heat Transport Processes in the Wake of a Stationary and Oscillating Circular Cylinder Using Digital Particle Image Velocimetry / Thermometry*. PhD thesis, California Institute of Technology, 1998.

[101] PARK, H. G., D. DABIRI and M. GHARIB: *Digital particle image velocimetry/thermometry and application to the wake of a heated circular cylinder*. Experiments in Fluids, 30:327 – 338, 2001.

[102] PARK, J. S., C. K. CHOI and KIHM K. D.: *Temperature measurement for a nanoparticle suspension by detecting the Brownian motion using optical serial sectioning microscopy (OSSM)*. Measuring Science and Technology, 16:1418–1429, 2005.

[103] PARK, J. S. and K. D. KIHM: *Three-dimensional micro-PTV using deconvolution microscopy*. Experiments in Fluids, 40:491 – 499, 2006.

[104] PEHL, M.: *In-situ Diagnose thermofluiddynamischer Vorgänge in komprimierten Flüssigkeiten*. PhD thesis, Lehrstuhl für Fluidmechanik und Prozessautomation der TU München, 2004, 2004.

[105] PEHL, M., F. WERNER and A. DELGADO: *First visualization of temperature fields in liquids at high pressure using thermochromic liquid crystals*. Experiments in Fluids, 29:302 – 304, 2000.

[106] PEREIA, F. and M. GHARIB: *Defocusing digital particle image velocimetry and the three-dimensional characterization of two-phase flows*. Measuring Science and Technology, 13:683 – 694, 2002.

[107] PEREIRA, F., M. GHARIB, D. DABIRI and D.: MODARRESS: *Defocusing digital particle image velocimetry: a 3-component 3-dimensional DPIV measurement technique. Application to bubbly flows*. Experiments in Fluids, 29:78 – 84, 2000.

[108] Pereira, F., J. Lu and E. Castano-Graff: *Microscale 3D flow mapping with* $\mu DDPIV. Experiments in Fluids, 42 : 589 - -599, 2007.$

[109] Pottebaum, T., S. and M. Gharib: *Using oscillations to enhance heat transfer for a circular cylinder.* International Journal of Heat and Mass Transfer, 49:3190 – 3210, 2006.

[110] Pottebaum, T. S. and M. Gharib: *The pinch-off process in a starting buoyant plume.* Experiments in Fluids, 37:87–94, 2004.

[111] Prasad, A. K. and J. R. Koseff: *Combined forced and natural convection heat transfer in a deep lid-driven cavity flow.* Int. J. Heat and Fluid Flow, 17:460 – 467, 1996.

[112] Quéré, D.: *Inertial capillarity.* Europhysics Letters, 39:533 – 538, 1997.

[113] Raffel, M., C. Willert and J. Kompenhans: *Particle Image Velocimetry - A Practical Guide.* Springer Verlag, 1998.

[114] Rao, Y., F. Dammel, P. Stephan and G. Lin: *Flow Frictional Characteristics of MEPCM Suspensions Flowing through Rectangular Minichannels.* 5th International Symposium on Multiphase Flow, Heat Mass Transfer and Energy Conversion, Xi'an, China, 3 - 6 July 2005, 2005.

[115] Rhee, H. S., J. R. Koseff and R. L. Street: *Flow visualization of a recirculating flow by rheoscopic liquid and liquid crystal techniques.* Experiments in Fluids, 2:57 – 64, 1984.

[116] Richards, C. D. and R. F. Richards: *Transient temperature measurement in a convectively cooled droplet.* Experiments in Fluids, 25:392 – 400, 1998.

[117] Roesgen, T. and R. Totaro: *A statistical calibration technique for thermochromic liquid crystals.* Experiments in Fluids, 33:732 – 734, 2002.

[118] Romano, V., A. D. Zweig, M. Frenz and H. P. Weber: *Time-Resolved Thermal Microscopy with Fluorescent Films.* Appl. Phys., B49:527 – 533, 1989.

[119] Ross, D., M. Gaitan and L. E. Locascio: *Temperature Measurement in Microfluidic Systems Using a Temperature-Dependent Fluorescent Dye.* Anal. Chem., 73:4117 – 4123, 2001.

[120] Sabatino, D. R., T. J. Praisner and C. R. Smith: *A high-accuracy calibration technique for thermochromic liquid crystal temperature measurements*. Experiments in Fluids, 28:497 – 505, 2000.

[121] Sakakibara, J. and R. J. Adrian: *Whole field measurement of temperature in water using two-color laser induced fluorescence*. Experiments in Fluids, 26:7 – 15, 1999.

[122] Sakakibara, J. and R. J. Adrian: *Measurement of temperature field of a Rayleigh-Bénard convection using two-color laser-induced fluorescence*. Experiments in Fluids, 37:331 – 340, 2004.

[123] Sakakibara, J., K. Hishida and M. Maeda: *Measurements of thermally stratified pipe flow using image-processing techniques*. Experiments in Fluids, 16:82 – 96, 1993.

[124] Sakakibara, J., K. Hishida and M. Maeda: *Vortex structure and heat transfer in the stagnation region of an impinging plane jet (simultaneous measurements of velocity and temperature fields by digital particle image velocimetry and laser-induced fluorescense)*. International Journal of Heat and Mass Transfer, 40, No. 13:3163 – 3176, 1997.

[125] Santiago, J. G., S. T. Wereley, C. D. Meinhart, D. J. Beebe and R. J. Adrian: *A particle image velocimetry system for microfluidics*. Experiments in Fluids, 25:316 – 319, 1998.

[126] Satake, S., T. Kunugi, K. Sato, T. Ito, H. Kanamori and J. Taniguchi: *Measurements of 3D flow in a micro-pipe via micro digital holographic particle tracking velocimetry*. Measurement Science Technology, 17:1647 – 1651, 2006.

[127] Savelski, M. J., S. A. Shetty, W. B. Kolb and R. L. Cerro: *Flow Patterns Associated with the Steady Movement of a Solid/Liquid/Fluid Contact Line*. Journal of Colloid and Interface Science, 176:117 – 127, 1995.

[128] Seuntiens, H. J., R. N. Kieft, C. C. M. Rindt and A. A. van Steenhoven: *2D temperature measurements in the wake of a heated cylinder using LIF*. Experiments in Fluids, 10:588 – 595, 2001.

[129] SHIKHMURZAEV, Y.: *Capillary flows with forming interfaces*. Chapman & Hall/CRC, Taylor and Francis Group, mLLC, 2008.

[130] SMITH, C. R., D. R. SABATINO and T. J. PRAISNER: *Temperature sensing with thermochromic liquid crystals*. Experiments in Fluids, 30:190 – 201, 2001.

[131] SPEIDEL, M., A. JONÁS and E. L. FLORIN: *Three-dimensional tracking of fluorescent nanoparticles with subnanometer precision by use of off-focus imaging*. Optics Letters, 28, No. 2, 2003.

[132] STEAERN, F. V., J. JOSEFSSON and S. TAGERUD: *Rhodamine B, a Fluorescent Probe for Acidic Organelles in Denervated Skeletal Muscle*. Journal of Histochemistry and Cytochemistry, 44-3:267–274, 1996.

[133] STOICA, V. and P. STEPHAN: *Measurement of temperature field around a single steady vapour bubble using phase shift interferometry*. Archives of Thermodynamics, 27:81–90, 2006.

[134] TIBERG, F., B. ZHMUD, K. HALLSTENSSONS and M. VON BAHR: *Capillary rise of surfactant solutions*. Physical Chemistry Chemical Physics, 2:5189 – 5196, 2000.

[135] TREUNER, M., H. J. RATH, U. DUDA and J. SIEKMANN: *Thermocapillary flow in drops under low gravity analysed by the use of liquid crystals*. Experiments in Fluids, 19:264 – 273, 1995.

[136] VEREIN DEUTSCHER INGENIEURE: *VDI Waermeatlas - Berechnungsblätter für den Wärmeübergang*. Springer Verlag, 2002, 9. Auflage.

[137] VOGT, J.: *Untersuchung des thermischen Antwortverhaltens von mikrogekapselten thermochromen Flüssigkristallen (TLCs)*. Bachelor's Thesis, Technische Universität Darmstadt, Technische Thermodynmaik, 2007.

[138] VOGT, J.: *Charakterisierung der Messmethode laserinduzierte Fluoreszenz (LIF) zur Bestimmung von Temperaturfeldern in Flüssigkeiten*. Master's Thesis, Technische Universität Darmstadt, Strömungslehre und Aerodynamik, 2008.

[139] WAGNER, E. and P. STEPHAN: *Frequency Response of a Surface Thermometer based on Unencapsulated Thermochromic Liquid Crystals*. Experimental Thermal and Fluid Science, 31:687 – 699, 2006.

[140] WALKER, D.: *A fluorescence technique for measurement of concentration in mixing liquids*. J. Phys. E: Sci Instrum., 20:217–224, 1987.

[141] WERELEY, S. T. and C. D. MEINHART: *Micron-Resolution Particle Image Velocimetry*. Springer Verlag, 2005.

[142] WIBERG, R. and N. LIOR: *Errors in thermochromic liquid crystal thermometry*. Review of Scientific Instruments, 75 No. 9:2985–2994, 2004.

[143] WILLERT, C. E. and M. GHARIB: *Three-dimensional particle imaging with a single camera*. Experiments in Fluids, 12:353 – 358, 1992.

[144] WISNIEWSKI, T. S., T. A. KOWALEWSKI and M. REBOW: *Infrared and Liquid Crystal Thermography in Natural Convection*. 8th International Symposium on Flow Visualization, 212, 1998.

[145] WOZNIAK, G., WOZNIAK K.: *Buoyancy and thermocapillary flow analysis by the combined use of liquid crystals and PIV*. Experiments in Fluids, 17:141 – 146, 1994.

[146] WU, M., J. W. ROBERTS and M. BUCKLEY: *Three-dimensional fluorescent particle tracking at micron-scale using a single camera*. Experiments in Fluids, 38:461–465, 2005.

[147] XUE, H.T., Z.N. FANG, J.P. HUANG and L.W. ZHOU: *Contact angle determined by spontaneous dynamic capillary rises with hydrostatic effects: Experiments and theorie*. Chemical Physics Letters, 432:326 – 330, 2006.

[148] YANG, C.-T. and H.-S. CHUANG: *Measurements of a microchamber flow by using a hybrid multiplexing holographic velocimetry*. Experiments in Fluids, 39:385 – 396, 2005.

[149] YOON, S. Y. and K. C. KIM: *3D particle position and 3D velocity field measurement in a microvolume via the defocusing concept*. Measurement Science Technology, 17:2897 – 2905, 2006.

[150] YOON, S. Y. and K. C. KIM: *Signal intensity enhancement of μ-LIF by using ultra-thin laser sheet illumination and aqueous mixture with ethanol/methanol for micro-channel applications*. Optics and Lasers in Engineering, 44:224 – 239, 2006.

[151] ZHMUD, B.V., F. TIBERG and K. HALLSTENSSON: *Dynamics of Capillary Rise*. Journal of Colloid and Interface Science, 228:263 – 269, 2000.

[152] ZHU, Y.: *Automatic Particle Detection Through Efficient Hough Transforms*. IEEE Transactions on Medical Imaging, 22, No. 9:1053 – 1062, 2003.

Curriculum Vitae

Persönliche Daten

Name:	Ralph Nasarek
Geburtsdatum:	24.11.1977
Geburtsort:	Heidelberg
Staatsangehörigkeit:	Deutsch

Schulbildung

1988 - 1993	Gymnasium Bildungszentrum Hemsbach
1993 - 1998	Starkenburggymnasium Heppenheim

Wehrdienst

1998 - 1999	Grundwehrdienst in Idar-Oberstein, Artillerie

Universitäre Ausbildung

10.1999 - 09.2001	Grundstudium des allgemeinen Maschinenbaus an der Technischen Universität Darmstadt
10.2001 - 07.2005	Hauptstudium an der Technischen Universität Darmstadt
07.2005	Abschluss der Diplomprüfung

Berufliche Tätigkeit

08.2005 - 01.2009	Stipendiat am Fachgebiet Technische Thermodynamik der Technischen Universität Darmstadt. Dissertation im Rahmen des Graduierten Kollegs 1114: "'Optische Messtechniken für die Charakterisierung von Transportprozessen an Grenzflächen"'
04.2008 - 05.2008	Forschungsaufenthalt an der Purdue University, Mechanical Engineering (Indiana, USA)
seit 02.2009	Anstellung bei Westinghouse Electrics Germany im Bereich Verfahrens- und Systemtechnik